Electromagnetic Field Exposure Reconstruction by Artificial Intelligence

Mohammed Tariqul Hassan Mallik

▶ To cite this version:

Mohammed Tariqul Hassan Mallik. Electromagnetic Field Exposure Reconstruction by Artificial Intelligence. Micro and nanotechnologies/Microelectronics. Université de Lille, 2023. English. NNT : 2023ULILN052 . tel-04835103

HAL Id: tel-04835103
https://theses.hal.science/tel-04835103v1

Submitted on 13 Dec 2024

Thèse de doctorat

présentée à

l'Université de Lille

Pour l'obtention du grade de
Docteur en Sciences
Spécialité: **Systèmes de Télécommunication**

par
Mohammed Tariqul Hassan MALLIK

Laboratoire d'accueil: Institut d'Électronique de Microélectronique et de Nanotechnologie IEMN– UMR CNRS 8520
École doctorale: 072 Sciences pour l'Ingénieur (SPI), Lille Nord-de-France

---

Electromagnetic Field Exposure Reconstruction by Artificial Intelligence

Reconstruction de l'exposition aux champs électromagnétiques à l'aide de l'intelligence artificielle

---

Soutenance prévue le 06/12/2023, devant le jury composé de:

Rapporteur	**François Septier**, Professeur, Universite Bretagne Sud, France.
Rapporteur	**Julien Sarrazin**, Maître de conférences HDR, Sorbonne Université, France.
President du Jury	**Alexandre Caminada**, Professeur, Université Côte d'Azur, France.
Examinateur	**Claude Oestges**, Professeur, Université catholique de Louvain, Belgique.
Examinatrice	**Emmanuelle Conil**, Ingénieure d'Études, ANFR, France.
Examinatrice	**Margot Deruick**, Assoc. Professeure, L'université de Gand, Belgique.
Directeur de thèse	**Davy Gaillot**, Maître de conférences HDR, Universite de Lille, France.
Co-Directeur de thèse	**Laurent Clavier**, Professeur, IMT Nord Europe, France.

In memory of my late mother.

Acknowledgments

I want to express my thanks and gratitude to my advisor, Davy Paul Gaillot and co-advisor Laurent Clavier, for their unwavering support and guidance throughout my academic journey, for Ph.D. research. Beyond their invaluable technical assistance, they played a pivotal role in shaping my research career. Recognizing my interest in research during multiple recruitment discussion, they have encouraged me to explore this Ph.D. opportunity. Without their encouragement and mentorship, I would not have had the chance to embark on these exciting research ventures. Davy and Laurent also granted me the freedom to pursue my passions and assisted me in developing my own research agenda over the years. They facilitated connections with several of my current collaborators, significantly expanding my research network. Most notably, Laurent is my mentor and has passionately answered zillions of my inquiries in this journey.

I want to express my thanks to co-supervisor Joe Wiart, who has been a guiding influence during my time at IRCICA. Joe has been a great source of support for my exploration in the field of telecommunication. Additionally, I'd like to acknowledge the warm reception and valuable assistance I've received from Joe and his team at Telecom Paris. They've played a pivotal role in broadening my understanding of propagation in the exposure field.

Next, my thanks are due to Benjamin Aellaert, for his invaluable collaboration in the field of machine learning using generative models for exposure reconstruction. Working alongside him and his associate has provided me with a comprehensive understanding of generative modeling, from generating data to building predictive models. I'd also like to extend my appreciation to Benjamin and his student for their warm hospitality during my visits to IMT Nord Europe, France.

Additionally, I'd like to express my gratitude to José María Molina García-Pardo and Esteban Eegea Lopez also known as Jose and Esteban, for their significant impact on my research in exposure simulations. Our stimulating conversations have played a pivotal role in shaping my studies on this topic. I'd also like to extend my appreciation to Esteban for broadening my research network through our joint efforts and also, for prompt answers in replying to all my queries at any time. Lastly, I want to thank Jose and Esteban for their warm welcome into their research group at UPCT, Spain. Engaging in discussions and collaborating with them and their students has been both enjoyable and fruitful.

I'm also grateful for the numerous undergraduate and graduate students I've had the privilege of working with at IMT Nord Europe. Their contributions have significantly influenced my development as a researcher. I'd like to thank Adam Idrissi, Majd Fassi, and Martin Hantson for engaging in insightful academic conversations that have sparked new research ideas.

I would also like to thank fellow Ph.D. and postdoctoral students Sofiane Kherbach, Angesom Tesfay, Shanshan Wang, Taghrid Mazloum, Nourel Islam, Cerine Mokhtari, Redha Kassi, Mamadou Ngom for their insightful discussion and collaboration.

Importantly, we couldn't have achieved any of this without the generous financial support from Métropole Européenne de Lille (MEL). I am especially thankful to MEL for enabling me to forge valuable connections with fellow experts in research. The MEL has proven to be immensely beneficial by offering a platform for implementing numerous techniques developed within this thesis. I would like to express my thanks to CNRS for their invaluable assistance and support in facilitating my appointment at IRCICA and making this project possible.

Finally, I'd like to express my thanks to my family and friends. First and foremost, I want to extend my appreciation to my father, Nazmul Ahsan Mallik, who has consistently provided me with guidance, assistance, and motivation throughout my life's journey. I also want to acknowledge my late mother, F.B.M., who had a remarkable foresight about my ability. Her belief in me will remain ever inspiring. I also want to recognize the contributions of my sister, Shameema Mallik, and her husband, Rubaiyat Imam, as well as my brother, Quamrul Mallik. Specifically, Quamrul Mallik has taught me how to develop the models and build repositories. Their encouragement and support have played a significant role in my research endeavors.

Résumé | Abstract

Résumé Le sujet de l’exposition aux champs électromagnétiques a fait l’objet d’une grande attention à la lumière du déploiement actuel du réseau cellulaire de cinquième génération (5G). Malgré cela, la reconstruction précise du champ électromagnétique à travers une région reste difficile en raison d’un manque de données suffisantes. Les mesures in situ présentent un grand intérêt, mais leur viabilité est limitée, ce qui rend difficile la compréhension complète de la dynamique du champ. Malgré le grand intérêt des mesures localisées, il existe encore des régions non testées qui les empêchent de fournir une carte d’exposition complète. La recherche a exploré des stratégies de reconstruction à partir d’observations provenant de certains sites localisés ou de capteurs répartis dans l’espace, en utilisant des techniques basées sur la géostatistique et les processus gaussiens. En particulier, des initiatives récentes se sont concentrées sur l’utilisation de l’apprentissage automatique et de l’intelligence artificielle à cette fin. Pour surmonter ces problèmes, ce travail propose de nouvelles méthodologies pour reconstruire les cartes d’exposition au Electromagnetic Field (EMF) dans une zone urbaine spécifique en France. L’objectif principal est de reconstruire les cartes d’exposition aux ondes électromagnétiques à partir de quelques données de capteurs répartis dans l’espace. Nous avons proposé deux méthodologies basées sur l’apprentissage automatique pour estimer l’exposition aux ondes électromagnétiques. Pour la première méthode, le problème de la reconstruction de l’exposition est défini comme une tâche de traduction d’image à image. Dans un premier temps, les données du capteur sont converties en une image et l’image de référence correspondante est générée à l’aide d’un simulateur basé sur le traçage de rayons. Nous avons proposé un réseau accusatoire génératif conditionnel (Conditional Generative Adversarial Network (cGAN)) conditionné par la topologie de l’environnement pour estimer les cartes d’exposition à l’aide de ces images. Le modèle est entraîné sur des images de cartes de capteurs tandis qu’un environnement est donné comme entrée conditionnelle au modèle cGAN. Cela nous permet d'estimer ou de reconstruire les cartes d'exposition EMF de manière dynamique lorsque les données des capteurs sont acquises toutes les deux heures. En outre, la cartographie du champ électromagnétique basée sur le Generative Adversarial Network est comparée au krigeage simple. Les résultats montrent que la méthode proposée produit des estimations précises et constitue une solution prometteuse pour la reconstruction des cartes d'exposition.

Cependant, la production de données de référence est une tâche complexe car elle implique de prendre en compte le nombre de stations de base actives de différentes technologies et de différents opérateurs, dont la configuration du réseau est inconnue, par exemple les puissances et les faisceaux utilisés par les stations de base. De plus, l'évaluation de ces cartes demande du temps et de l'expertise. Pour répondre à ces questions, nous avons défini le problème comme une tâche d'imputation de données manquantes. La méthode que nous proposons tient compte de l'entraînement d'un réseau neuronal infiniment large pour estimer l'exposition aux champs électromagnétiques. Nous avons dérivé un kernel de tangente neuronale pour un réseau neuronal infiniment large afin de compléter la matrice et d'estimer l'exposition aux champs électromagnétiques à partir d'un ensemble épars de valeurs mesurées par des capteurs dans un environnement urbain. La précision de cette approche découle d'une caractéristique préalable qui saisit la relation entre les coordonnées dans la matrice cible, ce qui s'apparente à un apprentissage semi-supervisé. Il s'agit d'une solution prometteuse pour la reconstruction des cartes d'exposition, qui ne nécessite pas de grands ensembles d'apprentissage. La méthode proposée est comparée à d'autres approches d'apprentissage automatique basées sur les réseaux UNet et les réseaux adversaires génératifs conditionnels, et les résultats montrent que l'approche proposée peut reconstruire les cartes d'exposition EMF sans utiliser un grand ensemble d'apprentissage.

Mots-clefs Exposition aux champs électromagnétiques, réseaux adversaires génératifs conditionnels, réseau neuronal à largeur infinie, neuronal tangent kernel.

Abstract The topic of electromagnetic field exposure has received a great deal of attention in light of the current rollout of the fifth-generation (5G) cellular network. Despite this, precise reconstruction of the electromagnetic field across a region is still difficult due to a lack of sufficient data. In-situ measurements have high interest, but their viability is constrained, making it difficult to fully understand field dynamics. Despite the high interest in localized measures, there are still untested regions that prevent them from providing a complete exposure map. Research has explored reconstruction strategies using observations from certain localized sites or spatially distributed sensors using techniques based on geostatistics and Gaussian processes. Notably, recent initiatives have focused on utilizing machine learning and artificial intelligence for this goal. To overcome these issues, This work proposes novel methodologies to reconstruct EMF exposure maps in a specific urban area in France. The main objective is to reconstruct EMF exposure maps from a few spatially distributed sensors. We have proposed two machine learning based methodologies to estimate EMF exposure. In the first method, the problem of exposure reconstruction is defined as image to image translation task. Initially, the sensor data is converted into an image and the corresponding ground truth image is generated using a ray tracing based simulator. We have proposed a conditional generative adversarial network (cGAN) conditioned on environment topology to estimate exposure maps using these images. The model is trained on sensor map images while an environment topology is given as conditional input as an image to the cGAN model. This allows us to estimate or reconstruct EMF exposure maps dynamically when sensor data is acquired every two hours. In addition, the conditional Generative Adversarial Network based electromagnetic field mapping is compared with simple kriging. Results show that the proposed method produces accurate estimates and is a promising solution for exposure map reconstruction.

However, generating ground truth data is a complex task since it involves taking into account the number of active base stations of different technologies and operators, whose network configuration is unknown, for example, powers and beams used by the base stations. Moreover, it takes time and expertise to evaluate these maps. Therefore, using ground truth data to infer exposure map need time and expertise to asses. In our second methodology, we have defined the exposure reconstruction problem as a missing data imputation task. Our proposed methodology takes into account training an infinitely wide neural network to estimate the EMF exposure. We derived a Neural tangent kernel for an infinitely wide neural network to perform matrix completion and estimate electromagnetic field (EMF) exposure from a sparse set of sensor-measured values in an urban environment. The accuracy of this approach stems from a feature prior that captures the relationship between coordinates within the target matrix, akin to semi-supervised learning. It is a promising solution for exposure map reconstruction, which does not require large training sets. The proposed method is compared with other machine learning approaches based on UNet and conditional generative adversarial networks and results show that the proposed approach can reconstruct EMF exposure maps without using a large training set.

Keywords EMF exposure, conditional generative adversarial networks, infinite width neural network, neural tangent kernel.

Contents

List of Figures

List of Tables

List of Abbreviations

MIMO Multiple-Input and Multiple-Output

RF-EMF Radio Frequency Electromagnetic Field

EM Electro Magnetic

EMF Electromagnetic Field

ICNIRP International Commission on Non-Ionizing Radiation Protection

IEEE-ICES IEEE-International Committee on Electromagnetic Society

MEL Métropole Européenne de Lille

ANN Artificial Neural Network

CNN Convolutional Neural Network

GAN Generative Adversarial Network

cGAN Conditional Generative Adversarial Network

NTK Neural Tangent Kernel

CNTK Convolutional Neural Tangent Kernel

General Introduction

Context

With the increasing use of wireless communication facilities, we live in a permanent Electromagnetic Field (EMF) that has induced concern and risk perception despite existing regulations. The people in charge of networks' deployment, the ones who check the compliance of EMF exposure to safety limits are facing such questions. The assessment of exposure requires specific equipment or simulation tools that can be complex to operate, therefore increasing the gap between laypeople and experts. The 5G deployment, which is just starting, reinforces these issues bringing new uncertainties resulting from the ever-increasing band used and the beam-forming introduced by massive Multiple-Input and Multiple-Output (MIMO).

Today, EMF monitoring is carried out using measurement campaigns. These in situ measurements are of great interest but they cannot be performed everywhere for capturing the dynamics of the field. Taking advantage of progress in connected devices technologies, the exposure assessment has been investigated using connected sensors. Recently, wireless sensors, autonomous in energy, have been designed and proposed. Associated in networks, these sensors are of great interest since they can grab the exposure's temporal variations; nevertheless, since they are still localized they cannot, alone, provide an exposure mapping because of unsampled locations. Reconstruction using measurements localized in some specific places has been investigated using methods based on geo-statistic and Gaussian processes. Recently, works have been carried out using artificial intelligence and machine learning. These works have been performed using simulations taking into account information that is available through databases (like the position of the base stations) as well as drive testing. Since these works dealt with simulations, confrontation with measures will require an adaptation of the method to increase the accuracy and take into account specific properties of the Electro Magnetic (EM) field.

Motivation

In wireless communication systems, in order to respond to the perception of risks related to EMF exposure and allocate radio resources, the estimation of the received power and exposure map is an essential task and a challenge. In recent years, exposure measurement methods have evolved significantly, providing researchers with new opportunities to quantify exposures with greater precision and accuracy. The Métropole Européenne de Lille (MEL), a public institution for inter-municipal cooperation in France showed much interest in EMF exposure maps for the city of Lille, France, to know if it is well under the regulatory limit, and funded this project. This thesis introduces novel methods for EMF exposure map reconstruction from sparse sensor measurement data and reviews and evaluates different exposure measurement methods used in environmental health research, with a focus on their strengths, limitations, and applications.

In this thesis, the following challenges are addressed:

1. **EMF exposure map reconstruction with generative models:** With the ongoing cellular network (5G) deployment, electromagnetic field exposure has become a critical concern. However, measurements are scarce, and accurate EMF reconstruction in a geographic region remains challenging. In an urban environment, EMF exposure map reconstruction from sparse sensor data is critical because of the limitations of measurement points. Moreover, environment topology plays a big role in propagation characteristics. Therefore, these issues need to be addressed for the accurate reconstruction of EMF exposure maps in an urban area using a generative model.

2. **EMF exposure map reconstruction by matrix completion:** As we mentioned, the lack of measurements makes it difficult to estimate an electromagnetic field accurately in a specific urban area. Moreover, using a ground truth full exposure map of a specific area is difficult to find in reality. When large quantities of data are missing, exposure map reconstruction techniques construct these maps from a collection of measurements from spatially distributed sensors. Therefore, there is a need for exposure map reconstruction techniques without using a ground truth or full exposure map which is proposed in this technique.

Chapter 1

Introduction

The research conducted for this thesis is introduced in this chapter. Section 1.1 states the context. Existing methods for exposure map estimation are described in Section 1.2. The contributions to exposure map reconstruction are discussed in Section 1.3, Lastly, Section 1.4 provides the dissertation's framework.

1.1 Context

EMF exposure from wireless communication, including 5G technology, is a topic of ongoing research and debate among scientists and policymakers. While some studies suggest that high levels of EMF exposure can be harmful to human health, others suggest that the levels emitted by 5G technology are well within safety limits. However, concerns remain about the potential long-term effects of prolonged exposure to EMF radiation in general and 5G in particular, especially for vulnerable populations such as children and pregnant women. To address these concerns, regulatory agencies have established safety guidelines, and manufacturers are required to ensure their products comply with these standards before they can be sold to the public. EMF exposure protection limits have been proposed by the International Commission on Non-Ionizing Radiation Protection (ICNIRP) [132] and the IEEE-International Committee on Electromagnetic Society (IEEE-ICES) [78]. These limits, composed of fundamental limitations and reference values, are established to prevent any adverse health effects due to EMF exposure. Due to their practicality, conservative reference levels are frequently utilized. To avoid any overexposure, the directive 2013/35/EU [139], which is based in part on ICNIRP [5] and IEEE-ICES [119, 77], calls for monitoring the employees exposure to EMF. Under the European Directive 2013/35/EU, reference levels are utilized as action values.

1.1.1 Radio Frequency Electromagnetic Fields

The electromagnetic spectrum is divided into two categories: ionizing and non-ionizing radiation, which are distinguished by their physical and natural impacts. EMFs produced by the interaction of electric and magnetic fields [169] as illustrated in Figure 1.1.

Ionizing radiation refers to high-energy radiation that has enough energy to remove tightly bound electrons from atoms, thereby creating ions. This process of ionization can lead to significant chemical and biological effects, making ionizing radiation potentially harmful to living organisms and materials. The main types of ionizing radiation are Alpha Particles, Beta particles, Gamma particles, X-rays, etc.

Non-ionizing radiation refers to a type of electromagnetic radiation that has lower energy levels than ionizing radiation and lacks the capability to remove tightly bound electrons from atoms, thereby not causing ionization. Non-ionizing radiation is generally considered to be less harmful than ionizing radiation and some common sources are: Radiofrequency (RF) Radiation, Microwave Radiation, Ultraviolet (UV) Radiation (Lower Energy), etc. Ionizing radiation is generated by the release of electrons from atomic structures, causing harm to the Deoxyribonucleic Acid (DNA), while non-ionizing radiation causes molecules to vibrate [99]. In this thesis, we will focus on non-ionizing radiation.

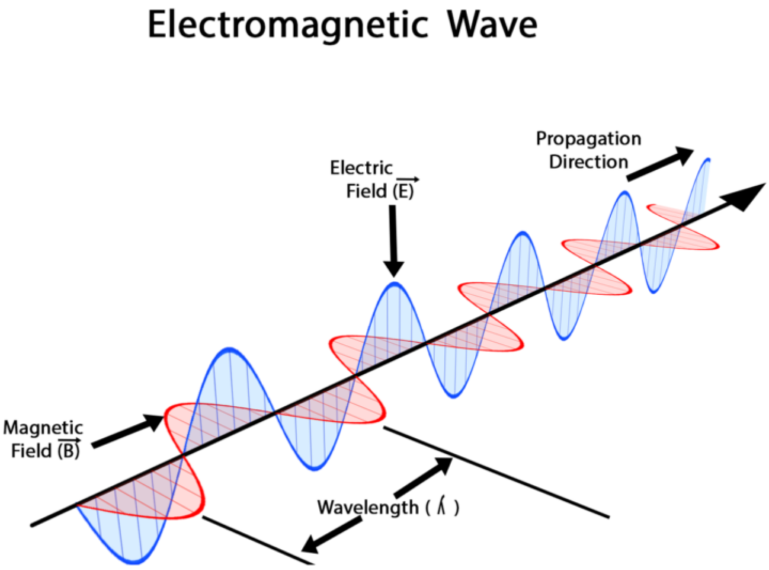

Figure 1.1: Wave propagation in the presence of magnetic and electric field vibrations

Either the electric field strength (E), which is expressed in Volt per meter (V/m), or the power flux density (S), which can be expressed in Watt per square meter - (W/m^2), can be used to determine the intensity of EMFs. Eq. (1.1)'s formula can be used to transform these two units into one another. A physical constant that describes a characteristic of wave propagation through the air, the free space impedance, or Z_0, has a value of 377 Ω [99]. Eq. (1.1) shows a quadratic connection between the two measurement scales, E and S.

$$E = \sqrt{S \times Z_0} \text{ and } S = E^2/Z_0. \tag{1.1}$$

In general, there are two types of EMFs: natural sources, like the earth's static field, and man-made sources, including the release of Radio Frequency Electromagnetic Field (RF-EMF)s from base stations for mobile phones and broadcast transmitters. The specific absorption rate (SAR), which is defined as the power in $Watt$

that is absorbed per 1 kg tissue, is a measure of RF energy dosage [126]. EMFs are especially employed in the area of information technology.

EMFs are a type of non-ionizing radiation that exists in the electromagnetic spectrum (refer to Figure 1.2) and are categorized into low-frequency (LF; up to 10 MHz) and radio-frequency (RF; 10 MHz-300 GHz) EMFs.

The frequency (measured in Hz) is one of the critical factors used to differentiate EMFs, where one oscillation per second is equivalent to 1 Hz, and the corresponding wavelength is shown in Figure 1.2.

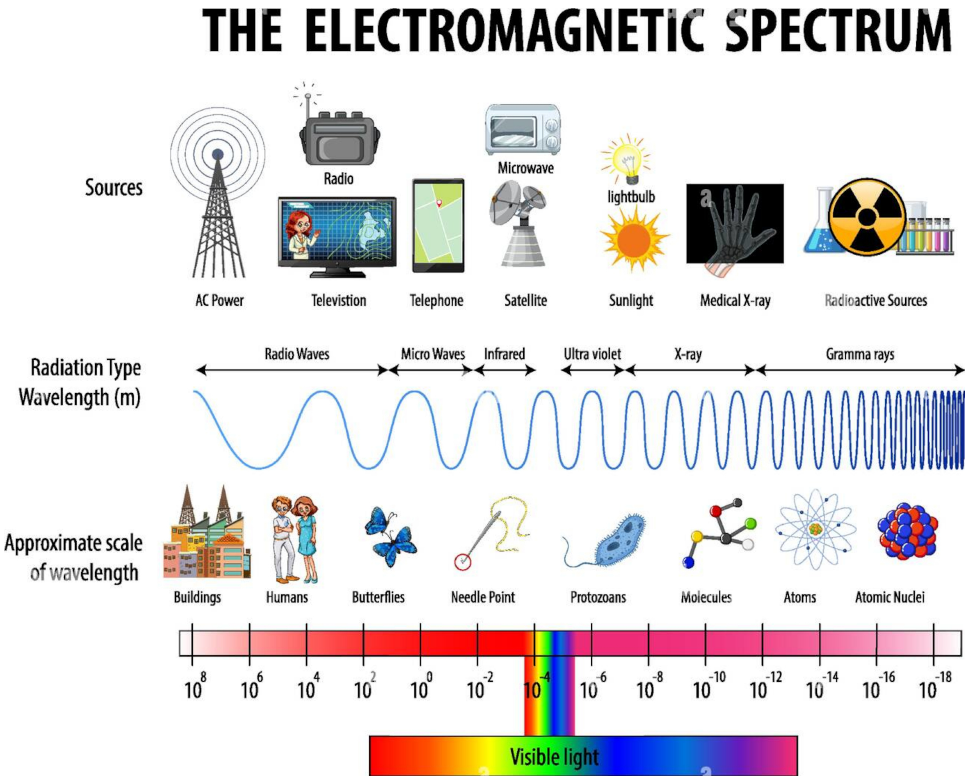

Figure 1.2: The electromagnetic spectrum for xHz to yGHz

1.1.2 Characteristics of Radio Frequency Electromagnetic Field

We are interested in telecommunications technology, where RF-EMFs are used to transmit wireless data across long distances between a transmitter (such as mobile phone base stations or broadcast transmitters) and a receiver. (e.g. mobile phone handsets, televisions, and radios). The communication between a mobile phone base station and a mobile phone handset is referred to as downlink exposure, and the communication between the two is referred to as uplink exposure, depending on the direction of the signal. The most important frequencies, including all uplink and downlink telecommunication frequencies between 100 MHz and 5.5 GHz used are listed in Table 1.1.

Table 1.1: Most relevant RF-EMF frequency signals and their characteristics

Location	**RF-EMF Source**	**Communication Standard**		**Frequency (MHz)**
Out	Base Station for radio	FM	Frequency Modulation	100
Out	Base Station for radio	DAB	Digital Audio Broadcasting	220
Out	Base Station for television	TETRA	Terrestrial Trunked Radio	390
Out	Base Station for television	Analogue TV	Analogue TV	174–223
Out	Base Station for television	DVB-T/TV	Digital Video Broadcasting–Terrestrial	470–830
Out	Base Station for television	UHF	Ultra-high frequency Television	470–860
Out	BS for mobile telecommunications	GSM900 DL	Global System for Mobile Communications	900
Out	BS for mobile telecommunications	GSM1800 DL	Global System for Mobile Communications	1800
Out	BS for mobile telecommunications	DCS1800 DL	Digital Communication System	1800
Out	Base station/Small cell	UMTS DL	Universal Mobile Telecommunications System	2100
Out	Base station/Small cell	LTE	Long Term Evolution	2600
In	Femtocell	UMTS DL	Universal Mobile Telecommunications System	2100
In	Femtocell	LTE DL	Long Term Evolution	2600
In	Femtocell	5G	5th generation mobile network	700, 2100, 3500
In	Access point	WIFI 2G	Wireless Local Area Networks	2400
In	Access point	WIFI 4G	Wireless Local Area Networks	2400
In	Access point	WIFI 5G	Wireless Local Area Networks	5500
In	Mobile phone/Tablet	GSM900 UL	Global System for Mobile Communications	900
In	Mobile phone/Tablet	GSM1800 UL	Global System for Mobile Communications	1800
In	Mobile phone/Tablet	DCS1800 UL	Digital Communication System	1800
In	Mobile phone/Tablet	UMTS UL	Universal Mobile Telecommunications System	2100
In	Mobile phone/Tablet	LTE UL	Long Term Evolution	2600
In	Cordless phone	DECT	Digital enhanced cordless telecommunications	1880

Exposure sources to RF-EMFs in daily life may essentially be divided into near-field and far-field sources (see Figure 1.3). Mobile phone handsets and cordless phones are examples of near-field sources that operate close to the body and can result in exposure levels that are up to 100 times greater than those from far-field sources 1.3. When compared to far-field sources, the maximum energy local absorption in the skull is around 1000–100 000 times higher during calls [95]. The power flux density drops ideally inversely according to the square of the distance from a source, or $1/r^2$. According to [87], far-field sources are "radiation from a source located at a distance of more than one wavelength." It is to be noted that the near field approximation holds depending on the wavelength and the size of the antenna. With massive antennas and reflecting intelligent surfaces (RIS), the near field situation could be more often encountered. But it does not impact the work in this Ph.D. Base stations for mobile phones and broadcast transmitters are examples of sources. However, in this situation, neighboring individual cell phones also count as far-field sources. Although the total body is continually exposed and the exposure time can be much longer, far-field sources provide noticeably lower exposure levels than near-field sources [57, 153].

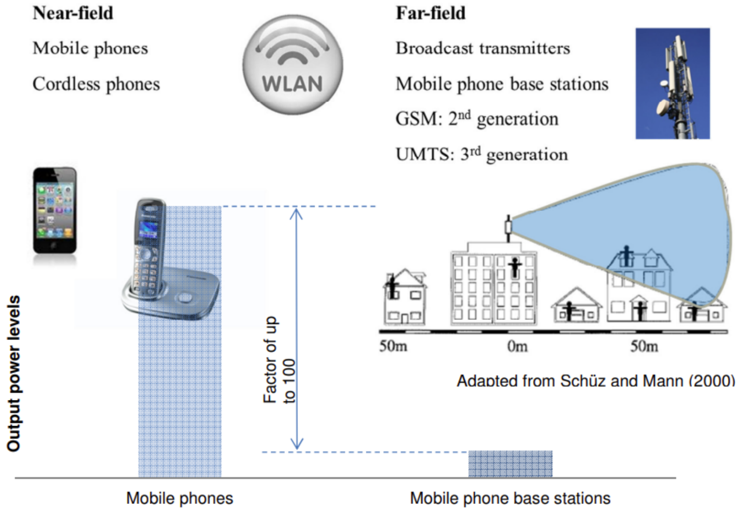

Figure 1.3: : Near-field and far-field sources, illustrating differences of output power levels.

1.1.3 Potential adverse impacts on health

Controversy surrounds discussions on the health impacts of RF-EMFs. In 2011, the International Agency for Research on Cancer (IARC) classified RF-EMF as potentially carcinogenic, falling under category 2B [15].

Mobile phones expose the head to RF-EMFs the most, thus implying that harmful health effects would likely result in tumors in the head region. Specifically, there is concern about various types of brain tumors (glioma and meningioma), acoustic nerve tumors (schwannoma, also known as acoustic neuroma), and parotid gland tumors [15]. In order to investigate whether mobile phone use could have negative health effects, numerous studies have been conducted. One of the most extensive studies, the INTERPHONE study, was coordinated by the WHO (World Health Organization). This study, which followed a standard protocol, included 2708 glioma and 2409 meningioma cases and matched controls across 13 countries [63]. They concluded that, in general, the usage of mobile phones did not show any rise in the likelihood of glioma or meningioma. Although there were indications of a heightened glioma risk at the most intense exposure levels, the presence of biases and errors hinders a definitive causal explanation. Additional research is needed to explore the potential impacts of prolonged and frequent mobile phone usage.

It has been suggested that children are a more susceptible population than adults and face a greater threat as they begin to utilize their cellular devices at an earlier age, which ultimately results in a greater cumulative exposure over their lifespan [24]. Brain tumors are the second most prevalent type of tumors in children, following leukemia [1]. In order to explore whether mobile phone usage is linked to the risk of brain tumors in children and adolescents, the CEFALO multicenter case-control study compiled data from Denmark, Sweden, Norway, and Switzerland, incorporating all individuals aged 7 to 19 years old. The study found no heightened risk of brain tumors in the areas of the brain that absorb the greatest amount of energy. Mobile phone users are not more inclined to be diagnosed with brain tumors compared to non-users ($Odds \quad ratio \quad OR = 1.36, 95\% \quad CI = 0.92 \quad to \quad 2.02$). Children who began using their mobile phones five years before the investigation did not exhibit an elevated risk in comparison to non-regular users ($Odds \quad ratio \quad OR = 1.26, 95\% \quad CI = 0.70 \quad to \quad 2.28$). The researchers concluded that there is no proof of causal connection with regard to the lack of a correlation between exposure to mobile phone usage and the localization of the brain tumor [14].

[147] proposes a thorough analysis of the scientific literature was carried out to investigate the correlation between mobile phone usage and the potential risk of developing brain tumors. The collation of epidemiological studies through a meta-analysis yielded no significant proof for an elevated risk of adult brain cancer or other head tumors associated with the use of mobile phones. Likewise, in vivo studies that evaluated the oncogenicity, tumor promotion, and genotoxicity of the brain cells, or the incidence of tumors in the head or other body parts showed the same result [147].

Most of the research examining the link between cell phone usage and brain tumors fails to find a causal relationship [6, 14, 57, 63, 147]. Considering the significant increase in mobile phone usage in recent times, it stands to reason that any potential risks of brain tumors would have manifested as an uptick in new cases. However, no such trend has been observed in different countries [43, 81]. Methodological restrictions, like selection bias and analysis of retrospective questionnaire data, make the interpretation of data more challenging and could explain some of the potential increases in risk found in some studies.

In addition to brain tumors, commonly reported health effects associated with EMFs are self-reported nonspecific symptoms, known as electromagnetic hypersensitivity or idiopathic environmental intolerance [156]. These symptoms can include headaches, sleep disturbances, and difficulty concentrating [152]. Experimental studies conducted under double-blind and randomized conditions have provided strong evidence that low levels of EMFs cannot be perceived [154, 152].

In [163], A case-control study was conducted, including 894 individuals without health issues and 211 individuals diagnosed with breast cancer. All participants were requested to complete standard questionnaires aimed at gathering data about sleep quality, smartphone addiction, and smartphone usage. The research concluded that excessive smartphone use significantly increased the risk of breast cancer, particularly for participants with smartphone addiction, a close distance between the breasts and smartphone, and the habit of smartphone use before bedtime. There is not much evidence of acute impacts from research on the RF-EMFs emitted by 2G mobile phones on subjective symptoms, well-being, and physiological measures [13]. Numerous researches have not been able to highlight a connection between RF-EMFs and general symptoms, and there is no proof that people may sense or be sensitive to EMFs [76, 156], according to these investigations.

However, there are signs of the opposite of placebo effects, known as nocebo effects, which are unfavorable outcomes brought on by unfavorable expectations. Numerous research studies have investigated the nocebo effects of EMFs [13, 156]. Notably, when patients were aware of their exposure to EMFs, their symptoms intensified and increased.

Various investigations have explored the adverse effects on personal sleep quality [72, 146, 125]. Results from these studies suggest that there is generally no correlation between exposure to RF-EMF and concrete sleep measurements [125]. However, [125] identified minor dissimilarities in the EEG (electroencephalography) pertaining to specific frequency bands.

As per present investigations, it appears that there is no correlation between the usage of mobile phones and a surge in health adversities in the brief period of less than a decade. However, for individuals who use these devices extensively or over an extended duration of over 10-15 years, there are certain uncertainties. The COSMOS research -link, regarded as one of the world's most extensive cohort studies, strives to monitor health over the long run in a vast group of study participants [161].

Experimental research examines only immediate consequences, while extended-term hazards necessitate examination through epidemiological investigations.

1.1.4 RF-EMF exposure regulations

The ICNIRP, an independent body of scientific experts funded by public funds, proposed and published recommendations for restricting RF-EMF exposure in all residential areas [5]. The reference levels proposed by the ICNIRP are dependent on frequency and are 41 V/m for 900 MHz, 58 V/m for 1800 MHz, and 61 V/m for 2100 MHz 1.2. These stated reference levels are based on research studies exploring the negative health effects of RF-EMFs. Experimental investigations indicate that generating a whole-body SAR between 1 and 4 W/kg, trigger an increase in temperature that is under 1°C. Exposure to SAR values above 4 W/kg from stronger fields may lead to irreparable consequences, impairing thermoregulation mechanisms and resulting in tissue damage (ICNIRP, 1998). The EMF initiative of the WHO compiled an international database with guidelines [135]. The ICNIRP, an independent body of scientific experts funded by public funds, proposed and published recommendations for restricting RF-EMF exposure in all residential areas [5]. The reference levels proposed by the ICNIRP are dependent on frequency and are 41 V/m for 900 MHz, 58 V/m for 1800 MHz, and 61 V/m for 2100 MHz 1.2. These stated reference levels are based on research studies exploring the negative health effects of RF-EMFs. Significant variations exist among nations in terms of the regulatory thresholds they incorporate into their legislation. When discussing the safety of unexplored dangers, a vital inquiry arises: what level of safety is sufficient [53] while certain countries, such as the Netherlands, have embraced ICNIRP reference values, others like Switzerland and Belgium have implemented frequency-dependent safety guidelines as precautionary measure (Table 1.2).

Frequency	ICNIRP reference levels	The Netherlands	Precautionary limits for places with sensitive use and places of residence		
			Switzerland	Brussels	**France**
GSM 900	42 V/m	42 V/m	4 V/m	3 V/m	6 V/m
GSM 1800	42 V/m	42 V/m	6 V/m	4.2 V/m	6 V/m
5G	63 V/m	63V/m	6 V/m	4.5 V/m	6 V/m

Table 1.2: Overview of the different limits adopted in Switzerland, Belgium and the Netherlands, France (Source: Federal Office for the Environment (FOEN), Resolution of the Flemish Government and Resolution of the Brussels Capital Region)

The World Health Organization [185] provided a key rationale for the implementation of safety precautions.

"To address public health concerns that potential or perceived but unproven health problem is taken into account..." (WHO 2003, p. 3)

The aim of the "Ordinance relating Protection from Non-Ionising Radiation" (ONIR), ordinance in Switzerland is to safeguard individuals against potential detrimental impacts or disturbances resulting from non-ionizing radiation [38]. This regulation applies to the radiation released by a solitary base station and is solely applicable to vulnerable areas where people spend most of their time, such as their dwellings, schools, preschools, hospitals, nursing homes, workplaces, and playgrounds. In Belgium, more stringent regulations are enforced than those in Switzerland. In Ghent, the exposure limits of the Flemish region (Resolution of the Flemish Region of Nov. 2010) regulate a frequency-dependent cumulative exposure of 21 V/m for a 900 MHz frequency. Indoor premises and children's playgrounds adhere to limits of 3 V/m at 900 MHz, 4.2 V/m at 1800 MHz, and 4.5 V/m at 2100 MHz per base station. These preventative limits are determined using Eq. (1.2) for the frequency range from 400 MHz to 2 GHz.

$$E = 0.1 * \sqrt{f}, \text{where f is frequency in MHz} \tag{1.2}$$

A maximum threshold of 4.5 V/m is enforced for the spectrum spanning from 2 GHz to 10 GHz. The Brussels Capital Region enforces the strictest limitations, as prescribed in the Brussels Capital Region Ordinance, effective at all communal sites to ensure combined exposure. Eq. (1.3) is employed to compute the restrictions for frequencies from 400 MHz to 2 GHz.

$$S = \frac{f}{4000} \quad \text{and} \quad E = \sqrt{\frac{f}{4000} * 377}. \tag{1.3}$$

Exposure values for frequencies between 2 GHz and 300 GHz might not fall higher than 4.33 V/m, which is equivalent to 0.05 W/m^2 of power flux density. To make room for the deployment of 5G (Long-term Evolution, LTE) in Brussels, the restrictions in the Brussels Capital Region will be changed.

1.1.5 Métropole Européenne de Lille (MEL) concern on public health implication on Exposure

MEL is a public entity for inter-municipal cooperation that was created by a law on December 31$^{\text{st}}$, 1966, in France. In a region that is both rural and urban, made up of large cities and villages, it houses over a million people. The MEL takes action in a number of crucial areas, including town and country planning, culture, household waste, sustainable development, water and purification, economy and employment, public space and public road network, Europe and international attractiveness, housing environment and housing, urban affairs, nature and living environment, sport, tourism, transport and mobility, accessibility for the disabled, and crematoriums. There is a growing concern about the potential health risks associated with exposure to electromagnetic radiation from 5G technology. Some studies suggest that long-term exposure to high levels of EMF radiation may increase the risk of cancer, neurological disorders, and other health problems. **Métropole Européenne de Lille (MEL)** has expressed interest in studying the potential impact of EMF exposure on its inhabitants. This interest reflects a growing concern among policymakers and the public about the potential health risks associated with prolonged exposure to EMF radiation. The study could provide valuable insights into the nature and extent of EMF exposure in Lille, and inform policies aimed at reducing potential risks to public health. Through multiple discussions and negotiations amongst **Prof. Dr. Laurent Clavier, Prof. Dr. Davy Gaillot and Prof. Dr. Joe Wiart** and MEL counterpart, MEL wanted to facilitate this idea and funded this Ph.D. project for the first time to develop a solution for spatial EMF exposure maps in the city of Lille. The map is constructed from a few fixed sensor-measured values over time. The request from MEL is the following:

- Develop a solution for exposure maps based on AI
- Need time-varying maps of EMF
- Spatial sampling of the field is fixed with few sensors
- Reconstructing the full map from the knowledge of these few sensors

The proposed solution for spatial EMF exposure reconstruction in Lille will involve the use of classical and modern machine learning algorithms to predict the EMF levels at different locations based on the limited sensor data available. The main scope of the task is developing and implementing these algorithms, as well as analyzing the accuracy and reliability of the results.

1.2 State of the Art

In the field of radio map estimation, a significant amount of work has been done, mostly concentrating on mapping three channel metrics: power, (Power Spectral Density) PSD, and channel-gain. Few works have been done in exposure map reconstruction in the literature, but open issues remain, the following section includes a summary of each of the current methods for radio map estimation and exposure map techniques and reviews to address their problem.

1.2.1 Coverage Map Reconstruction

Various techniques have been utilized to construct power maps from spatially distributed sensor measurements, including interpolation and regression approaches [8, 23, 4, 150]. Among these methods, kriging or Gaussian process regression has been employed in [193, 199, 27]. It involves estimating the power values at unobserved locations using a weighted linear combination of the available power measurements. The kriging weights are determined by the minimum mean square error estimator [90] that relies on a presumed statistical correlation among the measurements, usually expressed via a spatial covariance function. A matrix completion task is presented in [45], where the unobserved power values are determined via nuclear norm minimization. The compressive sensing technique is employed in [86], exploiting the sparse spatial distribution of primary users to construct power maps. On the other hand, a dictionary learning approach is proposed in [85, 92] to decompose power measurements into linear combinations of channel gains and transmit power for power map construction. Additionally, non-parametric power maps have been developed in [65, 197] using radial basis functions (RBFs), where the received power at each location is estimated through a weighted linear combination of RBF parameters and weights, which are optimized jointly. To estimate power maps, [75] models path loss with a Laplacian function and presents a sparse Bayesian learning method. Finally, a kernel-based learning algorithm is devised in [20, 197] that employs multiple kernels to capture path loss and shadowing for power map estimation. The method based on radial basis functions (RBF) is widely used and has been studied by various researchers [33, 145]. Compared to other methods, RBF is more flexible, as it makes fewer assumptions about the input data by only considering the distance-based dependency, and has been found to be more tolerant of uncertainty [158]. In [33], the authors divided a database of outdoor (Received Signal Strength Indicator) RSSI measurements into training and testing subsets and evaluated different kernel functions for interpolation. In [67] for instance, to enhance the efficiency of fundamental kriging, it is recommended to explore unvisited locations/grid-cells, where the estimated value is still assumed to be imprecise. A somewhat analogous crowdsourcing approach has also been utilized in [52] by framing the issue as a matrix completion problem utilizing singular value thresholding. This technique allows one to solicit further measurements at certain specific points where the algorithm lacks confidence in the estimated outcome. An alternative method explored for indoor wireless localization depends on both collected field data and an a priori path loss model that takes into account the impact of walls' weakening effect between the sender and receiver [94]. In outdoor settings, instead of using raw Received Signal Strength Indication (RSSI) data, local path loss models (and thus, specialized RSSI distributions) have been utilized to capture small-scale impacts in clusters of measured neighboring points [131], where a fitting RSSI distribution model is established for each group. However, these parametric path loss models are usually imprecise and require impractical on-site calibration, resulting in very limited generalization abilities. A very comparable strategy, except for the utilization of extra contextual information, is presented in [104], where they propose a technique called SateLoc. Based on satellite imagery, they suggest segmenting the areas "crossed" by a specific radio link, based on their category (e.g., terrain, water, forest, etc.). Then, the power path loss contributions are computed proportionally to the size of the crossed region(s), according to a priori model parameters (i.e., related to each environment type), and added together to determine the end-to-end path loss value.

1.2.1.1 Deterministic and Empirical models

In a given urban region, it is computationally costly to evaluate radio frequency power maps and exposure maps with accuracy. Propagation tools like Veneris-Opal [49], and Atoll [54] are based on Ray Tracing (RT) methods, where the propagating field is simulated with an array of rays that go through the environment and reflect, diffract, and scatter. These techniques depend on the Maxwell equations' high-frequency approximation (optical ray). These simulators only provide stochastic or simplified hybrid techniques since this methodology is computationally too costly to be applied in large and, in particular, dynamic environments and not adapted to network activity.

The maximum level of precision is provided by RT approaches, however, they frequently have significant processing requirements and depend on the correctness of the tridimensional (3D) model of the environment [195]. Ray-tracing and empirical / semi-empirical models like close-in (CI), floating intercept (FI), alpha, beta, gamma (ABG) [109, 140, 10], etc. are often used to predict power coverage in metropolitan areas. In previous studies, deterministic and empirical models were utilized to predict propagation. Examples include ray-tracing [149], the dominant path model [177, 17], and empirical models [202].

1.2.2 Exposure Map Reconstruction

1.2.2.1 Stochastic Geometry

The concept of using stochastic geometric in wireless communications is not new [32]. Numerous industries have used it, including localization, automobile radar [35], cumulated interference power [116]. Stochastic geometry is a useful tool, providing us with the mean exposure or CDF of exposure. However, it is important to note that this information is not directly linked to the spatial location of the user or the specific spot where we seek to understand the exposure. The authors of [59, 60, 61] have employed a stochastic geometric approach to model the exposure to EMF using drive test data obtained from the city Brussels, in Belgium. These methods relied on the assumption that the measurements obtained from the drive test constituted a single measurement, without considering the temporal variations. Consequently, the outcome is a single map representing the mean exposure rather than a dynamic map.

1.2.2.2 Kriging

The kriging method is the traditional approach for interpolating geographical data. Kriging has been used in several studies to reconstruct exposure maps, including [2, 3, 115, 162]. Additionally, in [164], field maps were interpolated utilizing data on a path from a moving robot in an indoor scenario using a Gaussian process or kriging approach. However, time evaluation was not taken into account in any of these studies resulting in one single map of the target area. Furthermore, the current body of scientific literature lacks substantial evidence or comprehensive research regarding the ability to accurately model electromagnetic field exposure through the implementation of Gaussian processes. This knowledge gap necessitates further investigation and exploration to establish a more robust understanding of the relationship between electromagnetic field exposure and its potential modeling methodologies. Future studies should aim to address this gap by conducting rigorous experiments and analyses to ascertain the efficiency and limitations of employing Gaussian processes for modeling EMF exposure.

1.2.2.3 Neural Networks and Matrix Completion

To the best of the authors' knowledge, artificial intelligence is only recently being applied in the area of RF-EMF exposure, but interest in this area is expanding. Only a few studies have utilized artificial intelligence to forecast the uplink (UL) and Downlink (DL) exposure of mobile phones. Specifically, some works have employed AI, such as Artificial Neural Network (ANN) models and machine learning models, to predict the power emitted by a mobile phone, which is equivalent to UL exposure [120, 50], as well as to estimate the DL exposure [170, 179]. The models for UL exposure prediction use readily available parameters, such as DL connection indicators (e.g., reference signal received power) and environmental information, as input features. The authors of [179] used measurement data from indoor and outdoor environments to account for realistic scenarios. They employed machine learning to estimate the levels of EMF exposure in the DL and UL. In [179], the authors used an artificial neural network to estimate exposure in urban areas using a limited amount of sensor data, and they did not consider full map reconstruction where environment infrastructure is taken into account. The previously described methods require reference to train the networks. Such full reference maps can however not be measured and simulated training sets need to be used. To avoid this requirement, standard kriging interpolation methods have been commonly used to infer electromagnetic field exposure. But neural network-based approaches have been shown to provide better performance [117, 160]. In [66], the authors take into account urban cognitive radio networks and estimate the power spectrum (PS) map using a Convolutional Neural Network (CNN)-based Generative Adversarial Network (GAN) [62]. In that work, 25 MHz and 75 MHz were used as the bandwidths, and a uniform distribution of users was assumed. A GAN model built on the basis of an autoencoder analogy was used to reconstruct images using the under-sampled power spectrum maps as input. To generate full PS maps for training, the authors used the inverse polynomial law model.

In [103], authors based on a self-supervised technique using GAN to generate a full radio frequency map of the selected area from an undersampled corrupted RF Map. In that work, to train the model, a weighted K-nearest neighbor algorithm is used to generate the reference. To mitigate training instability, an innovative lightweight reconstruction loss is introduced into the Self-supervised GAN's objective function, complementing the traditional adversarial loss. Additionally, it incorporates supplementary data, such as geographic information - an elevation map of the terrain as an additional input to the model, alongside observed measures of RF coverage and interference. These additional inputs are fed into the GAN framework to finely characterize the RF environment. In [110], authors estimated radio maps based on deep learning models. In that work, a few reference measurements along with side information such as - elevation maps and distance maps of base stations to measurement points to train the neural network models. They have employed Neural Architecture Search (NAS), a method that autonomously constructs an optimal Neural Network (NN) model architecture tailored to a specific task. Additionally, data augmentation techniques are used, which endeavor to tackle the constraint of limited labeled input data available for training. However, the measurement used as reference was considered a single measurement. In [179], authors estimated exposure in an urban environment from few sensor data using an artificial neural network. In that work, two neural network models are used - Hybrid ANN and conventional ANN architecture to reconstruct exposure maps from a few sensor data generated by simulations. Another approach explored in that work is using drive test data to estimate exposure maps. When using Hybrid ANN, authors used locally connected layers to the ANN model to imitate and reproduce the real propagation, locally-connected layers are constructed in parallel to process the inputs from the same base station antenna (BSA). Here, for exposure reconstruction from sensor data, inputs of ANN consist of distances to 10 nearest BSA, azimuth of antennas, locations of receivers, and time of the measurement. But full map reconstruction was not considered. In [16], EMF exposure was reconstructed using ANN models in the university campus in Turkey. In that work, multiple linear regression analysis and two different ANN models are used to estimate EMF exposure. The first ANN model was designed to have 9 input features to estimate EMF exposure as an output variable. In the second ANN model, only two input features are used (longitude and latitude) to predict exposure at a given location. They have compared the prediction results with real-world measurements at a specific location on the university campus. Two articles published recently [159, 79] presented deep learning methods for estimating radio maps. In [79], The mapping function used by the authors to estimate the propagation loss has two parts. The first part of the proposed method is a CNN to extract the features from the input map and in the second part of the proposed model, these extracted features by the CNN are used in the prediction part by a fully connected neural network (FNN). Using this information, one output variable is predicted by the proposed two-stage model as propagation loss.

Finally, several works have been done using matrix completion for radio map estimation [34, 74, 168, 167], avoiding the training phase with reference maps. In [181], authors used matrix completion for low-ranked matrices to construct radio maps in an indoor system.

1.2.2.4 Exposure Reconstruction as Missing Data

Several techniques for imputing missing values using machine learning methods rely on statistics gathered throughout the entire dataset and utilize supervised algorithms that depend on datasets containing complete observations to identify correlations between available data and missing data [22, 48, 56, 91, 37, 58, 184, 188, 192]. Imputing missing pixels in images with an unsupervised approach was implemented in [171, 30]. To explicitly describe observed and missing data, they introduced sparsity-aware neural network building blocks into a neural network-based learning system.

Missing data is frequent in sectors like healthcare and finance. Several time series applications, especially those in the area of medicine, have strived with the challenge of missing values [138]. Another avenue of research in this area uses deep learning techniques, such as variational autoencoders (VAEs) [7, 108, 129] or generative adversarial networks (GANs) [100, 194].

In [55], a generic framework for missing data imputation on time series is developed by combining concepts from VAEs [44], Cauchy kernels [84], Gaussian Processes [143], structured variational distributions with efficient inference [18] and a particular ELBO (Evidence Lower Bound) for missing data [129]. A new structured variational approximation, the non-linear dimensionality reduction in the presence of missing data is accomplished using the VAE method. In [46], authors designed variational graph autoencoders for matrix completion to infer air quality from a limited number of measurements. Deep matrix factorization [11] and nuclear norm minimization [144, 28] are examples of common methods for matrix completion to produce low-rank matrices. A low-rank completion is also often inefficient for image inpainting and reconstruction since it ignores local image structure [101, 190]. Several works used matrix completion for image inpainting/reconstruction [41, 172, 171], drug response imputation [73, 107, 142] and supervised and unsupervised infinitely wide neural network [191, 12, 165] for prediction. Recently in machine learning, in the realm of overparameterized neural networks, abundant parameters facilitate a flexible representation, potentially enhancing model performance and capturing intricate patterns enabling them for better generalization performance connecting them to kernel methods. Exploiting the infinite width limits of neural networks, recent work shows remarkable success in regression and classification tasks. Authors of [36] introduced an innovative approach for unsupervised 3D shape completion and reconstruction using incomplete scanned data. Their method involves crafting a deep prior based on the Neural Tangent Kernel (NTK) concept. Remarkably, the CNN-trained completion of shape patches exhibits a striking resemblance to pre-existing patches. This resemblance arises from their close proximity within the kernel feature space shaped by the NTK. Utilizing Convolutional Neural Tangent Kernel (CNTK) for predictive tasks across various classes on the CIFAR-10 dataset has been explored in the works of Arora et al. [12] and Li et al. [102]. In the research by Arora et al. [12], the application of CNTK demonstrated enhanced performance for optimization and generalization. Notably, this study provided a non-asymptotic proof, establishing the equivalence between a fully-trained, sufficiently wide neural network and the kernel regression predictor with NTK. Within the context of the CIFAR-10 dataset, CNTK was implemented to predict different class labels, yielding a noteworthy accuracy improvement of 10% compared to conventional methodologies. In the study by Fan et al. (2020) [51], they present another instance of polynomial matrix completion applied to incomplete data through a transductive learning approach. The researchers introduce a novel technique leveraging kernels on synthetic data, subspace clustering for incomplete data, as well as data recovery from motion capture and classification tasks involving incomplete data.

The following table 1.3 presents a comprehensive overview of exposure reconstruction techniques utilized from 2019 onwards. These methods are commonly employed in scientific research to estimate and reconstruct exposure levels in various contexts. By leveraging advanced statistical models and data analysis techniques, these approaches enable researchers to approximate historical exposure levels with a reasonable degree of accuracy, thus contributing to a deeper understanding of past events and their potential implications.

Technique	Year	Evaluation Metrics	Scenario	Data Type	Training required	No. of output maps
[179]	2020	MSE R^2	Outdoor	Simulations	yes	one
[120]	2021	MAE, R^2 RMSE	Indoor	Drive test	yes	one
[112] ours	2022	PSNR, SSIM	Indoor	Sensor simulations	yes	time dependant multiple maps
[178]	2022	MSE RMSE CDF of Prediction	Outdoor	Drive test	yes	one
[113] ours	2022	CDF,PDF of error ratio PSNR, SSIM	Outdoor	Sensor simulations	yes	time dependant multiple maps
[16]	2022	measurement comparison	Outdoor	real measurement	yes	measurement points
[31]	2023	CDF RMSE	Outdoor	Drive test	yes	one
[111] ours	2023	CDF,PDF of error ratio PSNR SSIM	Outdoor	Sensor simulations	yes	time dependant multiple maps
[183]	2023	CDF, CCDF	Outdoor	Drive test	yes	one
EME-CNTK ours	2023	MSE CDF,PDF absolute error	Outdoor	Sensor simulations	yes	time dependant multiple maps

Table 1.3: List of exposure reconstruction techniques by ML

1.3 Contributions

As per MEL's requirement, our research was conducted to reconstruct EMF exposure in Wazemmes and Euratech area in Lille City, France. In Wazemmes and Euratech areas 50 and 20 sensors are deployed respectively. Sensors are deployed on lamp posts in both of the areas and sensor locations are depicted in Figure 1.4. Our research on EMF exposure reconstruction with AI started in 2020-2021, and the sensors are deployed and functional in 2022-2023. Therefore, we have experimented on Lille City center, France during the sensor deployment time.

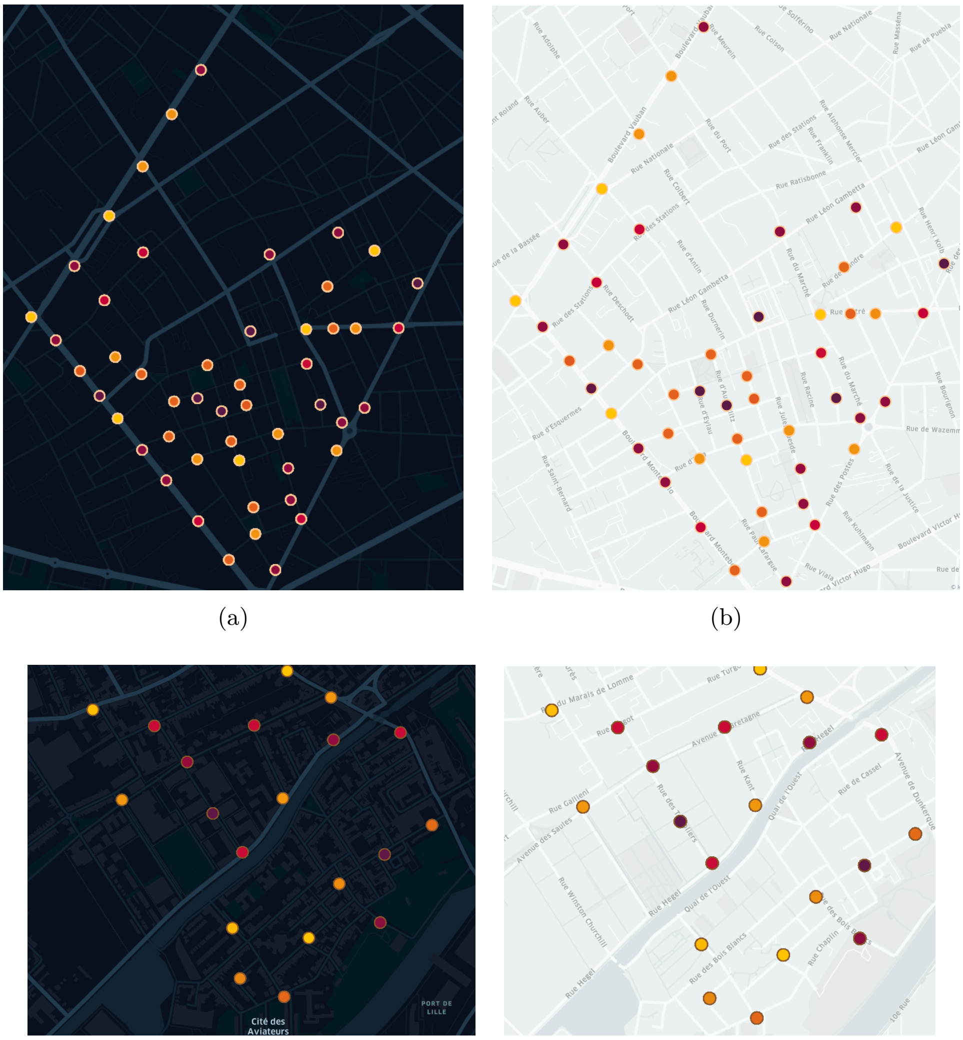

(a) (b)

(c) (d)

Figure 1.4: Sensor location in colored circles in **(a,b)** Wazemmes and **(c,d)** Euratech area

In this thesis, two main techniques based on AI tools are proposed.

- ⋆ **EMF exposure map reconstruction with generative models** - In this method, we proposed a conditional generative adversarial network for image-to-image translation task. From a few sparsely distributed sensors generating the full exposure map of the selected area is done by converting it into an image reconstruction task. We require reference or reference images to train the cGAN model. We have used Veneris-Opal, an open-source ray tracing simulator to generate the full exposure maps or reference images for training the model.
- ⋆ **EMF exposure map reconstruction with infinitely wide CNN** - it is quite difficult to access the full exposure map used in cGAN method in reality. In that case, we have proposed a method based on Infinitely wide CNN to impute missing data in a matrix. A convolutional neural tangent kernel CNTK is constructed in our proposed method and using only 60 sensor values the exposure maps are reconstructed in the selected area of interest.

Our study aims to investigate the capability of neural networks in extracting intricate features and their correlations with signal strength within a given local area or similar settings. Additionally, we explore how effectively these networks can consider environmental factors. We have utilized a convolutional neural network with infinitely long width-based matrix completion and reconstruction using generative models that are tailored to the exposure reconstruction task.

1.4 Plan of document

The thesis is organized as follows:

- ⋆ In chapter 2, we address the above mentioned issues with our novel methodologies for indoor and outdoor scenarios. This chapter is divided into three sections:
    - ⋆ Section A contains the preliminaries required for the methodologies developed such as datasets, simulators, and machine learning basics.
    - ⋆ Section B describes exposure reconstruction methods using **convolutional neural network** and **conditional generative adversarial networks** for indoor and outdoor settings.

- ⋆ In chapter 3, the evaluation of our methods is presented.
- ⋆ In chapter 4, Finally, the discussion and future perspectives are drawn.

Publications

This section summarizes the publications, conferences, and collaborations based on work that I have done during my Ph.D. candidature.

Journal Papers

- ⋆ **Mallik Mohammed**, Angesom Ataklity Tesfay, Benjamin Allaert, Redha Kassi, Esteban Egea-Lopez, Jose-Maria Molina-Garcia-Pardo, Joe Wiart, Davy P. Gaillot, and Laurent Clavier, "Towards Outdoor Electromagnetic Field Exposure Mapping Generation Using Conditional GANs." *Sensors 2022, no. 24*, vol 9643. MDPI

International Peer-reviewed Conference Papers with proceedings

- ⋆ **Mallik Mohammed**, Sofiane Kharbech, Taghrid Mazloum, Shanshan Wang, Joe Wiart, Davy P. Gaillot, and Laurent Clavier. "EME-Net: A U-net-based Indoor EMF Exposure Map Reconstruction Method." in.*In 2022 16th European Conference on Antennas and Propagation (EuCAP), IEEE*, pp. 1-5, 2022.
- ⋆ **Mallik Mohammed**, Benjamin Allaert, Joe Wiart, Davy P. Gaillot, and Laurent Clavier. "EME-GAN: A Conditional Generative Adversarial Network based Indoor EMF Exposure Map Reconstruction." in.*In 2023 23rd Gretsi*, pp. 1-5, 2022.
- ⋆ Esteban Egea Lopez, **Mallik Mohammed**, Laurent Clavier, Davy P Gaillot. "Generation of electromagnetic exposure maps for 5G communications" , *submitted In 2024 18th European Conference on Antennas and Propagation (EuCAP), IEEE, Glasgow, England.*
- ⋆ Angesom Ataklity Tesfay, **Mallik Mohammed**, Eric Pierre Simon and Laurent Clavier. "Deep Learning-based Serial Interference Cancellation to Improve Uplink in LoRa Networks." in.*In 2023 23rd Gretsi*, pp. 1-5, 2023.

International Conference paper without proceedings

- ⋆ **Mallik Mohammed**, Joe Wiart, Davy P. Gaillot, and Laurent Clavier. "A UNet based Indoor EMF Exposure Map Reconstruction." *In COST CA20120 INTERACT, Bologna, Italy* June, 2021.
- ⋆ **Mallik Mohammed**,Angesom Tesfay, Benjamin Allaert, Esteban Egea Lopez, Jose Maria Mollina, Joe Wiart, Davy P. Gaillot, and Laurent Clavier. "Towards Outdoor Electromagnetic Field Exposure Mapping Generation Using Conditional GANs" in.*In COST CA20120 INTERACT, Lyon, France*, Feb. 2022.
- ⋆ **Mallik Mohammed**, Angesom Tesfay, Joe Wiart, Davy P. Gaillot, and Laurent Clavier. "A GAN and LSTM model Based Spatio-Temporal Electromagnetic Field Exposure Prediction Method" in.*In COST CA20120 INTERACT, Valencia, Spain*, Sept. 2022.
- ⋆ **Mallik Mohammed**, Joe Wiart, Davy P. Gaillot, and Laurent Clavier. "A Fast Method to Reconstruct Urban Electromagnetic Field Exposure by Matrix Completion with infinitely wide Neural networks." in *In COST CA20120 INTERACT, Barcelona, Spain*, April. 2023.
- ⋆ **Mallik Mohammed**, Joe Wiart, Davy P. Gaillot, and Laurent Clavier. "EMF Exposure Reconstruction with Neural Networks" in *In COST CA20120 INTERACT, Poznan, Poland*, September. 2023.

Journal Papers in progress:

- ⋆ **Mallik Mohammed**, Joe Wiart, Benjamin Allaert, Esteban Egea-Lopez, Davy P. Gaillot and Laurent Clavier, "Matrix completion," In *IEEE Access*, vol. 8, pp. 199001-199015, 2023.
- ⋆ **Mallik Mohammed**, Angesom Tesfay, Joe Wiart, Davy Gaillot, Laurent Clavier. "Predicting Spatio-Temporal EMF exposure by Neural Networks Networks, in Métropole Européenne de Lille using drive test data."
- ⋆ Norel Islam, **Mallik Mohammed**, Esteban Egea Lopez, Jose-Maria Molina-Garcia-Pardo, Joe Wiart, Martine Liénard, Davy Gaillot, Laurent Clavier. "Comparison of real world data and simulated data MA-MIMO."

International Conference Papers with proceedings peer reviewed in progress

- ⋆ **Mallik Mohammed**, Esteban Egea Lopez, Jose-Maria Molina-Garcia-Pardo, Joe Wiart, Davy Gaillot, Laurent Clavier. "EME-GAN-V2 : A generative model for exposure reconstruction in urban area with beam forming."
- ⋆ Nor El Islam Dahmouni, Mohammed Mallik, Pierre Laly, Davy P. Gaillot, Esteban Egea Lopez. "A Comparative Analysis of SISO Stationarity Time and Pathloss in Suburban Environments Using Veneris Ray Tracing and Real Data.", in VEHICULAR 2024: International Conference on Advances in Vehicular Systems, Technologies, and Applications, Athens, Greece.
- ⋆ Angesom Ataklity Tesfay, **Mallik Mohammed**, Eric Pierre Simon and Laurent Clavier. "Deep Learning-based Serial Interference Cancellation to Improve Uplink in LoRa Networks." in *IEEE MeditCom 2023: IEEE International Mediterranean Conference on Communications and Networking 2023 IEEE ComSoc Portfolio Event*, pp. 1-5, 2023.

Chapter 2

EMF Exposure Reconstruction Techniques

Preliminaries

This chapter outlines the proposed AI-driven techniques for reconstructing the exposure to EMF in outdoor and indoor settings. It is divided into three sections. The first section details the preliminaries, such as the datasets and simulators. The second section describes different neural network architectures used for exposure reconstruction for both outdoor and indoor settings. Finally, the third section presents a novel method for exposure map reconstruction through the use of an infinite-width CNN for matrix completion.

2.1 Dataset: Reference Maps

In our study, two unique datasets are utilized for outdoor and indoor exposure measurements with respect to multiple base stations and wi-fi access points namely 'VenerisLilleExposure' and 'IndoorExpMap' Dataset, respectively to train the neural network models. The first dataset was created using the Ray-Tracing tool Veneris-Opal [49]. The second dataset was created using Pylayers [9], an open-source propagation modeling tool for indoor environments.

2.1.1 Indoor Scenario

IndoorExpDataset For indoor simulations, we consider a customized version of the environment WINNER-II A1 [122]. The considered building is a single floor which represents a typical multi-room office environment where the floor area is $2100m^2$, room dimensions are $10m \times 10m \times 3m$, and the corridor has the dimensions $70m \times 10m \times 3m$. Windows are located on the north and south side of the office environment. Each room has a wooden door, and the walls are constructed with plaster with a thickness of 10 *cm*. The ceiling and floor are made using reinforced concrete. The indoor office model layout is illustrated in Figure 2.1. Materials used to construct the rooms and their properties are given in Table 2.1.

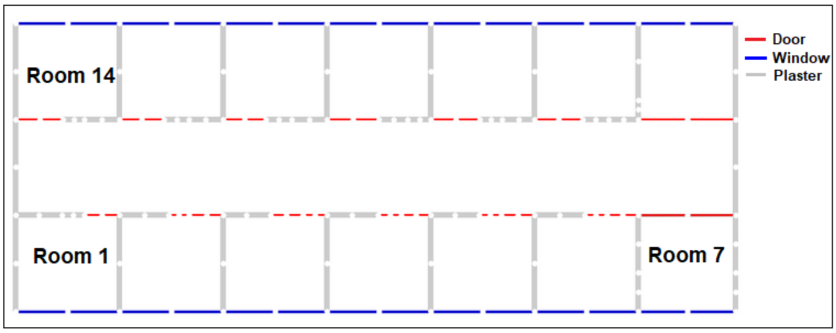

Figure 2.1: Layout of the indoor scenario.

These properties are implemented in 'PyLayers' for the simulations. For training the model, several Wi-Fi access points are considered with different location scenarios while keeping two or three of them in the corridor and three in the rooms. 'PyLayers' is an open-source radio-channel wave propagation simulation tool [9]. Using 'PyLayers', we simulate the received power maps in a dense environment; then, we employ them as reference maps (see Figure 2.3).

Description	Wall	Air	Ceiling	Floor	Door
Material	Plaster	Air	Reinforced concrete	Reinforced concrete	Wood
Relative permeability μ_r	$1 + 0j$	$1 + 0j$	$1 + 0j$	$1 + 0j$	$1 + 0j$
Relative permittivity ε_r	$8.0 + 0j$	$1 + 0j$	$8.09 + 0j$	$8.09 + 0j$	$8.3 + 0.02j$
Sigma conductivity s/m	0.308	0	0	0	0
Thickness in cm	10	2	10	10	5
Manning's roughness	0.0	0.0	0.012	0.0	0.0

Table 2.1: Properties of the environment materials.

Five pixels in each room and 26 pixels in the corridor, 96 pixels were taken from the reference map to generate the sensor measurement maps. Sensor measurement locations as the incomplete image are shown in Figure 2.2. We consider 15, 30, 50, 70, 90 pixels taken from the reference map images for the test sets. It is worth noting that, for the most optimistic scenario, i.e., when 115 measures or pixels are considered, we cover less than 1% of the reference image area.

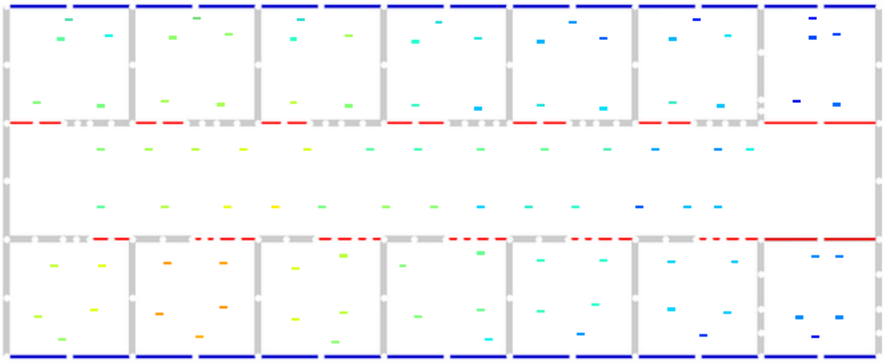

Figure 2.2: Input sensor measurement map with 96 pixels from the reference map.

The Wi-Fi hotspots are omnidirectional with orthogonal and parallel polarization. Generating the EMF exposure maps considers the multi-wall and multi-frequency home environment path loss model [88]. The path loss is calculated taking into account that the direct line between Tx and Rx crosses several kinds and amounts of walls added to the free space log-distance path loss:

$$PL(d)[dB] = PL_0(d_0) + 20log_{10}(d/d_0) + \sum_{i=1}^{M} k_i L_i + X\sigma,$$

where $PL(d)$ is the path loss at a Tx - Rx distance equal to PL_0 at a reference distance d_0 equal to 1m is the path loss, k_i is the number of walls of type i crossed by the line-of-sight, the total number of different kinds of wall is M, L_i is the penetration loss of wall type i, and X_σ is a zero-mean gaussian random variable with a standard deviation σ. The value for $PL_0(d_0)$ and X_σ for a Wi-Fi radio technology at frequency band 2.4 - 2.5 GHz are 27.75 dB and 5.94 dB respectively.

Reference maps are generated using the features of propagation, the type of material used to construct the wall, the wall penetration loss, the relative permeability and permittivity, the conductivity, and the thickness of walls. Figure 2.3 shows examples of reference reference indoor exposure map images when the Wi-Fi access points are at different locations in the room.

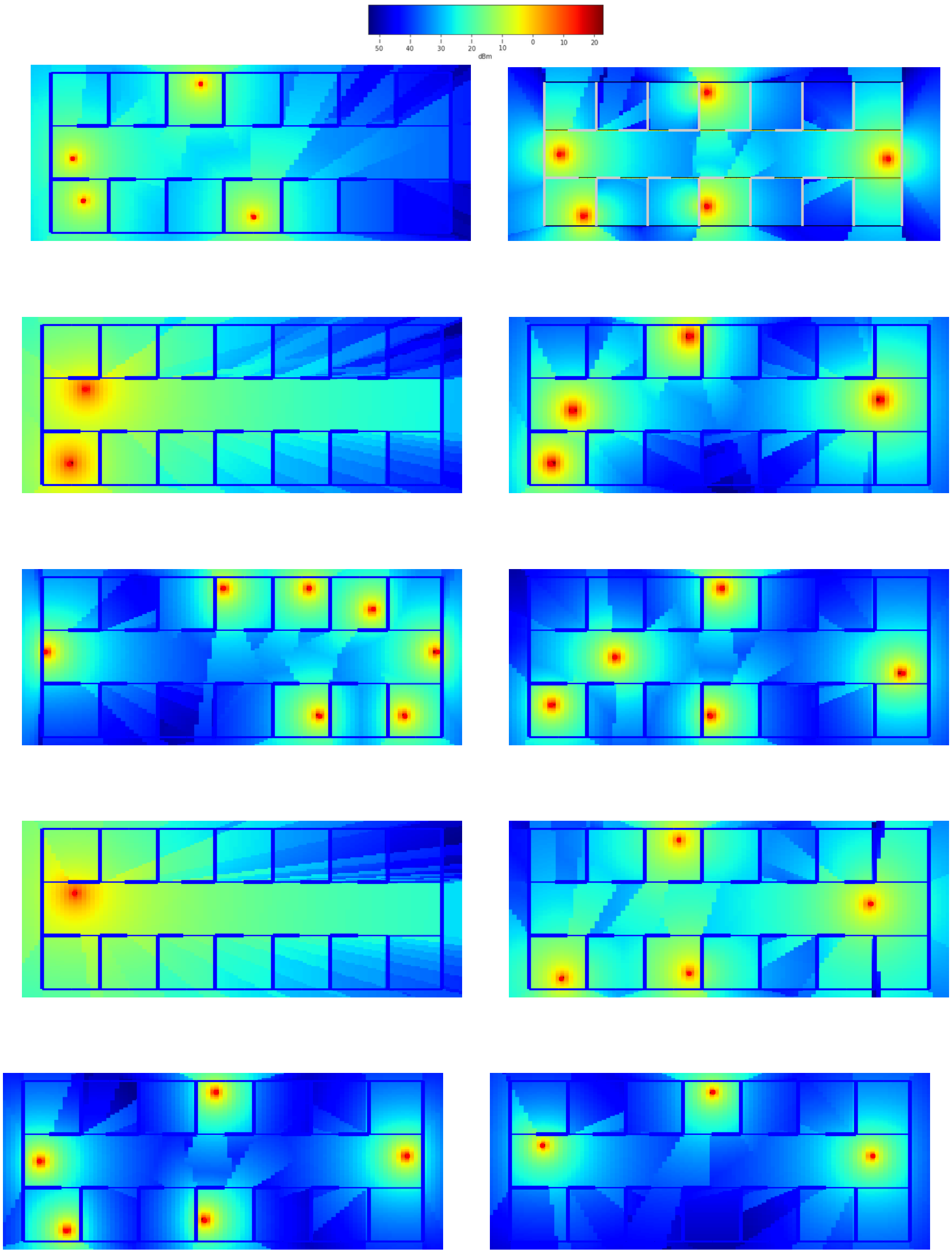

Figure 2.3: RF-EMF exposure reference map images with different Wi-Fi access points locations are used to generate reference / reference maps using PyLayers

2.1.2 Outdoor Scenario

Simulator and Dataset Generating large open-source datasets made of real data can be difficult in the area of data-based research and machine learning. As a result, synthetic data can be generated alternatively or as a complement to using real data through deterministic simulations. For our study, we utilized three separate databases of outdoor exposure measurements regarding multiple base stations. The first was created through an open-source Ray-Tracing tool **Veneris-Opal** in Lille, France, in the context of this Ph.D. work.

Veneris-Opal is a simulation framework for research on Vehicular Networks and cooperative automated driving [49], which can also be used for general wireless networks simulation requiring 3D environment-aware propagation simulation. The tool was developed at Universidad Politécnica de Cartagena, Spain, and made available to the public. Veneris consists of a traffic simulator that utilizes the Unity game engine [64] and comprises a realistic vehicle model, as well as driving and lane change behaviors that replicate traffic dynamics. Also included are a ray-launching GPU-based propagation simulator known as Opal, and a collection of modules that allow bidirectional coupling with the extensively employed OMNET++ network simulator [174].

In an interactive 3D environment, Veneris enables a realistic microscopic road network simulation through a collection of Unity components and related assets, developed with NVIDIA PhysX. The scenario elements, such as roads, intersections, traffic lights, or buildings, are generated using Builder components. Meanwhile, Vehicle components model the dynamics of the vehicle and how they behave on the roads, intersections, and interact with other vehicles. Communication components are responsible for implementing the communication with simulation modules. An example of the 3D environment of Lille city center in Veneris is illustrated in Figure 2.4.

To simulate multipath channel propagation with NVIDIA Optix [136] for multiple moving transmitters and receivers, **Opal** library in Veneris is used. This simulator is based on 3D ray launching, which is a deterministic radio-frequency propagation technique. The rays are propagated along their path until they encounter an obstacle, where they are reflected, diffracted, transmitted, or scattered. Afterward, subsequent rays are traced, and the contributions of all rays hitting a reception

Figure 2.4: Snapshot of Lille city center in Veneris. Pink, green and light blue represents road cross sections, park and buildings respectively.

sphere on the receiver are added to compute the electric field. Further information on open-sourced Ray-Tracing simulator Veneris-Opal can be found in [49].

Particularly in the areas of machine learning and data-based research, large open-source datasets with actual data are often hard to come by. Deterministic simulations can, however, sometimes be used to generate synthetic data that can be used instead of or in addition to real data in certain circumstances.

Environment Infrastructure - OpenStreetMap The environment and infrastructure, among other things, have an impact on how signals in telecommunication networks propagate. Signal attenuation, reflection, and diffraction can all be caused by structures like buildings, roads, cars, and trees. Signal loss, interference, and distortion can occur as a result of the signal's interaction with the surrounding environment. Therefore, in our generative model-based method we have utilized in city topology image as a conditional input to the CNN-based generative models. The city topology image is taken from OpenStreetMap in QGIS using a Python plugin to extract raster images to Portable Network Graphic (PNG) format. The city topology of Lille, France is illustrated in Figure 2.5. The image size is 512 × 512 × 3 and black and white represent buildings and roads, respectively. This image is used as a conditional input for the proposed cGAN method which is described in the later sections.

Figure 2.5: city topology

VenerisLilleExposure is a dataset comprising maps of outdoor exposure that were simulated in an urban cellular environment using a ray-tracing propagation tool called Veneris-Opal of 3003 simulated EMF exposure maps in Lille, France. The context in which the measurements were taken was that of a 5G network with multiple transmitters. Such a deterministic instrument explicitly assumes the electromagnetic interactions of a multipath radio signal between the transmitter and a receiver by using both deployment details (typically, the mobile nodes' relative locations and base stations) and an explanation of the physical setting (such as a city plan featuring a detailed description of buildings and their constituent materials). Lille city center, France was selected as the target region of interest for exposure reconstruction. The overall scene is $1000m \times 1000m$, each pixel being $1.5m \times 1.5m$, thus forming a matrix of size 512 × 512. The area considered in these simulations is located in Lille city center from Place de la Republique, Le nouveau Siecle, Gare de Lille Flandre and Centre du service national et de la jeunesse (CSNJ) de Lille as shown in figure 2.6 as google reference of the target RoI. For each pixel, the exposure value was simulated with respect to 3 different 5G Base Stations. Different moving transmitter positions are used in order to generate different maps. In Figure 2.7 one transmitter in Veneris simulation scenario is shown.

Figure 2.6: google reference map for ROI

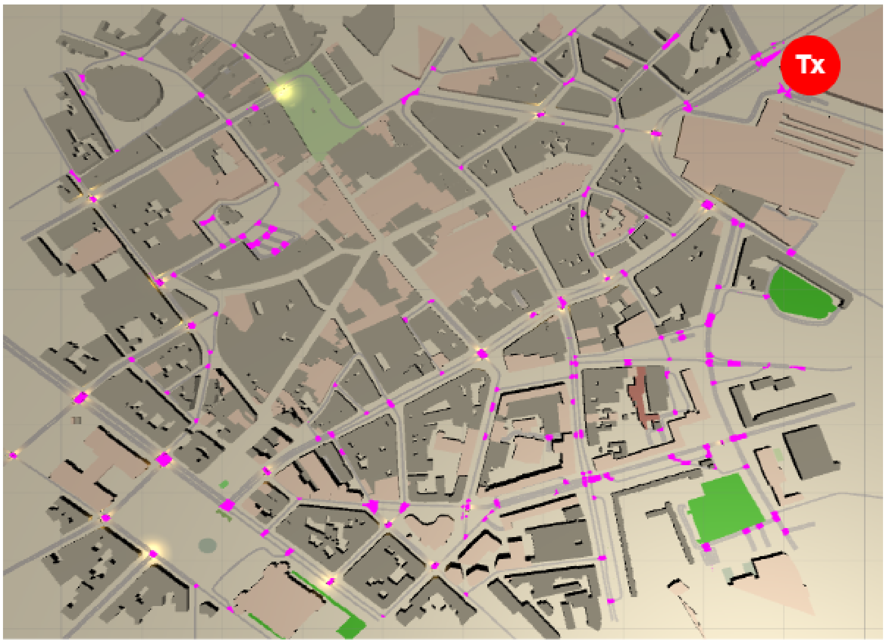

Figure 2.7: Transmitter in red in VEneris simulator

The dataset contains objects with rough surfaces like 3D building walls, statues, roads, etc., interacting with the rays in complex ways. Moreover, gaps in the object, e.g., bridges and rays at different levels, can pass or reflect from such objects. The presence of the object in the environment, and several ray interactions result in a complex power distribution representing a real-life environment. The transmitters are assumed to use an isotropic antenna, producing omnidirectional radio waves. The height and power of the transmitting antenna were set at a maximum of 15 $meters$ and 20 $Watts$, respectively. The height is selected as 20 $meters$ as an average height in the selected area of interest. The propagation model in ray launching considers reflections on 3D buildings, resulting in more complex patterns. Even if VENERIS can handle a very high number of iterations, a convergence study shows that 2 interactions are enough for reliable results in this kind of environment. For simulations, three transmitters are used at different locations, one for each simulation at 5.89 GHz with 20 W transmitting power, and other simulation parameters are used, like azimuth, elevation, reflection, etc. To generate the reference maps, 2088 receivers at the height of 1.5 $meters$ are placed in a uniform grid in the area of interest, as shown in Figure 2.8. The receivers inside buildings have 0 values in simulations to generate data. There are approximately 1269 receivers in outdoor locations. Nonetheless, this number of points is sufficient to capture the dynamics of the field and train the model. The data from Veneris simulations are saved in CSV format. Then we can resize the image using different upsampling or downsampling

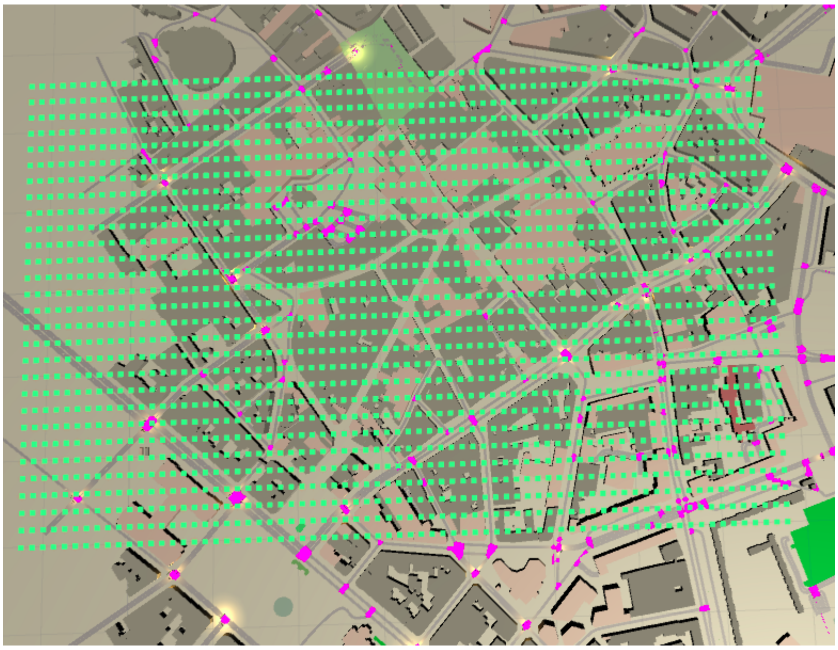

Figure 2.8: Three-dimensional environment model of Lille City 1 km2 area with 2088 receiver grid represented in green squares.

methods provided in Pillow or OpenCV library. This process can also be done using numpy [68] and opencv library using a 'percentile' object from numpy library to create a cluster of power values from the CSV data. Then using OpenCV provided 'applycolormap' method the image can be created with the required image size.

Figure 2.9 gives examples of reference reference exposure map images when the transmitter is at different locations. Each map has a dimension of 512 height, 512 width, and 3 RGB color channels. In Veneris-Opal simulations, the data is generated on time steps. Thus, 3003 map images at each time step (Tx location is changing) are used as reference real images to train the CNN based conditional generative model.

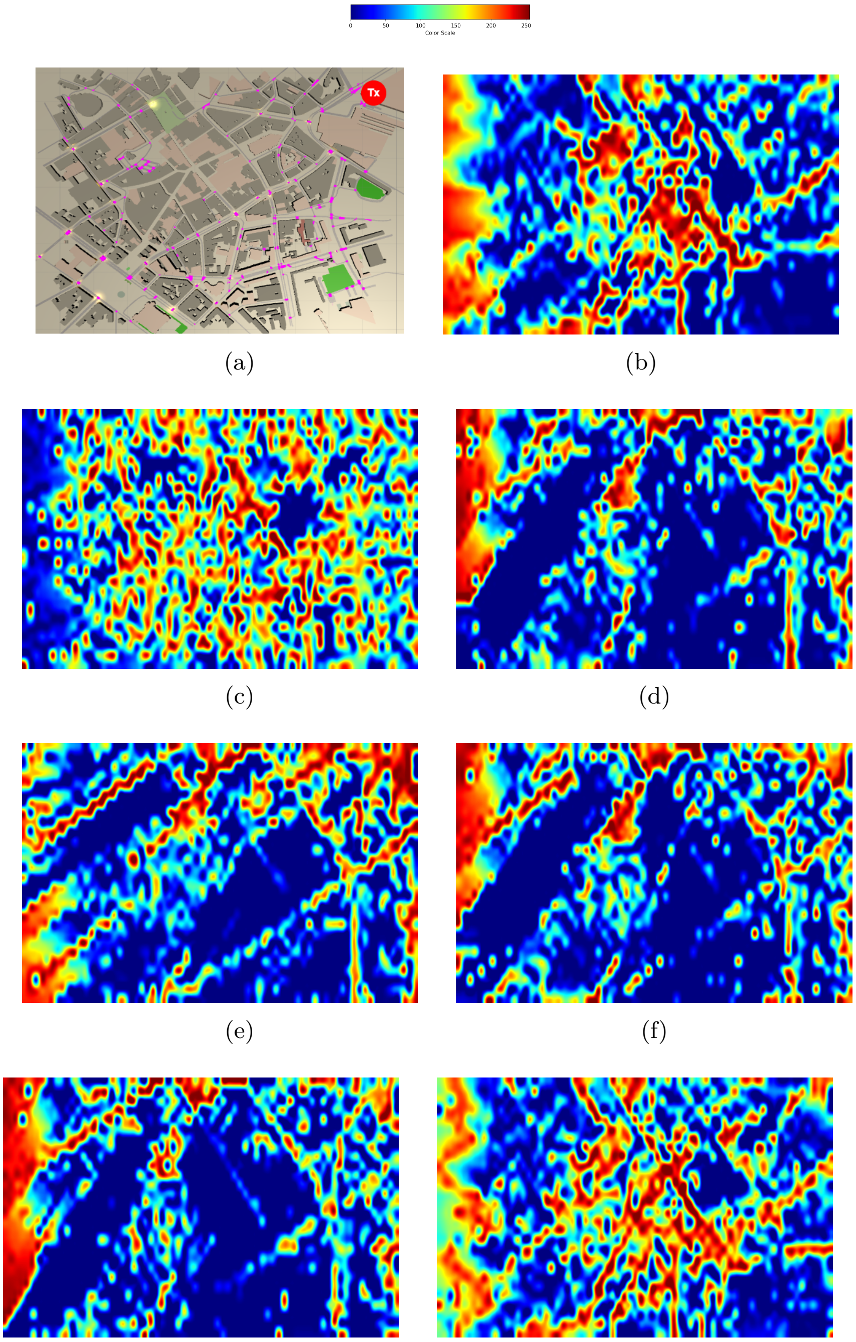

(a) (b)

(c) (d)

(e) (f)

(g) (h)

Figure 2.9: RF-EMF exposure reference map images with different transmitter locations are used **a)**In Veneris: Transmitter at upper right corner, **b)** transmitter at center, **c)** 2 transmitters at middle, **d)** upper right corner, **e)** bottom left corner, **e)** upper right corner, **f)** bottom left corner, **h)** transmitter moved towards bottom left corner

Dataset for Matrix completion The region of interest (RoI), Lille city center, is an area of 1 km^2. To evaluate the performance of the method, a 1.5-meter height grid is defined as sensor locations as shown in Figure 2.10. Two different scenarios are considered: one or two transmitters are placed in the RoI. The exposure data for the sensors were generated for 20, 40, 60, and 100 sparsely located sensors using Veneris-Opal. Different Transmitter positions were used in order to generate different reference maps and sensor values. Moreover, to implement the city topology effect in the proposed method, the environment (buildings, roads, etc.) has been extracted from OpenStreetMap [134] as a polygon. The dataset consists of matrices, where each matrix is $\gamma \in \mathbb{R}^{m \times n}$, where m and n are the row and column of the matrix.

The goal of matrix completion is to impute the unseen entries in a matrix γ given that only a subset of its coordinates has been observed. An example of the matrix γ is depicted in Figure 2.10.

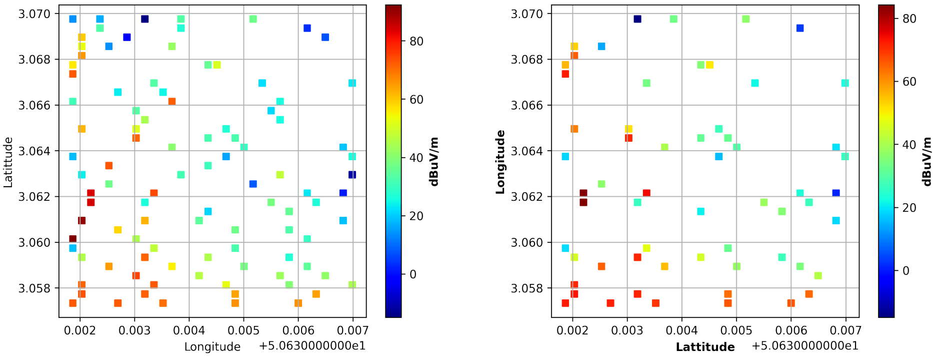

(a)

(b)

Figure 2.10: Matrix γ with **(a)** 100 sensors and **(b)** 60 sensors in $1km^2$ area

2.2 Machine Learning

Machine Learning (ML), a fascinating topic in computer science, enables machines to generate predictions without the requirement for explicit training. By utilizing inference, ML entails training a computer on a small group of samples known as the training set and then using the learned model on new data. As it combines knowledge from other study fields, this area of informatics draws academics from a variety of backgrounds, including psychologists, neuroscientists, computer scientists, and statisticians, among others.

Due to the growing accessibility of computational resources, the advent of open-source machine learning programs, and the growth of large-scale data sets, the field has witnessed an increase in attention recently. Natural language processing, computer vision, medicine, banking, social networks, signal processing, digital advertising, and other fields have all found use for ML because of its capacity to enhance existing results, uncover hidden patterns, or resolve challenging mathematical problems.

Based on factors like the current problem, the volume of available data, and its characteristics, there are numerous learning paradigms. Generally speaking, these paradigms fall into one of three categories: supervised learning, unsupervised learning, and semi-supervised learning.

- ⋆ Supervised learning aims to discern the connection between inputs and their intended outcomes through the utilization of a training set containing a finite collection of instance-output pairs. If the outputs are discrete, the task is referred to as classification, whereas if the outputs are continuous, it is known as regression.
- ⋆ In unsupervised learning, clustering is a crucial activity that is centered on the lack of output examples. By utilizing the training data's inherent structure, which groups together comparable cases, the main goal is to find clusters. Without relying on explicit output information, the goal in these situations is to identify patterns and relationships. By revealing links between data points through unsupervised learning, clustering reveals important insights that lead to a deeper comprehension of the underlying patterns and structures.
- ⋆ Semi-supervised learning, which falls between the two preceding frameworks, makes use of both labeled and unlabeled training data to determine the re-

lationship between input instances and the related outputs. Its goal is to combine the structure of the unlabeled training data with the label information found in the labeled training set. In the absence of fully labeled datasets, semi-supervised learning can be a useful approach in various domains such as computer vision, natural language processing, and speech recognition.

This chapter aims to give a clear understanding of the frameworks of supervised learning and semisupervised learning, which are both included in our study. In Section 2.2.1.1, we will go into supervised learning and clarify the design ideas that underlie all supervised learning models. We shall concentrate particularly on the Neural Networks models used in this thesis. Additionally, Section 2.2.1.2 explains the semi-supervised learning framework and foundation for building SSL models. These subjects will be thoroughly covered in this chapter's remaining sections.

2.2.1 Classical Machine Learning

2.2.1.1 Supervised Learning

The goal of supervised learning algorithms is to identify the general predictor, sometimes referred to as the mapping function, that links the input space $\mathcal{X}$ and the output space $\mathcal{Y}$. Through the use of a training set made up of pairs of observations and related outputs, the goal is to select this mapping that will have the lowest likelihood of mistakes when applied to unobserved examples.

Core Concept The practical application is the design of a loss function that assesses the degree of agreement or disagreement between a prediction and the anticipated output, frequently referred to as the label. The learning process then chooses the prediction function that minimizes the average error displayed in the training data. This concept is known as "Empirical Risk Minimization" (ERM). The empirical risk must be decreased in order to construct a prediction function with a low generalization error, which results in fewer errors when applied to new cases. The key premise is that these fresh cases are exactly like the training examples that were used to develop the prediction function. Consequently, statistical learning theory's theoretical foundation centers on exploring the correlation between empirical error and generalization error [173].

Definitions and notations Throughout this thesis, we will introduce the terminology and notations essential for our discourse, commencing with specific illustrative instances comprising observations and target outputs. For a given integer

$d \in \mathbb{N}$, each observation is denoted by a collection of features defined in a vector space $\mathcal{X}$, commonly denoted as $\mathcal{X} \subset \mathbb{R}^d$. The associated result is called the target output, and it is considered to be a member of an output set $\mathcal{Y}$. In this case, an element of $\mathcal{X} \times \mathcal{Y}$ is represented by (x, y).

The fundamental assumption of ML rests on the notion that all instances are dispersed autonomously and uniformly independent and identically distributed (i.i.d.) through an established albeit unfamiliar probability distribution $\mathcal{D}$. Consequently, for any given set $\mathcal{S}$, its instances (x_i, y_i) within $\mathcal{S}$ are expected to be produced independently and identically in accordance with $\mathcal{D}$. Next, we establish that $\mathcal{S}$ is an i.i.d. sample conforming to $\mathcal{D}$. In a less formal sense, this assumption delineates the concept of the representativeness of a training set and a test set concerning the given problem. Both the training examples and test observations, along with their corresponding expected outcomes, are produced independently and identically from the same probability distribution.

The second foundational principle in machine learning revolves around the notion of error, frequently denoted as risk or loss. Assessing the concordance between the prediction is key in this context. $f(x)$ and the desired output y for a given observation $x \in \mathcal{X}$ in the class of functions $\mathcal{F} = \{f | f : \mathcal{X} \to \mathcal{Y}\}$, a loss function $\ell : \mathcal{Y} \times \mathcal{Y} \to \mathbb{R}_+$ is employed. The quantification of the similarity between the expected and desired outputs is intuitively captured by $\ell(f(x), y)$, typically defined as a distance across the set of outputs $\mathcal{Y}$.

In binary classification, where $\mathcal{Y}$ is the set $\{-1, +1\}$, the prevalent loss function is typically the 0/1 loss, denoted as (2.1):

$$\ell(f(x), y) = \mathbb{1}_{f(x) \neq y}, \tag{2.1}$$

where $\mathbb{1}_\pi = 1$ is predicate π is true and 0 otherwise.

In regression, where $\mathcal{Y} = \mathbb{R}$, the most commonly used losses are the absolute error defined in Eq. (2.2):

$$\ell(f(x), y) = |f(x) - y| \tag{2.2}$$

and the square loss :

$$\ell(f(x), y) = |f(x) - y|^2. \tag{2.3}$$

Generalization and Empirical Risk minimization In Eq. (2.4), the expression for the generalization error of a prediction function $f \in \mathcal{F}$ is articulated based on the provided definition.

$$\mathcal{L}(f) = \mathbb{E}_{(x,y)\sim\mathcal{D}}(\ell(f(x),y)) = \int_{\mathcal{X}\times\mathcal{Y}} \ell(f(x),y) d\mathcal{D}(x,y) \tag{2.4}$$

The function of interest in our case, denoted as f and belonging to the set $\mathcal{F}$, is the one that yields the minimum prediction errors when applied to new data. Consequently, it possesses the lowest generalization error. However, due to the unknown probability distribution $\mathcal{D}$, it is not possible to calculate this generalization error. In 1998, it was demonstrated by Vapnik [173] that a consistent search for the function f can be achieved by reducing the mean error of f over a training set $\mathcal{S} = (x_i, y_i)_{1\leq i\leq m}$, which is generated independently and identically (i.i.d.) from $\mathcal{D}$. This value is referred to as the empirical risk of f on $\mathcal{S}$ and serves as an unbiased estimation of the generalization error:

$$\hat{\mathcal{L}}(f,S) = \frac{1}{m}\sum_{m}^{i=1} \ell(f(x_i),y_i) \tag{2.5}$$

Minimization of Empirical Risk The prediction function $f_S : \mathcal{X} \to \mathcal{Y}$ is outputted by a learning algorithm when a training set $\mathcal{S}$ is given as input. The function $\mathcal{A}$, which is a learning algorithm, searches for the function f_S within a class of functions referred to as $\mathcal{F}$. The ERM algorithm can be intuitively understood in the following way.

The generalization error $\mathcal{L}(f)$ can be accurately calculated by the empirical error $\hat{\mathcal{L}}_{\Updownarrow}(f,S)$ if the distribution $\mathcal{D}$ is appropriately represented by the training instances in $\mathcal{S}$. As a result, on a particular training set $\mathcal{S}$, the empirical error is minimized in order to reduce the generalization error. The ERM principle returns the function f_S when given $\Updownarrow$ samples in a training set $\mathcal{S}$, and a class of functions $\mathcal{F}$ with a loss function $\ell : \mathcal{Y}\times\mathcal{Y} \to \mathbb{R}_+$:

$$f_S = \underset{f\in\mathcal{F}}{\operatorname{argmin}} \frac{1}{m} \sum_{(x_i,y_i)\in\mathcal{S}} \ell(f(x_i),y_i) \tag{2.6}$$

The practical method involves training over a continuously differentiable upper bound of the empirical loss in eq. (2.6), also known as the surrogate loss, to create a real-valued prediction function $h_w : \mathcal{X} \to \mathbb{R}$. The classification function is thereafter defined as this function's sign. In light of this, the function $f(x)$ equals the sign of $h_w(x)$ for every x in the set of real numbers $\mathbb{R}$, that is $\forall x \in \mathbb{R}, f(x) = sgn(h_w(x))$.

The objective is not solely focused on minimizing empirical error, but rather on minimizing generalization error. Hence, the ERM approach loses its value if the function f_S, despite having a low empirical error, exhibits a high generalization error. Consequently, we can expect the ERM method to possess the ability to generalize, indicating that the empirical error of f_S can be a reliable indicator of generalization error. As long as this condition of generalization holds, we can confidently assume that if ERM yields a function f_S with low empirical error, its generalization error will also be low.

It is important to note that the ERM approach operates inside a predetermined and constant set of $\mathcal{F}$ with the aim of identifying the function with the lowest generalization error. As a result, another crucial aspect of the ERM technique emerges: given enough learning examples, it finally reveals the best function within $\mathcal{F}$, which has the lowest generalization error. The *consistency* of the ERM principle is the term used most frequently to describe this phenomenon.

Complexity of a class of functions and Overfitting For different classes of functions, the accuracy of the empirical error in estimating the generalization error varies. In contrast to the training examples, it is more common to keep the learned function simple. This is so that a function's simplicity can be determined because it can have a null empirical loss on the training set yet exhibit very high generalization error. *Overfitting* is what this event is known as.

Thus, by limiting the complexity of function class $\mathcal{F}$, the efficacy and homogeneity of the ERM algorithm are maintained. However, it becomes difficult to successfully generalize the learnt function when distribution $\mathcal{F}$ appears to be overly basic in compared to distribution $\mathcal{D}$. Both high empirical error and high generalization error will be present.

Consequently, it is crucial to choose the best function set $\mathcal{F}$. It should achieve acceptable generalization performance without being overly complicated to prevent overfitting or too simple to prevent the problem of *underfitting.* In machine learning, the *bias-variance* trade-off also known as the trade-off between low empirical error and a complicated class of functions is crucial. This idea is demonstrated in Figure 3.9.

Thus, the objective is for the ERM algorithm to acquire the ability to grasp

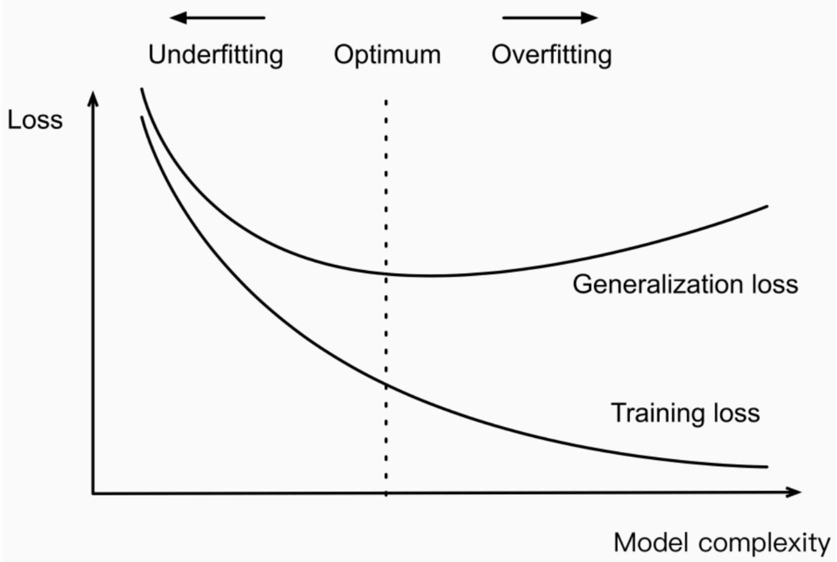

Figure 2.11: The empirical error and generalization error are considered in relation to the complexity of the function class. To discover the ideal class of functions for finding the prediction function, it is crucial to strike a balance between high complexity and low empirical error.

uncomplicated functions. One approach to infuse simplicity (though its precise definition is pending) is to limit the scope of functions within the class $\mathcal{F}$ to those of a straightforward nature. This maneuver leads us to establish a correlation between the ERM principle's concepts of generalization and consistency, showcasing their equivalence. Consequently, by curbing the intricacy inherent in the set of functions $\mathcal{F}$, we secure both the ERM algorithm's generalization and consistency.

Bounds of Generalization Establishing a link between empirical error, generalization error, and the complexity of a specific class of functions is one of the main goals of statistical learning theory. The Rademacher generalization bound [19] (described below), which sets an upper bound on the generalization error, is an example. In proportion to the complexity of the class under consideration, the empirical error, and a residual term that controls the precision of the bound, it has a high likelihood.

Redmacher Complexity Rademacher complexity, denoted as $\mathcal{R}_S(\mathcal{F})$, quantifies the expected difference between the empirical risk and the true risk of a class of functions $\mathcal{F}$ over a sample set S of size m random variables. Mathematically, it can be expressed as:

$$\hat{\mathfrak{F}}_{\mathfrak{m}}(\mathcal{F}, \mathcal{S}) = \mathbb{E}_{\sigma}\left[\sup_{f \in \mathcal{F}} \frac{1}{m} \sum_{i=1}^{n} \sigma_i f(x_i)\right],$$

where: - $\sigma = (\sigma_1, \sigma_2, \ldots, \sigma_m)$ is a vector of independent Rademacher random variables (taking values +1 or -1 with equal probability). - $\mathbb{E}_{\sigma}$ denotes the expectation over all possible realizations of σ. - $f \in \mathcal{F}$ represents a function from the class $\mathcal{F}$. - x_i is the i-th data point in the sample set S.

Increased Rademacher complexity leads to an augmented capacity of function class $\mathcal{F}$ for accommodating random noise. Consequently, the Rademacher complexity is subsequently characterized as follows:

$$\mathfrak{F}_{\mathfrak{m}}(\mathcal{F}) = \mathbb{E}_{S}[\mathfrak{F}_{\mathfrak{m}}(\mathcal{F}, S]. \tag{2.7}$$

In essence, Rademacher complexity measures the "richness" of the class of functions $\mathcal{F}$ in terms of its ability to fit the given data. It provides insights into the potential generalization performance of learning algorithms and is often used in the context of analyzing the complexity of machine learning models for tasks such as binary classification.

Theorem 1 (Generalization bound [19]). *Let $\mathcal{X} \in \mathbb{R}$ be a vectorial space and $\mathcal{Y} = \{-1, +1\}$ an output space. Suppose that the pairs of examples $(x, y) \in \mathcal{X} \times \mathcal{Y}$ are generated i.i.d. with respect to the probability distribution $\mathcal{D}$. Let $\mathcal{F}$ be a class of functions having values in $\mathcal{Y}$ and $\ell : \mathcal{Y} \times \mathcal{Y} \to [0, 1]$ a given loss and m is number of random variables. Then for all $\delta \in [0, 1]$, we have with probability greater or equal to $1 - \delta$ the following inequality:*

$$\forall f \in \mathcal{F}, \mathcal{L}(f) \leq \hat{\mathcal{L}}_m + (f, S) + \mathfrak{F}_{\mathfrak{m}}(\ell \circ \mathcal{F}) + \sqrt{\frac{\ln \frac{1}{\delta}}{2m}} \tag{2.8}$$

Similarly utilizing the same process it can be also shown that with probability at least $1 - \delta$:

$$\mathcal{L}(f) \leq \hat{\mathcal{L}}_m(f, S) + \hat{\mathfrak{F}}_{\mathfrak{m}}(\ell \circ (f, S)) + 3\sqrt{\frac{\ln \frac{2}{\delta}}{2m}} \tag{2.9}$$

Where, $\ell \circ \mathfrak{F} = \{(x, y) \mapsto \ell(f(x), y) | f \in \mathcal{F}\}$. The three components on the right side of the inequalities (2.8) or (2.9) must have low magnitudes in order to reduce risk. These elements are composed up to two components: the empirical error, which depends on the prediction function f, and the second term, which is affected by the function class $\mathcal{F}$'s complexity. It becomes essential to choose a function class that is not overly complex while simultaneously minimizing the empirical error (which has a larger complexity term) in order to ensure a theoretical guarantee of generalization error. Establishing a balance is essential to avoid major empirical errors caused by oversimplifying data. As a result of these factors, the notion of bias-variance trade-off is developed.

Neural Networks Neural networks, without a doubt, emerge as one of the preeminent classification algorithms in the realm of Machine Learning. In the forthcoming segment, our contributions will be expounded upon, wherein these models find utilization.

A neural network comprises artificial neurons, interconnected to enable diverse non-linear transformations. These models originated from the endeavors of neuroscientists in the 1950s, who delved into mathematical models to conceptualize the workings of natural neurons. These models enjoyed some success until the 1990s when the field of machine learning encountered a revolutionary shift with the advent of statistical learning theory, proposed by [173]. Throughout this era, little progress was made in the practical application and utilization of neural networks. However, recent advancements in hardware components, particularly the emergence of new graphics processors (GPU - Graphics Processing Unit) and increased RAM capacity, have reignited enthusiasm in learning with neural networks. These developments have facilitated Intricately constructed multilayer neural networks were first shown with the advent of deep learning, which was a major turning point. Their application in essential fields of computer science like computer vision and automated natural language processing has advanced dramatically since 2010. The objective of this chapter is to present the fundamental principles underlying the learning process of these networks.

In this part, let us delve into an exceptionally broad modular framework. Within this structure, a network manifests a sequential amalgamation of functions, with each function denoting a layer and characterized by its unique set of parameters.

In our analysis, we focus on the simple sequential scenario. Here, the model computes the function h_W or $h(W)$, which represents the overall transformation executed by the network. This transformation is achieved by combining N functions, denoted as $h_n(W_n)$, where each function corresponds to a specific step in the sequential process, ranging from 1 to N i.e. $1 \leq \ n \leq N$:

$$h_W = h^N_{W_N} \circ ... \circ h^2{}_{W_2} \circ h^1{}_{W_1} \tag{2.10}$$

In this explanation, $h_W(x)$ represents the model's prediction for a given input x. The composite function is defined by the vector W, which consists of the concatenated vectors W_n, where $1 \leq n \leq N$. The functions h^n may have varying dependencies on their parameter vectors W_n, and these vectors can have different sizes. While the vectors W_n can potentially contain more complex structures like matrices or weight tensors, in the context discussed here, they will only be treated as vectors with serialized contents. The functions h_n can be arbitrary as long as they are both differentiable with respect to their data and parameters.

The use of a function often indicates a formal neuron layer in the traditional representation of neural networks. However, in real-world applications, the conventional idea of a neuron layer is typically implemented by two subsequent functions, each of which corresponds to a different kind of layer (or sub-layer). The first is referred to as a *linear layer*, and it consists solely of multiplying a matrix by a vector for the linear component. The second layer, also known as a *point-to-point layer*, is in charge of applying the activation function for the non-linear aspect element by element. On occasion, other operations like regularization or normalization may also be included.

A very adaptable back-propagation technique for training networks of this type is described below. Different combinations of differentiable and parameterizable functions can be used with it. In this discussion, we will pay particular attention to the sequential combination of functions. It's crucial to remember that the method's generality goes deeper. It can be applied to functional combinations that are organized in any acyclic graph.

Optimizers - Stochastic Gradient Descent Frequently, when aiming to train a network defined by a global function h_W relying on parameter vector W, a commonly employed approach involves utilizing mini-batches and stochastic gradient descent. The goal is to minimize an objective function, which is regulated, while staying true to the Structural risk minimization (SRM) [173] principle. For this purpose, a training set $\mathcal{S} = (xi, yi)_{1 \leq i \leq m}$ is utilized.

$$\hat{\mathcal{L}_m}(h_W, \mathcal{S}) = \frac{1}{m} \sum_{(x,y) \in \mathcal{S}} \ell(h_W(x), y) + \lambda \Omega(W) \tag{2.11}$$

A regularization term designated as $\Omega(W)$ is added to prevent overfitting, assuming the loss function ℓ is continuously differentiable. The parameter λ is used to determine the relative impact of the regularization term and function Ω must be continuously differentiable.

A mini-lot, which is a subset of the training set $\mathcal{M}_S \subseteq \mathcal{S}$, is used in the stochastic mini-batch version of the gradient descent algorithm's formula (2.12) for updating the vector W.

$$W^{(t+1)} = W^{(t)} - \frac{\eta}{|\mathcal{M}_\mathcal{S}|} \sum_{(x,y)\in\mathcal{M}_\mathcal{S}} \nabla_W \mathcal{L}_{(x,y)}(W^{(t)}) \tag{2.12}$$

with :

$$\mathcal{L}_{(x,y)}(W) = \ell(h_w(x), y) + \lambda\Omega(W) \tag{2.13}$$

So, the square loss and $\Omega(.)$ the squared norm of the weights could be the regularisation term, i.e. :

$$\mathcal{L}_{(x,y)}(W) = \frac{1}{2}(h_W(x) - y)^2 + \frac{\lambda}{2}||W||^2 \tag{2.14}$$

The computation of $\nabla_W \ell(h_w(x), y)$ for the (x, y) example becomes necessary in order to use the gradient descent approach described in eq. (2.12) and (2.13). It should be noted that when Eq. (2.12) and (2.13) are employed, calculating $\nabla_W \Omega(W)$ is typically simpler. For instance, $\nabla_W \Omega(W)$ would be W^T when $\Omega(W) = \frac{1}{2}||W||^2$. This regularization, which is also known as *weight decay* in the literature, can be thought of as applying a decay rate $\eta\lambda$ to the components of W during each iteration t.

The concatenation of vectors W_n, where $1 \leq n \leq N$, yields to W. As for the concatenation of $\nabla_{W_n} \ell(x^n, y)$, denoted as $\nabla_W \ell(x, y)$, it can be simplified by introducing a simplified notation $\frac{\delta\ell}{\delta W_n}$.

Gradient Computation The gradient $\nabla\ell(x, y)$ are computed by *backpropagation* algorithm. The term '*backpropagation*' was first introduced by Frank Rosenblatt in 1962 [155], but implementation was not known. In 1986, David Everett Rumelhart and Geoffrey Hinton, American psychologists published the first experimental analysis of the technique [157].

- The initial stage of prediction for training, which is referred to as the *forward pass*, embodies the normal network behavior. Through the sequential application of the $h^n_{W_n}$ functions, the values of x^n are repeatedly calculated from the current input, $x^0 = x$, during this process. Additionally, the associated cost or error is computed as $\ell(x^n, y)$.
- As part of the *backward pass*, the second phase involves executing *backpropagation* with respect to the data. Within this segment of the backward pass, we iteratively compute the gradients for the data x^n based on the error, starting from N and decreasing with each iteration. This computation is performed using the chain rule in Eq. (2.15) and (2.16) :

$$\delta_N = \frac{\delta\ell(x^N, y)}{\delta x^N} \tag{2.15}$$

$$\forall_n \in \{N, ..., 2\}; \delta_{n-1} = \frac{\delta\ell(x^N, y)}{\delta x^{n-1}} = \frac{\delta\ell(x^N, y)}{\delta x^n} . \frac{\delta h^n_{W_j(x^{n-1})}}{\delta x^{n-1}} \tag{2.16}$$

  From the definition, $x^n = h^n_{W_n}(x^{n-1})$
- Part three, known as *parameter-based backpropagation*, is a component of the backward pass. It does not involve any recurrence relation and is independent of both forward and backward dependencies on the values of n when $\frac{\delta\ell(x^N,y)}{\delta x^N}$ is computed in the second part. By employing the chain rule once more, the gradients of the error with respect to the parameters W_n are finally computed.

$$\forall_n \in \{N, ..., 1\}; \frac{\delta\ell(x^N, y)}{\delta W_n} = \frac{\delta\ell(x^N, y)}{\delta x_n} . \frac{\delta h^n_{W_n(x^{n-1})}}{\delta W_n} = \delta_n \frac{\delta h^n_{W_n(x^{n-1})}}{\delta W_n} \tag{2.17}$$

Applying Neural Networks for the Reconstruction of EMF Exposure Maps Neural networks have recently been employed in the reconstruction of exposure maps. Various studies have focused on estimating signal values by utilizing known locations and incorporating additional information [103, 69, 127, 80, 201]. Side information commonly used includes radio parameters (such as transmission specifications or the Rx-Tx connection) and building details (such as height) [103]. In cases where building information is unavailable, researchers resort to satellite photos for forecasting (as demonstrated in the paper [80]). The approach in these works treats the problem as a regression task, employing environmental or technological characteristics as input and predicting the signal value as output.

The majority of these efforts adopted NN models that were created for image classification and segmentation and treated the signal map as an image.

Image processing by Neural Network models Convolutional neurons are used in neural network models for image analysis to extract high-level information from natural images. In contrast to the feedforward neural networks covered in Section 3.2.2, these models exhibit a distinctive characteristic. Formal neurons in each layer are connected to all formal neurons in the layer before them (or to all of the inputs for the top layer). The all-to-all connection scheme, which describes this fully connected configuration, calls for independent weights and biases for each connection and each neuron. Although the input and output values are often represented as vectors of real numbers, the organization of neurons within the layers lacks a precise topology; they instead form a collection rather than a vector, matrix, or any other hierarchical arrangement.

The input data for image analysis is set up in a particular way—a two-dimensional grid. Preserving and using this structure becomes important for maximizing parameter utilization and computational power, particularly in the earliest layers of neural networks. This is accomplished by setting a maximum distance restriction on connections depending on the grid and by distributing weight across units in the same layer but at different grid locations. Therefore, matrix-vector product operations are not used, but rather convolution operations, which have limited support and translation invariance. However, both strategies are really combined in practice. Consequently, a collection of identical neurons are related from one place to another rather than one neuron being assigned to each grid position.

The input and output layers will both have D topological dimensions if the input data is organized in accordance with a grid of D dimensions ($D = 2$ in the case of an image signal). There will also be an additional non-topological dimension to take into account the fact that each grid point in the data can take several values. These values, which are scattered evenly throughout the grid like arrays, serve as tables with values for each point on the grid. For each level of data processing, a different number of these arrays is chosen.

Images are represented as tensors of order 3, denoted as X_{in} and X_{out}. X_{in} has a size of $p_{in} \times w_{in} \times h_{in}$, while X_{out} has a size of $p_{out} \times w_{out} \times h_{out}$. Here, p_{in} and p_{out} represent the number of matrices in X_{in} and X_{out}, respectively. The dimensions $w_{in} \times h_{in}$ and $w_{out} \times h_{out}$ correspond to the grid sizes on which X_{in} and X_{out} are defined. The convolution layer's linear component can be described as follows eq.

(2.18):

$$X_{out}(l,i,j) = B(l) + \sum_{k-p_in}^{k=1} \sum_{m=+w}^{m=-w} \sum_{n=+w}^{n=-w} \kappa(l,k,m,n) X_{in}(k, i-m, j-n) \tag{2.18}$$

For $1 \leq i \leq w_{out}$, $1 \leq j \leq h_{out}$ and $1 \leq l \leq p_{out}$; where w is the maximum distance in the grid at which points can be connected.

The varied selection of p_in cards in X_{in} serves as the independent and autonomous base of values for the p_{out} cards of X_{out}. One of the output maps is computed using a convolution filter, which appears to be the key player in the world of input maps. A scalar $B(l)$ and a three-dimensional tensor known as the kernel of this filter, denoted by the expression $\kappa(l,.,.,.)$, describe the identity of each of these filters, referred to as p_{out} filters. This kernel's dimensions coincide with our consensus that the filter size is $(2w+1) \times (2w+1)$ and span $d_{in} \times (2w+1)(2w+1)$. As a result, the robust kernel and the harmonious combination of vector B and materialize the entire convolution layer.

The **UNet model** is a deep learning architecture widely used for image segmentation tasks, first presented in [151]. This architecture is based on encoder-decoder neural networks, which are fundamental in nature. In this method, the encoder component concentrates on locating key patterns in the input data before transferring important information to the decoder component. Max pooling and convolutional layers make up the encoder part. Deconvolution, also known as the symmetric expanding path, is carried out in the background by the decoder component in order to upsample the image back to its original input size using the recovered data. Figure 2.12 shows an illustration of the U-Net-based design, which incorporates skip connections for image reconstruction.

Generative Adversarial Networks GANs, a novel method, are widely used in image analysis. This model is based on convolutional neural networks, namely, the generator and the discriminator models included in a game-like scenario in GAN. The Generator's goal is to generate observations that the Discriminator will verify. To learn the distribution p_G, which closely reflects the true distribution p_{data} of the input dataset, is done by the generator. The network works by taking a genuine observation and an input noise vector z from a previous distribution $p(z)$, producing an output $G(z)$, and then passing it to the discriminator. In the end, the Discriminator calculates the likelihood that the input sample came from the Generator's output as opposed to the training set.

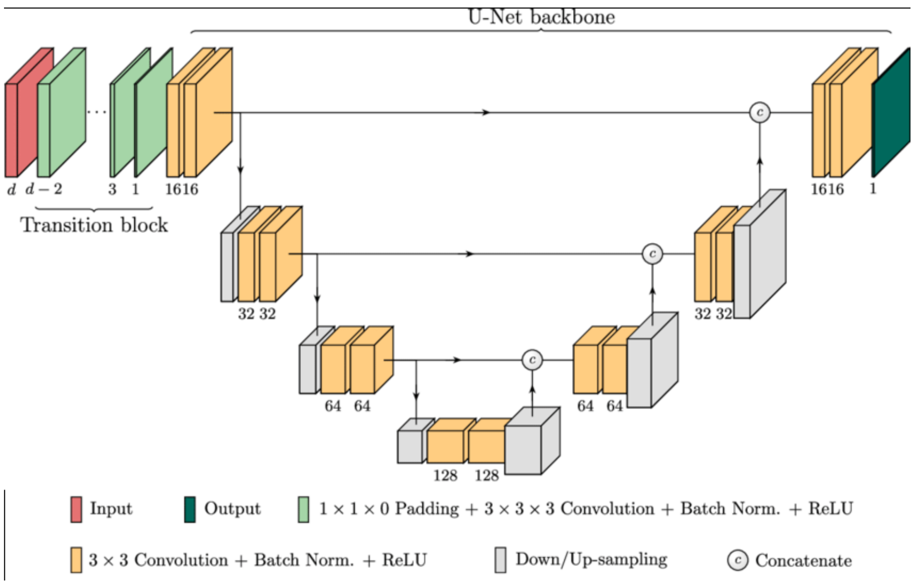

Figure 2.12: UNet-based architecture, padding is not compulsory

The Generator and Discriminator networks are trained concurrently, engaging in a two-player minimax game. In this game, the Generator's parameters θ_G are adjusted to confuse the Discriminator, effectively reducing $log(1 - D(G(z)))$. Conversely, the Discriminator's parameters θ_D are fine-tuned to achieve optimal classification predictions, maximizing $\log D(x) + \log(1 - D(G(z)))$. The objective function for this minimax game can be described as follows eq. (2.19):

$$\min_{\theta_G}\max_{\theta_D}(\mathbb{E}_{x\sim p_{data}(x)}(\log(D(x)) + (\mathbb{E}_{x\sim p_z(z)}(\log(1 - D(G(z))))) \tag{2.19}$$

The training procedure of this adversarial network is conducted with simultaneous update of both θ_D and θ_G by stochastic gradient descent of logistic loss functions in eq. (2.20) and (2.21):

$$\nabla_{\theta_D}\frac{1}{2}\frac{1}{n}\sum_{n}^{i=1}(\log(1 - D(x^i)) + \log(D(G(z^i))), \tag{2.20}$$

$$\nabla_{\theta_G}\frac{1}{n}\sum_{n}^{i=1}(\log(1 - D(G(z^i)))), \tag{2.21}$$

where n is the size of the data batch during the training process.

This GAN model could be further extended to the conditional case (namely cGAN), where additional information could be added as an input to both the generator and the discriminator in order to help the generator produce outputs that are more similar to the data or the discriminator better distinguish between true and fake samples. We may rewrite the objective function from Eq. (2.22) as follows by denoting this new knowledge as a condition:

$$L_{cGAN}(G, D) = E_{x,y}[\log D(x, y)] + E_{x,z}[1 - \log D(x, G(x, z)] \tag{2.22}$$

where x is the input, y is the output, and z is the conditional signal. The generator G is not only trying to reduce the loss from the discriminator but also trying to move the fake distribution close to the real distribution by using L1 loss given by:

$$L_{L1}(G) = E_{x,y,z}[\|y - G(x, z)\|]. \tag{2.23}$$

The loss function of the generator network is stated in Eq. (2.24):

$$G^{\star} = \arg\min_{G}\max_{D} L_{cGAN}(G, D) + \lambda L1(G). \tag{2.24}$$

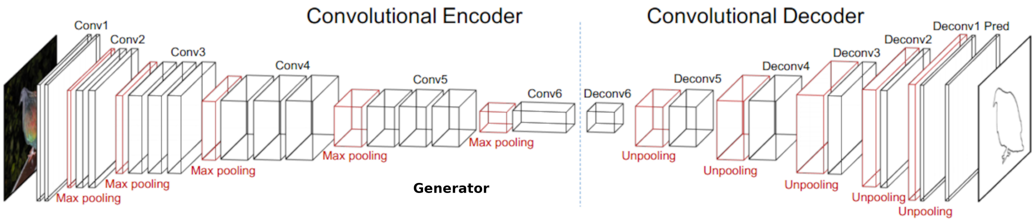

Figure 2.13: Example of Generator architecture

Figure 2.13 illustrates an example of the architectures of the Generator (top), with the goal of producing samples that are indistinguishable from real data. The Discriminator (bottom), with the target of estimating the probability that the samples come from the real distribution rather than was produced by the Generator.

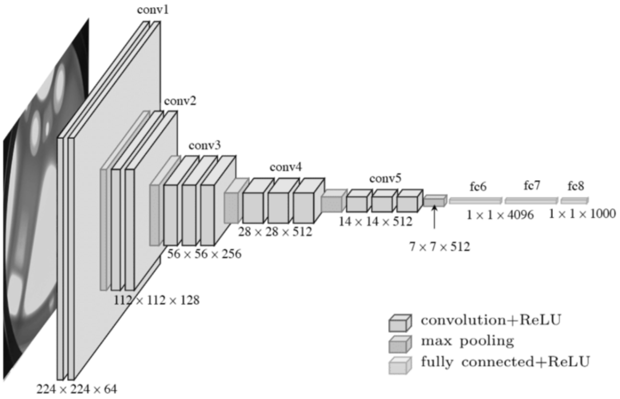

Figure 2.14: Example of Discriminator Architecture

2.2.1.2 Semi-Supervised Learning

Manually constituting coherent and consistent labeled collections is a laborious process that demands significant effort and often proves time-consuming and, in certain scenarios, unfeasible. Since the late 1990s, the ML community has been exploring semi-supervised learning for discrimination and modeling tasks. This exploration stems from the realization that labeled data is costly, while unlabeled data is abundant and harbors valuable information pertinent to the problem at hand.

Definitions: In this context, the scarcity of labeled examples typically hinders the attainment of reliable estimation of the desired association between the input and output spaces. Consequently, the objective becomes utilizing unlabeled examples to achieve a more accurate estimate. Given a set of labeled training examples $S = (x_i, y_i)|i = 1, ..., m$, which are assumed to be generated independently and identically distributed (i.i.d.) from an underlying distribution $\mathcal{D}$, and a set of unlabeled examples $X_u = (x_i|i = m+1, ..., m+u)$, which are drawn independently and identically distributed from the marginal distribution $\mathbb{P}(x)$. Similar to this, if S is empty, we run into an unsupervised learning problem.

Semi-supervised algorithms are used to estimate labels for unlabeled samples throughout the learning process. These algorithms estimate a pseudo-label $\widetilde{y}$ for an unlabeled sample $x \in X_u$, which is represented by the symbol y. When $u = |X_u| \gg m = |S|$, semi-supervised learning becomes significant since the goal is to use the knowledge about the marginal distribution, $P(x)$, learned from the unlabeled samples to acquire useful information for inferring $P(y|x)$. In the event that this goal is not accomplished, the efficiency of semi-supervised learning will be diminished compared to supervised learning, and there is even a possibility that the performance of the learned prediction function will be degraded by the utilization of unlabeled data [200, 39]. Consequently, the formulation of working hypotheses is deemed necessary for the incorporation of unlabeled data into the supervised learning process of a prediction function.

Inductive vs Transductive Learning We emphasize that semi-supervised learning can be defined in two different contexts, namely transductive and inductive learning, In the inductive case (covered in previous sections), where the learning objective is to minimize the genealization risk for the distribution D. This scenario involved training a model across a limited number of training samples. The most typical semi-supervised learning environment is also this one.

Kernel Methods are a class of machine learning algorithms that utilize kernel functions to implicitly map data into a higher-dimensional feature space. These methods excel at handling nonlinear relationships and are widely used for tasks such as classification, regression, and dimensionality reduction. In kernel methods, the key idea is to operate solely on inner products between data points in the transformed feature space, avoiding the explicit computation of high-dimensional feature vectors. This approach is mathematically elegant and computationally efficient.

An essential component of kernel methods is the kernel function, denoted as $K(x, x')$, which computes the inner product between the two input samples, x and

x', in the feature space. This can be expressed as:

$$K(x, x') =< \phi(x).\phi(x') >, \tag{2.25}$$

where $\phi(x)$ and $\phi(x')$ are the respective feature vectors in the transformed space. By using kernel functions, we can work with the kernel matrix K, which stores all pairwise inner products between the data points, instead of explicitly calculating and storing the transformed feature vectors.

Kernel methods rely on the concept of a positive definite kernel function, denoted as $K(x, x')$, which calculates the similarity between two data points x and x' in the input space. The most commonly used kernel is the Gaussian also known as radial basis function (RBF) kernel, defined as :

$$K(x, x') = exp(-\gamma||x - x'||^2), \tag{2.26}$$

where γ is a parameter that controls the smoothness of the kernel.

One of the fundamental properties of kernel methods is **Mercer's theorem** [123], which guarantees that a function can be expressed as a kernel if and only if its corresponding kernel matrix is positive semidefinite. By using the kernel trick, the kernel function is implicitly applied to the input space, enabling efficient computations even in high-dimensional or infinite-dimensional feature spaces. Kernel methods offer a non-linear way to transform the input space, allowing linear algorithms to work effectively on non-linear problems.

The kernel matrix is a symmetric matrix where each element $K_{\{i,j\}}$ represents the similarity between input samples i and j. It serves as the basis for various kernel-based algorithms. Support Vector Machines (SVMs) are a well-known example of kernel methods that use the kernel trick to find a hyperplane that separates data points in a transformed feature space. The kernelized version of SVMs solves a dual optimization problem, involving only the inner products of input samples, making it computationally efficient. Kernel Principal Component Analysis (PCA) utilizes the kernel trick to capture non-linear dependencies in data, projecting it onto a lower-dimensional space while preserving its essential structure. Kernel Ridge Regression [176, 182] is another application of kernel methods that combines ridge regression with the kernel trick to perform non-linear regression tasks. The kernel trick allows the use of linear algorithms, such as ridge regression, perceptron, or logistic regression, on data transformed by a kernel function. Representer Theorem [93] is a fundamental result in kernel methods that states that the optimal solution of many kernel-based learning algorithms can be expressed as a linear combination of kernel evaluations on the training data. In addition to classification and regression, kernel methods have found applications in anomaly detection, clustering, and time series analysis. The choice of an appropriate kernel function is crucial for the success of kernel methods. Different kernels have different characteristics and are suitable for capturing different types of data structures. Kernel methods offer several advantages, including flexibility in modeling complex relationships, implicit feature expansion, and the ability to incorporate prior knowledge through the choice of the kernel function. Additionally, they exhibit strong mathematical foundations, such as the representer theorem and Mercer's theorem, which guarantee the validity of kernel functions and provide insights into the behavior of these methods.

Kernel Regression A non-parametric statistical method called kernel regression is used to calculate the conditional expectation of a random variable given a set of observed data. Without taking a precise functional form, it is frequently used for finding trends in the data and smoothing noisy data.

Kernel regression's fundamental notion is to give neighboring data points weights based on how close they are to a particular point of interest. A kernel function, which is a symmetric, non-negative function that integrates to 1, is commonly used to assess this proximity.

At a high-level overview of how kernel regression works:

Kernel Function Selection: Choose a suitable kernel function, such as the Gaussian kernel, Epanechnikov kernel, polynomial kernel, or others. The choice of kernel can affect the smoothness and sensitivity of the regression.

Bandwidth Selection: Determine the bandwidth parameter, which controls the size of the neighborhood around each point that contributes to the regression. A larger bandwidth includes more data points, while a smaller bandwidth considers only closer points.

Weight Calculation: For each point in the dataset, calculate the weights for nearby points based on the chosen kernel and bandwidth. Points closer to the target point receive higher weights.

Regression Estimation: Calculate the estimated value at the target point by combining the weighted contributions of the neighboring data points.

Mathematically, the estimated value at a given point x using kernel regression is expressed as:

$$f(x) = \frac{1}{n} \sum_{i=1}^{n} \frac{K(\frac{x-x_i}{h}) y_i}{\sum_{i=1}^{n} K(\frac{x-x_i}{h})} \tag{2.27}$$

where, n is the total number of data points, x_i are the data points, y_i are the corresponding observed values, K is the chosen kernel function, h is the bandwidth.

In the context of a training dataset denoted as $\{(x_p, y_p)\}_{p=1}^{n}$ where $x_p \in \mathbb{R}^d$ and $y_p \in \mathbb{R}^c$, the concept of kernel regression involves following process [176, 182, 47, 141]. Initially, each x_p is subjected to a predetermined feature mapping ψ, which transforms it from $\mathbb{R}$ to a Hilbert space denoted as $\mathcal{H}$. Subsequently, a linear regression analysis is conducted on the transformed dataset $\{(\psi(x_p), y_p)\}_{p=1}^{n} \in \mathcal{H} \times \mathbb{R}^c$. The challenge arises when $\mathcal{H}$ has an infinite dimensionality; in this case, solving linear regression depends on grasping the inner product relationships among the transformed data points. Specifically, these inner products, denoted as $\langle \psi(x), \psi(z) \rangle_{\mathcal{H}}$ for $x, z \in \mathbb{R}^d$, play a crucial role. The inner products are abstracted which is a positive semi-definite and symmetric function $K : \mathbb{R}^d \times \mathbb{R}^d \to \mathbb{R}$, known as the kernel K. Given the aforementioned training dataset and a kernel function denoted as K, the process of kernel regression is first, the kernel matrix, denoted as $\hat{K}$, where $\hat{K}$ is an $n \times n$ matrix with entries $\hat{K}_{i,j} = K(x_i, x_j)$. then Solve the system of equations $\beta \hat{K} = y$, where β is a vector in the space $\mathbb{R}^{c \times n}$, and $y = [y_1, ..., y_p]$ is a vector in the space $\mathbb{R}^{c \times n}$. The resultant predictor, represented as $\hat{f} : \mathbb{R}^d \to \mathbb{R}^c$, is defined as follows: $\hat{f}(z) = \beta K(X, z)$, where $K(X, z)$ is a vector in the space $\mathbb{R}^n$ with entries $K(X, z)i = K(x_i, z)$.

Notably different from the case of neural networks, it is important to highlight that training a kernel machine involves addressing a convex optimization problem, which corresponds to solving a linear system of equations. Kernel regression is widely used in various fields, including finance, economics, machine learning, and signal processing, for tasks like smoothing data, time series prediction, and density estimation. It is a powerful tool for understanding relationships in data when the underlying structure is unknown or complex.

2.2.2 Modern Machine Learning

Modern ML has witnessed intriguing phenomena that challenge conventional wisdom regarding model complexity and generalization. One particularly fascinating aspect is the phenomenon of double descent [21, 121] in infinite-width neural networks. Traditionally, as model complexity increases, the risk of overfitting grows, leading to poor generalization. However, recent research has shown that for certain tasks and datasets, the performance of deep neural networks improves with increasing width, even surpassing the performance of narrower networks. This phenomenon occurs due to the network's ability to capture intricate data patterns and interpolate them more accurately as the width increases. Double descent in infinite-width neural networks highlights the delicate balance between capacity and regularization in learning (see Figure 2.15).

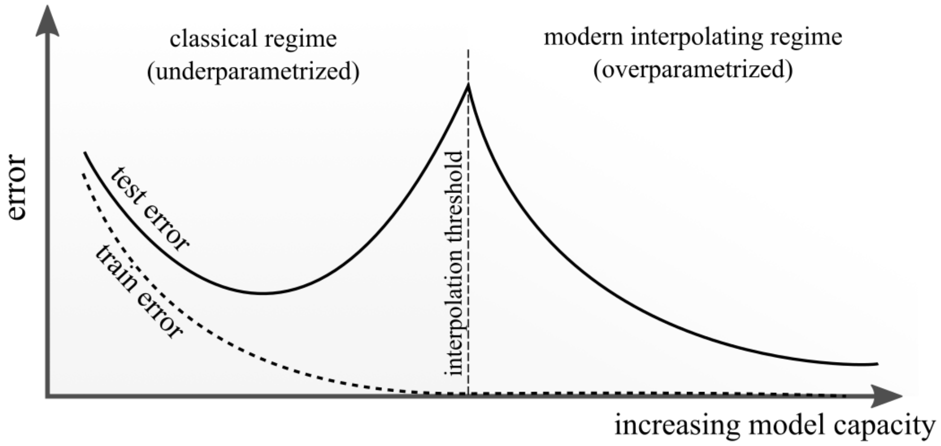

Figure 2.15: This figure depicts a schematic representation of the empirically observed double descent phenomenon. Specifically, within the under-parameterized (classical) realm, traditional overfitting becomes apparent: data interpolation is unachievable, resulting in an increase in test loss alongside the reduction of training loss. Conversely, in the over-parameterized (modern) scenario, all models impeccably capture the training data, leading to a noteworthy decline in test loss as the model's complexity, characterized by neural network width in this context, expands.

Double descent & Overparameterized Networks The phenomenon of double descent in modern machine learning, specifically in infinite-width neural networks under overparameterization [21], can be mathematically described. Let us consider a deep neural network with a fixed architecture and an activation function, represented by $f(x;\theta)$, where x denotes the input and θ represents the network parameters. The network is trained using a dataset $\{(x_i, y_i)\}_{i=1}^{N}$, where y_i is the corresponding target output. The network's training error can be quantified by the empirical risk, $R(\theta) = \frac{1}{N}\sum_{i=1}^{N} L(y_i, f(x_i;\theta))$, where L is a loss function measuring the discrepancy between the predicted and true outputs.

In the case of overparameterized neural networks, where the number of parameters greatly exceeds the number of training data points, the optimization problem becomes highly nonlinear and complex. The key observation is that as the network width approaches infinity, the optimization landscape undergoes a phase transition. This transition is characterized by a U-shaped curve in the generalization error, $G(\theta) = \mathbb{E}_{x,y}[L(y, f(x;\theta))]$, as a function of model complexity. The generalization error initially decreases with increasing model complexity until it reaches a minimum, followed by an increase known as the double descent curve. This behavior is mathematically captured by the equation $G(\theta) = R(\theta) + \lambda\Omega(\theta)$, where $\Omega(\theta)$ represents a regularization term and λ controls the trade-off between training error and complexity.

The interplay between overparameterization, width, and double descent can be further explored using statistical learning theory. The Rademacher complexity, $R_n(\mathcal{F})$, provides a measure of the complexity of a function class $\mathcal{F}$ with respect to a given sample size n. It quantifies the ability of the class to fit random noise in the training data. In the case of overparameterized networks, the Rademacher complexity exhibits a logarithmic dependence on the network width, emphasizing the importance of width in capturing finer data structures. The explicit formulation of the Rademacher complexity and its relation to network width and generalization error offer valuable insights into the theoretical foundations of double descent in the context of overparameterized infinite-width neural networks.

2.2.2.1 Linearization of Neural Network

Consider a set of training samples denoted as $X = [x(1), x(2), ..., x(n)] \in R^{d\times n}$, along with their corresponding training labels $y = [y(1), y(2), ..., y(n)] \in R^{1\times n}$. Instead of utilizing linear or kernel regression methods to fit this training data, we can opt for a neural network that implements a function $f(x) : R^d \to R$.

In the scenario where the neural network consists of a single hidden layer, it is conventionally parameterized by two weight matrices $A \in R^{1\times k}$ and $B \in R^{k\times d}$. Additionally, it employs an elementwise nonlinearity function $\psi : R \to R$ to enhance its capabilities.

Definition 1 (Linearization of Neural Network) . *Let* $f_x(w) : \mathbb{R}^P \to \mathbb{R}$ *denote a neural network operating on a fixed sample* $x \in R^d$*. Then, the linearization of* $f_x(w)$ *around initial weights* $w(0)$ *is given by:*

$$\widetilde{f_x}(w) = f(w^{(0)}) + \nabla f_x(w^{(0)})^T(w - w^{(0)}) \tag{2.28}$$

It is important to emphasize that the linearization mentioned earlier can be viewed as the application of a linear model to modified characteristics. To train the linearization $\widetilde{f_x}(w)$ using the Mean Squared Error (MSE) loss, we solve a linear regression problem by first applying the feature map $\psi : \mathbb{R}^d \to \mathbb{R}^p$, where $\psi(x) = \nabla f_x(w(0))$, to the samples. Thus, linear regression can be efficiently tackled using the kernel trick. The kernel mentioned below is commonly known as the Neural Tangent Kernel (NTK) [83].

2.2.2.2 Infinite Width Neural Networks

It is a theoretical construction that connects neural networks to kernel methods, enabling us to understand the behavior of neural networks in the context of kernel-based algorithms. In this framework, an infinite width network is approximated by its associated kernel, allowing us to leverage the tools and insights from kernel methods.

An infinite width neural network is characterized by an infinite number of neurons in each layer, resulting in an unbounded number of parameters. The activation of each neuron is determined by a weighted sum of its inputs, followed by an activation function, such as the rectified linear unit (ReLU). The output of a neuron can be represented as $y = f(Wx+b)$, where $\mathcal{Y}$ is the neuron's output, $\mathcal{X}$ is the input vector, W is the weight matrix, b is the bias vector, and $f(\psi)$ is the activation function. In an infinite width network, the weight and bias parameters are typically assumed to be drawn from a gaussian distribution.

For example, considering a simple regression task, where we aim to approximate a function $f(x)$ using an infinite width neural network, the NTK can be defined as:

$$K(x, x') = Cov(\nabla\theta f(x), \nabla\theta f(x')), \tag{2.29}$$

where x and x' are input samples, $f(x)$ represents the output of the network for input x, $\nabla\theta f(x)$ denotes the gradient of $f(x)$ with respect to the network's weights θ, and $Cov(.)$ denotes the covariance.

2.2.2.3 Neural Tangent Kernel: NTK

NTK [83] is a mathematical tool that connects the infinite-width neural network and kernel methods. It allows us to analyze the behavior and properties of neural networks in the limit of infinitely many neurons per layer. In this detailed explanation, we will delve into the NTK and its connection to infinite-width neural networks, discussing the mathematical foundations, key concepts, and practical implications.

Definition 2 (Neural Tangent Kernel) *Let* $f(w) : \mathbb{R}^P \to \mathbb{R}$ *denote a neural network with initial parameters* $w^{(0)}$*. The* ***neural tangent kernel,*** $K : \mathbb{R} \times \mathbb{R} \to \mathbb{R}$ *is a positive semi-definite function given by:*

$$K(x, x') = \langle \nabla f_x(w^{(0)}), \nabla f_{x'}(w^{(0)}) \rangle, \tag{2.30}$$

where $w^{(0)} \in \mathbb{R}^P$ *denotes the parameters at initialization.*

The NTK captures the similarity or covariance between gradients of the outputs of an infinite width neural network with respect to its weights. In an infinite width network, the weights and biases are typically assumed to be randomly drawn. The NTK measures how small perturbations in the weights affect the network's output. The NTK is a symmetric positive semidefinite kernel matrix, denoted as $K(x, x')$, where x and x' are input samples. The entries of the NTK matrix, K_{ij}, are given by the covariance between the gradients of the network's outputs for inputs x_i and x_j with respect to the weights. The NTK is closely related to the kernel methods, as it measures the similarity between inputs in a high-dimensional feature space implicitly defined by the neural network. Using the NTK, the network's output for a given input x can be expressed as:

$$f(x) = \sum_i \alpha_i K(x, x_i), \tag{2.31}$$

where α_i represents the learned coefficients. The main discovery in [83] indicates that when w_i are independently and identically distributed (i.i.d.) with a standard normal distribution (0, 1), as the indices $k_1, k_2, ..., k_L$ approach ∞, the kernel $K(x, x')$ converges with a high likelihood to a fixed kernel that remains constant throughout the training process. The NTK can be computed using automatic differentiation techniques, which allow efficient calculation of the gradients required for the covariance estimation. In the case of feedforward neural networks with ReLU activations, the NTK has been shown to converge to a limiting kernel during training. The limiting kernel is a piecewise linear function and can be computed analytically for specific network architectures. The limiting NTK provides insights into the network's behavior, training dynamics, and generalization properties. One important property of the NTK is the neural tangency property, which states that the NTK remains fixed during training when the network is initialized with small random weights. This property allows for the analysis of network behavior without explicitly considering the weight updates during training.

The NTK also exhibits interesting properties such as kernelized memorization, where the network learns to store training data in its weights. Additionally, the NTK connects to random features and random networks, providing links to the theory of random matrix theory and random feature expansions. While the NTK framework provides valuable theoretical insights, it is important to note that it assumes an infinite width limit, which may not be directly applicable to finite width networks commonly used in practice.

Nonetheless, the NTK analysis serves as a valuable tool for understanding the behavior and properties of neural networks and can guide the design and optimization of practical architectures.

Similarity of training Neural Network and NTK: The correspondence of the NTK with the training of neural networks has been described. The NTK emerges as the kernel linked to the linearization of an initial weight configuration in a neural network. Interestingly, when the widths of individual layers tend towards infinity, solving kernel regression using the NTK remarkably converges to the process of training all the layers in a neural network, as proved in [106, 105].

2.2.2.4 Convolutional Neural Tangent Kernel: CNTK

Convolutional Neural Networks (CNNs) have revolutionized many areas of machine learning, particularly in computer vision tasks. A significant theoretical development in understanding CNNs is the introduction of CNTK [12]. CNTKs provide a mathematical framework for analyzing the behavior and generalization properties of CNNs. We present an overview of the CNTKs, their mathematical formulation, and their application in deep learning. CNTK [12] is derived from the NTK theory, which extends the kernel theory to convolutional neural networks. CNTKs provide a way to analyze the dynamics of CNNs during training and their generalization capabilities similar to NTK. The CNTKs capture the similarity between inputs by measuring the inner product between the tangent vectors of neural network parameters. This similarity measure facilitates the study of gradient-based optimization and generalization in CNNs. CNTK is defined by :

$$K(x, x') = \langle \frac{\delta f(x)}{\delta W_{i,j,k,l}} \times \frac{\delta f(x')}{\delta W_{i,j,k,l}} \rangle, \tag{2.32}$$

where x and x' are input examples, $W_{i,j,k,l}$ represents the weights of the convolutional filters, $\sum_{i,j,k,l}$ denotes the summation over the indices of the convolutional filters and their corresponding weights. $\frac{\delta f(x)}{\delta W_{i,j,k,l}}$ represents the partial derivative of the output feature maps $f(x)$ with respect to the weights $W_{i,j,k,l}$. and $\langle \circ, \circ \rangle$ denotes the inner product operation, which measures the similarity between the tangent vectors of the neural network parameters.

Matrix Completion is widely used in machine learning applications. It is a powerful technique that leverages mathematical principles and algorithms to infer missing entries in a partially observed matrix. This approach finds applications in diverse fields such as recommendation systems, image inpainting, and collaborative filtering. The fundamental idea behind matrix completion is to exploit the low-rank structure of the underlying matrix, assuming that it can be represented as the product of two low-rank matrices.

Let's denote the partially observed matrix as M, which has dimensions $m \times n$, where m represents the number of rows and n the number of columns. The objective is to estimate the missing entries in M. Matrix completion formulates this task as an optimization problem, aiming to find low-rank matrices X and Y such that their product approximates M:

$$M \simeq X \times Y^T \tag{2.33}$$

To achieve this, ML techniques come into play. One popular approach is to employ singular value decomposition (SVD) to compute the low-rank approximation. SVD decomposes a matrix into three parts: U, $\sum$, and V, where U and V are orthogonal matrices and $\sum$ is a diagonal matrix of singular values. The rank of the matrix is determined by the number of non-zero singular values.

The matrix completion problem can also be formulated as an optimization problem, the objective being to minimize the reconstruction error. This error is typically measured using a loss function, such as the squared Frobenius norm:

$$Loss = ||M - X \times Y^T||_F^2 \tag{2.34}$$

To solve this optimization problem, ML algorithms such as gradient descent, alternating least squares, or nuclear norm minimization can be employed. These algorithms iteratively update the low-rank matrices X and Y until convergence.

Regularization techniques are often used to prevent overfitting and improve generalization. Ridge regression, LASSO, or elastic net regularization can be incorporated into the optimization problem, introducing penalty terms to control the complexity of the learned model.

Moreover, to handle missing entries in the observed matrix, imputation strategies can be employed. These strategies use the available information to estimate the missing values, which are then fed into the matrix completion algorithm. Techniques like mean imputation, regression imputation, or matrix factorization imputation can be used for this purpose.

In recent years, deep learning techniques have also been applied to matrix completion. Deep neural networks can learn complex representations from the observed data, capturing intricate patterns and dependencies. Autoencoders, recurrent neural networks (RNNs), or graph convolutional networks (GCNs) have shown promising results in matrix completion tasks.

In conclusion, matrix completion with machine learning is a valuable approach for inferring missing entries in partially observed matrices. By exploiting the low-rank structure of the underlying matrix and employing optimization algorithms, machine learning techniques can effectively estimate the missing values.

The exposure reconstruction technique for indoor and outdoor scenarios will be presented in this section. First, the application of Machine Learning, specifically Deep Learning, to the task of exposure Map Reconstruction as an image reconstruction problem for indoor scenarios using a specific ***UNet*** *model will be covered. Next, outdoor exposure map reconstruction from 50 sparsely distributed sensors using* ***CNN*** *based* ***cGAN*** *models will be presented. Subsequently, the* ***Unet*** *based indoor reconstruction technique will be compared with cGAN models. Finally, a novel method for urban exposure reconstruction with* ***Infinitely wide CNN*** *by matrix completion will be introduced.*

Contributions

2.3 Proposed Neural Network Architecture

Indoor EMF Exposure Modeling The following sections present an algorithm for estimating electromagnetic field exposure maps using UNet architecture based on CNN. The power map estimation is transformed into an image reconstruction task by image color mapping, where every pixel value of the image represents the received power intensity. The designed model learns wireless signal propagation characteristics in a realistic indoor environment while considering various positions of the Wi-Fi access points. Results show that indoor propagation phenomena and environment models can be learned from data producing an accurate power map to measure the electromagnetic field. In this section, we introduce the reconstruction of RF-EMF exposure for Wi-Fi access points situated at various locations within a realistic indoor environment. In this context, the channel frequencies range from 2.412 GHz to 2.472 GHz. This is achieved using a CNN-based architecture embedding the popular UNet [151] model used for biomedical image segmentation. The introduced reconstruction model is referred to as the Exposure Map Estimation Network (EME-Net). The pixel color in the reference power map image of the indoor environment represents the power intensity.

2.3.1 EME-Net Model

The exposure map estimator system labeled EME-Net based on popular UNet architecture, is composed of two modules in Figure 2.16. The first module is the reduction module and consists of convolutional, max-pooling, and dropout layers that extract the features of the input images by downsampling. The second module is the expansion module: a symmetric expanding path consisting of transposed convolutional layers upsampling the feature matrix. The architecture follows the structure of auto-encoders. The model is designed to capture the information from the training dataset, learn more complex wireless propagation features of the target area, and reconstruct the power map.

Every layer of the expansion module uses skip connections by concatenating the output of the convolutional layers and the feature extraction layer. This is processed through the contraction module of the same level. The contraction module of the proposed EME-Net model encodes and learns features extracted from the input measurement map while keeping the spatial information of the input image. Each function used in the CNN model is described below:

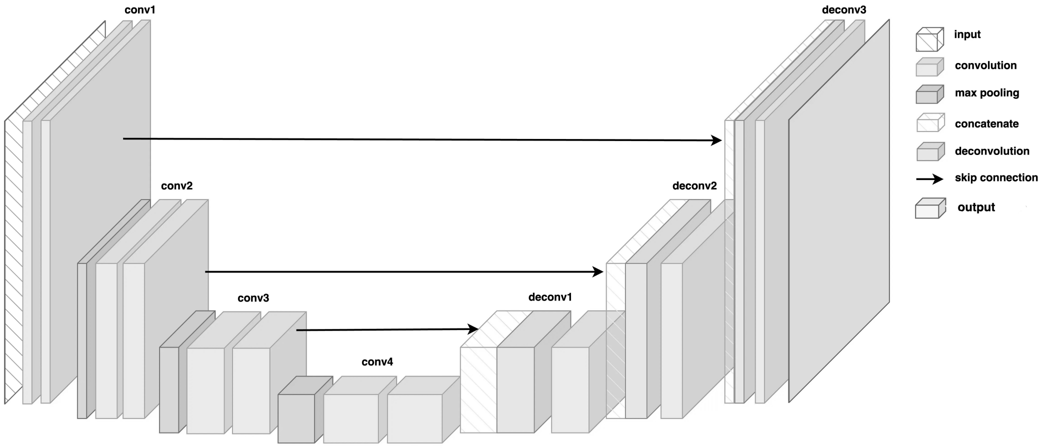

Figure 2.16: The EME-Net model architecture.

convolutional layer A convolutional layer is a fundamental building block of CNNs, which is widely used in image and video analysis tasks. A convolutional layer performs convolutional operations on the input data to extract features, typically used for tasks like image recognition, object detection, and more.

Mathematically, the operation of a convolutional layer can be defined as follows:

Given an input tensor X of shape $(H_{\text{in}}, W_{\text{in}}, C_{\text{in}})$, where H_{in} is the input height, W_{in} is the input width, and C_{in} is the number of input channels. Additionally, let F be the convolutional filter (also known as kernel) of size $(H_{\text{filter}}, W_{\text{filter}}, C_{\text{in}}, C_{\text{out}})$, where H_{filter} and W_{filter} are the filter's height and width, C_{out} is the number of output channels, which corresponds to the number of filters.

The convolutional operation is defined as follows:

For each output channel $k = 1, 2, \ldots, C_{\text{out}}$, the output tensor Y at position (i, j, k) is obtained by applying the convolution operation:

$$Y(i,j,k) = \sum_{c=1}^{C_{\text{in}}} \sum_{p=1}^{H_{\text{filter}}} \sum_{q=1}^{W_{\text{filter}}} X(i+p-1, j+q-1, c) \cdot F(p,q,c,k) \tag{2.35}$$

Where: - $X(i+p-1, j+q-1, c)$ is the value of the input tensor at the position $(i+p-1, j+q-1, c)$. - $F(p,q,c,k)$ is the value of the filter at position (p,q,c,k). - The indices p and q iterate over the height and width of the filter. - The indices i and j iterate over the height and width of the output tensor Y. - The indices c iterate over the input channels.

After the convolution operation, often a bias term is added to each output channel, followed by an activation function like ReLU. This mathematical definition captures the essence of how a convolutional layer processes input data using filters to extract features through convolution operations.

ReLU activation The Rectified Linear Unit (ReLU) is a common activation function used in neural networks. It's defined mathematically as follows:

$$f(x) = \max(0, x) \tag{2.36}$$

Where: - x is the input to the ReLU function. - $\max(0, x)$ means that the output is the maximum of 0 and x. In other words, if x is positive or zero, the output is x; otherwise, if x is negative, the output is 0.

The ReLU activation function introduces non-linearity into the network, allowing it to learn complex relationships and making it especially useful for deep neural networks.

Max pooling is a technique commonly used in CNNs for down-sampling the spatial dimensions of feature maps while retaining important information. It helps reduce the computational complexity of the network and aids in capturing translation-invariant features. Max pooling is typically applied to each feature map independently.

Mathematically, the operation of max pooling can be defined as follows:

Given a 2D input feature map X of size $H_{in} \times W_{in}$, where H_{in} is the height and W_{in} is the width, and a pooling window of size $k \times k$, the output feature map Y of size $H_{out} \times W_{out}$ is obtained by applying max pooling as follows:

$$Y_{i,j} = \max_{m=0}^{k-1} \max_{n=0}^{k-1} X_{i \cdot k+m, j \cdot k+n} \tag{2.37}$$

Where: - $i = 0, 1, \ldots, H_{out} - 1$ - $j = 0, 1, \ldots, W_{out} - 1$ - $Y_{i,j}$ is the value of the output feature map at position (i, j) - $X_{i \cdot k+m, j \cdot k+n}$ are the values in the input feature map covered by the pooling window at position $(i \cdot k + m, j \cdot k + n)$ - k is the size of the pooling window

Max pooling selects the maximum value within each pooling window and places it in the corresponding position of the output feature map. This helps retain the most important information from the input feature map while reducing its spatial dimensions.

Keep in mind that this explanation assumes 2D max pooling for simplicity. In practice, max pooling can also be applied to higher-dimensional feature maps.

Deconvolution/transposed convolution is an operation used in CNNs for upsampling feature maps. Mathematically, the transposed convolution operation takes an input tensor and performs a convolution-like operation using a learnable kernel, but with additional strides and padding. The goal is to upsample the input tensor to a larger size.

Given an input tensor X with dimensions $H \times W \times C_{\text{in}}$, where H is the height, W is the width, and C_{in} is the number of input channels, and a learnable kernel K with dimensions $K_H \times K_W \times C_{\text{out}}$ (where C_{out} is the number of output channels), the transposed convolution operation can be defined as follows:

$$Y[i,j,k] = \sum_{m=0}^{K_H-1} \sum_{n=0}^{K_W-1} \sum_{c=0}^{C_{\text{in}}-1} X[\text{stride} \cdot (i-1) + m, \text{stride} \cdot (j-1) + n, c] \cdot K[m,n,c,k] \tag{2.38}$$

Where: - Y is the output tensor of the transposed convolution operation. - i and j are the spatial indices of the output tensor Y. - k is the index of the output channel of Y. - m and n are the indices of the kernel K. - c is the index of the input channel. - stride is the stride used in the transposed convolution operation.

It's important to note that the transposed convolution operation can also involve adjusting padding to control the spatial dimensions of the output tensor. The choice of stride and padding can influence how much the output tensor is upsampled. Also, the learnable kernel K is often shared across different positions in the input tensor, similar to how convolutional kernels are shared in traditional convolutions.

Skip connections Skip connections, also known as residual connections, are a fundamental architectural component in CNNs that help mitigate the vanishing gradient problem and facilitate the training of very deep networks. They were introduced in the context of the ResNet (Residual Network) architecture. Mathematically, a skip connection can be defined as follows:

Given an input feature map x and a sequence of convolutional layers represented as $F(x)$, a skip connection allows the output of the convolutional layers to be combined with the original input feature map:

$$\text{Output} = f(x) + x \tag{2.39}$$

Here: - $f(x)$ represents the transformation performed by the convolutional layers. - x is the original input feature map. - Output is the final output, which combines the transformed feature map with the original input using element-wise addition.

This approach enables the network to learn the residual information that wasn't captured by the convolutional layers. If the transformation performed by $f(x)$ is close to zero, the skip connection allows the information from x to directly flow through the network, thus helping to prevent the gradients from vanishing during backpropagation.

The explanations of the modules in EME-Net (UNet based) are as follows.

Reduction Module

For the EMENet model, the input layer is a three-dimensional sensor measurement image. In this specific UNet architecture, a version of an encoder can be found. Its purpose is to generate a compact representation of the input image, comprising only the most crucial information within the image. Features are extracted using the encoder, which essentially serves as the means for this extraction.

Furthermore, this lower-dimensional representation obtained by the encoder enables efficient processing and analysis of the image. It allows for faster computations and reduces the computational complexity involved in subsequent stages of the CNN. The extracted features are then utilized for various tasks such as image classification, object detection, and semantic segmentation. Thus, the encoder plays a fundamental role in enhancing the performance and effectiveness of CNN models, an example of this encoder/reduction module is depicted in 2.17.

The reduction module is a chain of convolutional blocks, each of them is composed of

- Two consecutive convolutional layers with kernel size 3×3, a stride of 1. The input layer takes a three-dimensional sensor measurement image, i.e., tensors with size $112 \times 112 \times 4$. This increases the channel number of the feature map and results in new dimensions with 16 channels.
- The employed activation function is the rectified linear unit (ReLU). Taking only positive values after convolution serves to overcome the vanishing gra-

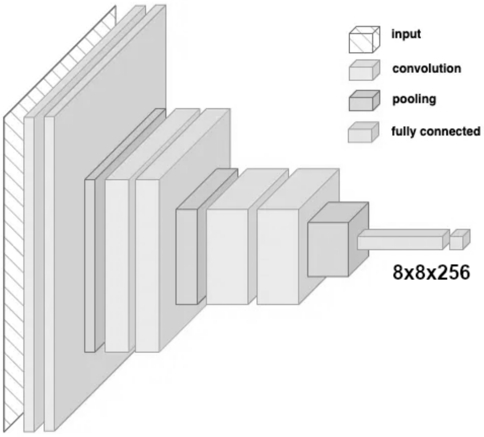

Figure 2.17: The encoder architecture.

dient problem during the backpropagation process while updating the model weights. Convolutional and max pooling layers are depicted in 2.18.

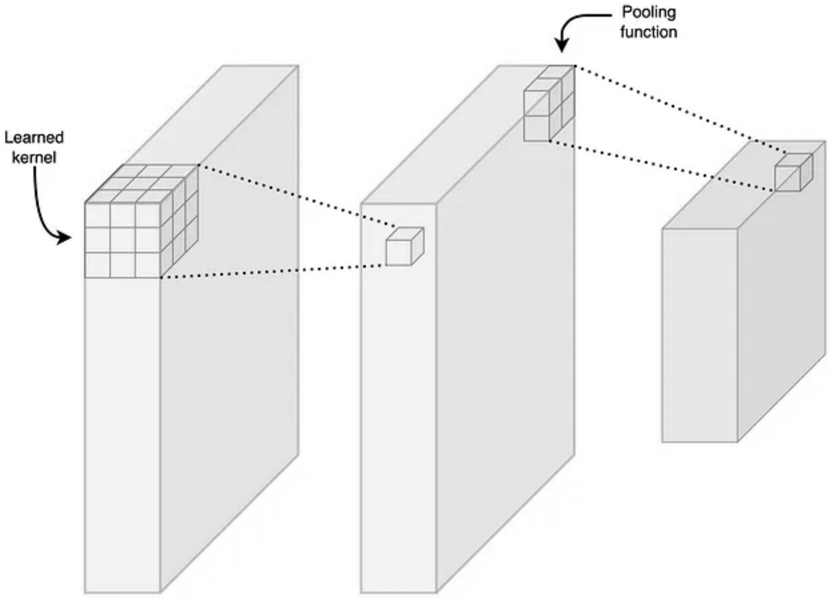

Figure 2.18: convolutional and pooling layers.

- Previous layers are ended with a max-pooling layer. The largest value in each patch of each feature map is taken in this layer, downsampling the feature map. This results in new dimensions: $64 \times 64 \times 16$.

Layers in the first block are repeated in the reduction module, where the feature map size gradually reduces while the depth or channel number increases to 8×8×256.

Expansion Module

In the expansion module or the decoder, five symmetric blocks of the reduction module are used with a transposed convolutional layer for upsampling. Layer parameters are set so that the height and width of the feature map are doubled, whereas the depth (number of channels) is halved.

On the other hand, the increase in dimensionality in upsampled or deconvolution layers is accomplished by employing a learned function. This means that the upsampling function is updated during the model's training process. The pooling layer by learned upsampling function is depicted in 2.19

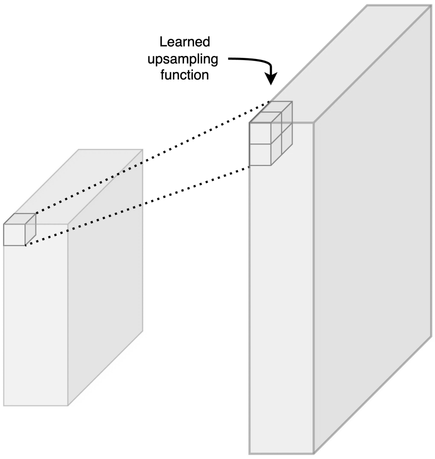

Figure 2.19: deconvolution using a learned upsampling function.

Two successive convolutions are applied to learn more definite features from the feature map. The proposed EME-Net model architecture is symmetric U-shaped and has five blocks on each module.

Outdoor EMF Exposure Modeling This section presents a conditional Generative Adversarial Network to address this issue. The main objective is to reconstruct the electromagnetic field exposure map accurately according to the environment's topology from a few sensors located in an outdoor urban environment. The model is trained to learn and estimate the propagation characteristics of the electromagnetic field according to the topology of a given environment.

Although sensor networks and on-site measurements are essential, they are confined systems that only allow a limited amount of EMF exposure monitoring. Locations of base stations and mobile devices in an urban setting are influenced by elements including building topology, roadways, vehicles, and urban city topology. To evaluate RF-EMF exposure, a power map must be constructed while taking these relevant factors into account. The challenge is reconstructing the EMF exposure map in an urban area from only a few sparsely located sensor-measured power values changing over time according to environment topology and network activity.

This is achieved using a conditional Generative Adversarial Network (cGAN) [124] architecture where the city topology is used as a conditional input. The proposed Exposure Map Generative Adversarial Network (EMGAN) method is an innovative approach inspired by the cGAN architecture. The EMGAN model learns and then estimates the features of outdoor wireless propagation, including diffraction, shadowing reflection, and the impact of building walls, materials, roadways, and city topography.

2.3.2 EMGAN Model

The proposed deep learning method is inspired by a conditional GAN architecture adapted to image-to-image translation. Several studies have been done using this specific model architecture [189, 166, 82] for different applications. The neural network learns to estimate the propagation of an electromagnetic field according to a set of sensors. Our model is conditioned by a map that represents the topology of an environment, thus forcing the model to adapt to a targeted topology, whether indoor or outdoor. Figure 2.20 illustrates cGAN model architecture and the details are given next.

UNet Generator Estimating the EMF exposure map is an image-to-image translation task (architecture details are in section 2.3.1). The model's inputs consist of two images, a sparse sensor measurement map, and the city topology as a conditional input to the generator (the UNet model), represented as a three-dimensional matrix (height, width, and color channel). Three channels—red, green, and blue—are combined to create a picture [148]. A channel represents the color and color intensity of an image. The proposed method reconstructs the final image using a three-dimensional image tensor with three channels. The input sensor measurement map is sparse because each pixel's color intensity corresponds to a sensor-measured value at that location.

The generator is an encoder-decoder model using a UNet architecture (see section 2.3.1). The model takes a source image (e.g., a sensor map) along with a city topology image as a conditional input and generates a target image. It does this by first downsampling or encoding the input image down to a bottleneck layer, then upsampling or decoding the bottleneck representation to the size of the output image. Moreover, skip connections are added between the encoding and corresponding decoding layers for learning features from input images. The model is built to learn more intricate wireless propagation aspects of the target area and translate it to an EMF map for exposure assessment.

Discriminator The PatchGAN discriminator is a specific type of discriminator architecture commonly used in Generative Adversarial Networks (GANs), particularly in the context of image-to-image translation tasks. It's designed to provide high-resolution feedback to the generator about the realism of local patches in the generated images. The discriminator's main function is to distinguish between real and generated images, but the PatchGAN discriminator goes further by providing detailed information about the local regions of an image.

Local Discrimination: Instead of processing the entire input image at once, the PatchGAN discriminator focuses on smaller patches or regions of the image. These patches are usually non-overlapping subregions of the input image. This approach enables the discriminator to provide fine-grained feedback on the realism of local image details.

Convolutional Architecture: The PatchGAN discriminator typically uses a series of convolutional layers to process the image patches. The architecture can vary, but it often consists of multiple convolutional layers followed by downsampling layers such as max-pooling or strided convolutions. These layers capture hierarchical features from the input patches.

Output Interpretation: For each patch, the discriminator produces an output that represents the likelihood or confidence that the given patch is real. In the context of binary classification (real vs. fake), this output can be interpreted as the probability of the patch being real. Since the discriminator operates on patches, it produces an output map where each value corresponds to a patch's classification.

Patch Overlapping: Although the concept of patches suggests non-overlapping regions, in practice, it's common to have overlapping patches. Overlapping patches provide smoother transitions and help avoid artifacts along the patch boundaries.

Using the PatchGAN discriminator in image-to-image translation tasks, such as style transfer or image generation from sketches, often leads to more visually pleasing results. The local focus allows the generator to create realistic textures, patterns, and details, as the discriminator evaluates the quality of these details at a finer level.

In summary, the PatchGAN discriminator is a discriminator architecture tailored to provide localized, high-resolution feedback to the generator in GANs, making it particularly useful for tasks where fine-grained image details matter. In Figure 2.20 a general architecture of the PatchGAN is illustrated.

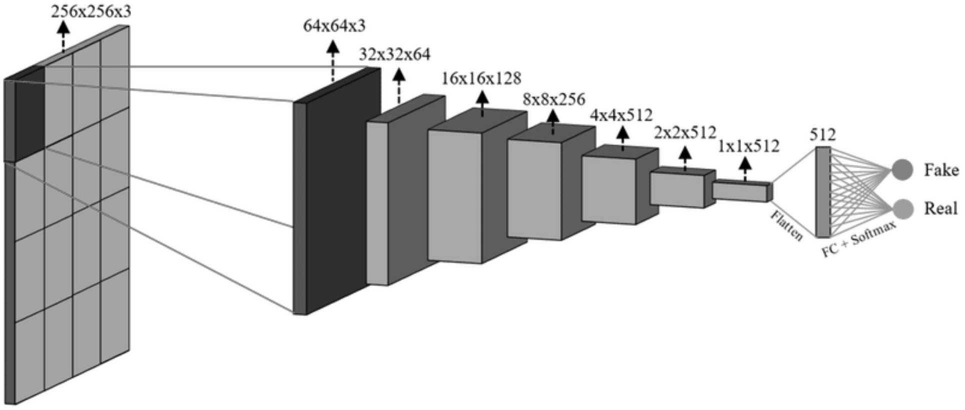

Figure 2.20: PatchGAN Discriminator.

Loss Functions of cGAN model The loss function of the proposed cGAN model contains the discriminator and the generator part as shown in eq. (2.40):

$$L_{cGAN}(G, D) = E_{x,y}[\log D(x, y)] + E_{x,z}[1 - \log D(x, G(x, z)] \tag{2.40}$$

where x is the input image, y is the output image, and z is the conditional image.

The generator G is not only trying to reduce the loss from the discriminator but also trying to move the fake distribution close to the real distribution by using L1 loss which is given in Eq. (2.41):

$$L_{L1}(G) = E_{x,y,z}[\|y - G(x, z)\|] \tag{2.41}$$

The loss function of the generator network is stated in (2.42):

$$G^{\star} = \arg\min_{G}\max_{D} +L_{cGAN}(G, D) + \lambda_{L1}(G) \tag{2.42}$$

In this section, we discussed CNN-based conditional generative model architecture and implementation for outdoor exposure reconstruction. Recent works based on conditional GAN models [124], where inference is conditioned by rules, e.g., physical laws or structural constraints, tend to better address this issue. However, no solution based on this architecture has been proposed so far for the analysis of outdoor electromagnetic field inference. In chapter 3 we present the results.

2.3.3 EME-CNTK

Infinite width neural networks: a convolutional neural tangent kernel (CNTK) [187, 186] is computed for an infinitely wide convolutional neural network whose training dynamics can be completely described by a closed-form formula. This CNTK is utilized to impute the target matrix and estimate EMF exposure from a few sensor-measured values located in an urban environment.

One big issue though is that we do not have access to a reference covering the full map. as explained in section 2.1.2, using a ray-tracing simulator for instance to generate the reference and train the neural networks. Simulations are complex tasks, especially because the number of active base stations from different technologies and operators should be taken into account and we do not have access to the network configuration: what are the powers and beams used by the base stations? We want to propose a solution that does not require reference maps and uses only the measurement points to train the network and reconstruct the exposure map. As shown in [89, 196, 70], expanding the size of the neural network models larger improves the efficiency of the model. The advantages of wider neural network models for generalization and efficiency in classification and feature learning tasks have been highlighted in numerous recent experiments [198, 128] (see section 2.2.2). In the infinite-width limit [97, 130, 42, 118], ANNs are known to be comparable to Gaussian processes, which links them to kernel methods. Therefore, exposure reconstruction is achieved through neural tangent kernels (NTK) [83] for convolutional neural network [96] where the neural network size approaches infinity [186, 98, 25]. The proposed Exposure Map reconstruction method using convolutional neural tangent kernel (CNTK) [102, 12], EME-CNTK, is an innovative approach inspired by the unobserved data imputation in a matrix, also known as image reconstruction using neural networks.

The exposure map reconstruction problem is defined as missing data imputation in images. We propose to address the problem as missing data imputation or image inpainting using CNTK [12]. The exposure map is reconstructed using only data recorded from a few sparse sensor values in a 1 km^2 area. No complete exposure map as a reference is used in the proposed method for reconstruction. A high-level overview of our approach is depicted in Figure 2.21.

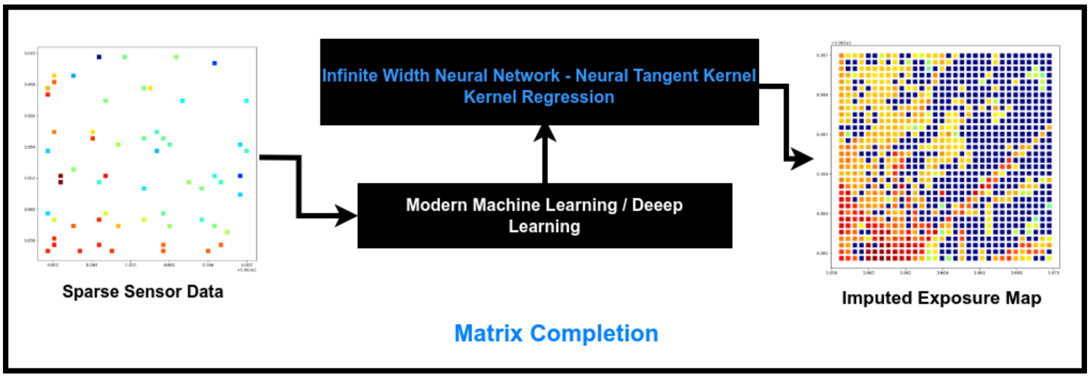

Figure 2.21: Overview of the proposed EME-CNTK approach, which exploits the width limits of neural networks to faithfully and rapidly reconstruct an exposure field. Based on a set of measurements from a sparse sensor network and the terrain map, the neural network, based on ConvNet, infers a coherent exposure field. The main contribution lies in the construction of the kernel and the computation of the priors.

To apply matrix completion for exposure map reconstruction, We need to construct the kernel and then apply kernel regression.

2.3.3.1 Kernel Construction

The NTK is constructed as described in section 2.2.2.3. The NTK method shows that for infinitely wide networks, the neural network behavior is analogous to a continuous kernel function. The kernel is given by the network architecture and the initialization of the kernels/filters and the network parameters. In traditional supervised learning, the target is to learn a mapping function between data X and labels Y. The feed-forward deep neural network is a function γ_ψ that can be represented as a formation of $\gamma_\psi(x) = \gamma_{\psi_k}\phi(\gamma_{\psi_{k-1}}\phi(...(\gamma_{\psi_1}(x))...))$, where x is the input and γ_{ψ_k} is the layer functions. Layer functions can be designed as required, but commonly they are formed by connecting simple scalar-valued functions called neurons, which represent a linear function followed by a non-linear function as activation ϕ [71]. In [179], exposure in an urban area in Paris city was estimated using an artificial neural network from a few sparsely distributed sensors. In that work, the ANN model was trained by minimizing mean squared error (MSE) loss while having 5 input features such as location, transmitter distance to sensors, etc. In our method, exposure values from sensors in γ are modeled using a neural network function γ_ψ using SGD (Stochastic Gradient Descent) in Eq. (2.43) for the proposed method.

$$\gamma_\psi(x) = \gamma_{\psi_k}\phi(\gamma_{\psi_{k-1}}\phi(...(\gamma_{\psi_1}(A))...)) \tag{2.43}$$

Previous studies have demonstrated that using priors [171, 40, 29] where the channels of prior are drawn from a stationary distribution can yield better outcomes [30, 171] for inpainting tasks. In this work, A is a matrix, the size is defined as $A \in \mathbb{R}^{c\times m\times n}$, where m and n are the rows and the columns of A, c is the channel information and its initialization is called the prior. $A \in \mathbb{R}^{c\times m\times n}$ is considered to be a sensor-base prior (SBP) or, i.i.d. a random tensor, where the channels of A are taken from a normal distribution (random normal prior - RNP). The SBP contains the sensor data at one time stamp with the base station location defined in A. The accuracy of the reconstruction is influenced by this prior that captures the relationship among the coordinates within the target matrix, resembling semi-supervised learning and Such priors are extensively used in tasks related to image inpainting [171]. The work by Jacot et al. [83] demonstrates that in the case of overparameterized or infinitely wide neural networks, their behavior closely mimics that of a kernel function. Consequently, solving kernel regression with NTK, as outlined by [12, 83], is equivalent. The definition of NTK is given by:

Definition (Neural Tangent Kernel) *Let* $f(w) : \mathbb{R}^P \to \mathbb{R}$ *denote a neural network with initial parameters* $w^{(0)}$. *The* ***neural tangent kernel,*** $K : \mathbb{R} \times \mathbb{R} \to \mathbb{R}$ *is a positive semi-definite function given by:*

$$K(x, x') = \langle \nabla f_x(w^{(0)}), \nabla f_{x'}(w^{(0)}) \rangle, \tag{2.44}$$

where $w^{(0)} \in \mathbb{R}^P$ *denotes the parameters at initialization.*

Using Convolutional NTK (CNTK) for exposure map reconstruction is a mapping of element coordinates in the matrix γ to the observed entries present in γ. The element coordinates of γ are selected to map the information to the exposure map reconstruction task. The CNTK [12] is constructed from a convolutional network with a different number of layers, kernel size, and convolution incorporated with down and upsampling. The CNN model details and definition for deriving CNTK are as follows.

$$K(x, x') = \langle \frac{\delta f(x)}{\delta W_{i,j,k,l}} \times \frac{\delta f(x')}{\delta W_{i,j,k,l}} \rangle, \tag{2.45}$$

where x and x' are input samples, $W_{i,j,k,l}$ represents the weights of the convolutional filters, $\sum_{i,j,k,l}$ denotes the summation over the indices of the convolutional filters and their corresponding weights. $\frac{\delta f(x)}{\delta W_{i,j,k,l}}$ represents the partial derivative of the output feature maps $f(x)$ with respect to the weights $W_{i,j,k,l}$. and $\langle \circ, \circ \rangle$ denotes the inner product operation, which measures the similarity between the tangent vectors of the neural network parameters. The L-th layer CNTK kernel described as $\Theta^{(L)}(x, x') \in \mathbb{R}^{[M]\times[N]\times[M]\times[N]}$, and output of CNTK is :

$$K(x, x') = [\Theta^{L}(A, A')]_{i,j,i',j'} \tag{2.46}$$

2.3.3.2 CNN architecture

During training, at initialization, a convolutional neural network is used and the kernel is derived when the Network's width tends to be infinity. We choose a CNN with eight convolutional layers following the architecture used in [171], where each layer is accompanied by *LeakyReLU* activation and down and upsampling by mimicking (nearest neighbor and bilinear interpolation methods and layers, models, activation functions, kernel functions implementation from [114, 172, 175, 133, 26]). The slope of the activation is set to 0.05 and stabilization technique is applied to mitigate exploding or vanishing gradient issues during training. Model parameters, Layers, and activation functions are taken from [172, 133]. The weights and filters are initialized randomly. The architecture of the CNN is shown in Figure 2.22.

The dimension of the matrix can be 32×32, 64×64, 128×128. In this work, the dimension of the grid was limited to 32×32 and 64×64 and only 60 observations from the sparsely distributed sensors are available.

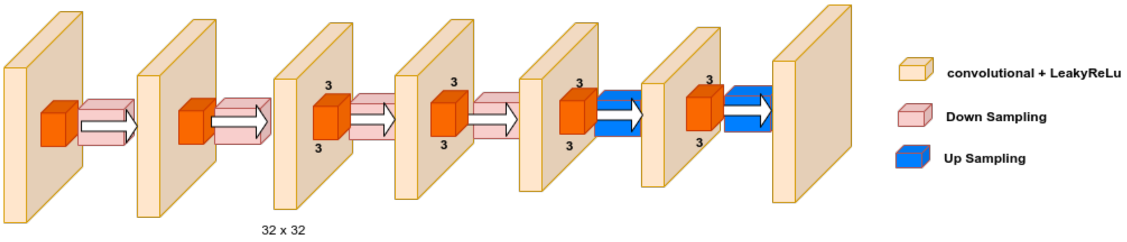

Figure 2.22: ConvNet Architecture with kernel size = 3

Reconstructing the map. For the exposure reconstruction task, two procedures are explored, kernel regression by CNTK.

2.3.3.3 Kernel Regression by CNTK

The goal of this method is to fill in missing entries (missing pixel values) as a linear combination of training examples (observed pixel values) in the corrupted exposure map image.

The corrupted exposure matrix denoted by γ has dimensions 32×32. Let ψ_{obs} represent the matrix containing only the observed entries (available pixel values in γ), constituting 60 entries as sensor data in a grid comprising 1024 elements and rest ψ_{unobs}.

Each entry (p, q) in the matrix γ within ψ_{obs} corresponds to a linear combination of pixel coordinates in γ in the CNTK $\psi \in \mathbb{R}^{mn \times mn}$. The available exposure value in γ is E. The conventional approach for solving a linear system for the weight vector ω involves computing ω as $\omega = \psi_{obs}^{-1} E$ [12].

From ψ that corresponds to the unobserved entries (missing pixel values) for the exposure value, we can calculate $\psi_{unobs} \times \omega$.

Conclusion

Within this chapter, we provided a concise introduction to both supervised and semi-supervised learning paradigms. We have illustrated their foundational principles and delved into primary approaches characteristic of each paradigm, namely EME-Net, EMGAN, and EME-CNTK. Overall, our investigation highlights the importance of considering the computational complexity of image inpainting tasks when using high-resolution grids. The use of pre-conditioned gradient descent methods offers a promising solution to the computational challenges posed by these tasks. An evaluation of the presented methods is provided in Chapter 3.

Chapter 3

Evaluation

In Chapter 2, we introduced a novel approach utilizing CNN models to address exposure reconstruction challenges in both indoor and outdoor environments. In this chapter, we conduct a comprehensive analysis of our experimental results, encompassing both qualitative and quantitative evaluations. Our investigation will begin with indoor scenarios followed by outdoor. The EME-Net and EME-GAN models are used and compared in the indoor case. In the outdoor scenario, the cGAN and EME-CNTK will be tested.

3.1 Metrics

3.1.1 Peak Signal-to-Noise Ratio - PSNR

The peak signal-to-noise ratio (PSNR) [137] and structural similarity index (SSIM) [180] are used between the reconstructed map and the reference map in order to assess the model performance. Values between -1 and 1, where 1 denotes perfect resemblance, are provided by the SSIM model, which captures the observed change in the structural information of the picture. The PSNR test compares the distortion power to the greatest possible pixel intensity. The SSIM index is calculated on various windows of an image. The measure between two windows x and y of common size $N \times N$ is given below along with PSNR:

$$\mathrm{PSNR} = 10\log_{10} * \frac{\mathrm{MAX}_\mathrm{I}^2}{\mathrm{MSE}}, \tag{3.1}$$

where MAX_I is the maximum possible pixel value of the image. When the pixels are represented using 8 bits per sample, this is 255. The degree of inaccuracy in statistical models is measured by the mean squared error, or MSE. Between the observed and estimated values, it evaluates the average squared difference. The MSE is equal to 0 when a model is error-free. Its value increases when model error does as well. The mean squared deviation is another name for the mean squared error (MSE).

3.1.2 Structural Similarity Index - SSIM

The SSIM [180] is given by:

$$\mathrm{SSIM(x,y)} = \frac{(2\mu_x\mu_y + c_1)(2\sigma_{xy} + c_2)}{(\mu_x^2 + \mu_y^2 + c_1)(\sigma_x^2 + \sigma_y^2 + c_2)}, \tag{3.2}$$

where, μ_x and μ_y are the pixel sample mean of x and y, μ_y. σ_x^2 and σ_y^2 are the variance of x and y, σ_{xy} is the covariance of x and y. $c_1 = (k_1L)^2$ and $c_2 = (k_2L)^2$ are the variables to stabilize the division with weak denominator, where L is the dynamic range of the pixel values. k_1 and k_2 are set to 0.01 and 0.03.

Finally, we will consider the pixel-to-pixel error that we will denote by R. R, in dB, is given by:

$$R(x,y) = 10\log_{10}\left(\frac{x}{y}\right). \tag{3.3}$$

3.1.3 Cumulative Distribution Function - CDF & Probability Density Function- PDF

We represent either the probability distribution of R or the cumulative distribution of R. This allows us to have a more detailed understanding of the error behavior. Kernel density estimation (KDE) is a non-parametric approach to estimate the probability density function of a random variable based on kernels as weights. It is an application of kernel smoothing for probability density estimation. Its kernel density estimator is :

$$f_h(x) = \frac{1}{nh}\sum_{i=1}^{n} K(\frac{x - x_i}{h}) \tag{3.4}$$

where K is the kernel — a non-negative function — and $h > 0$ is a smoothing parameter called the bandwidth. A kernel with subscript h is called the scaled kernel and defined as $K_h(x) = \frac{1}{h} \times K(x/h)$. Intuitively one wants to choose h as small as the data will allow; however, there is always a trade-off between the bias of the estimator and its variance. The proposed approach is based on a gaussian kernel where each data point contributes a normal distribution (bell curve) centered at that point.

3.1.4 Root Mean Squared Error - RMSE

In statistics, the mean squared error (RMSE) or root mean squared deviation (RMSD) of an estimator (of a procedure for estimating an unobserved quantity) measures the average of the squares of the errors—that is, the average squared difference between the estimated values and the actual value. RMSE is a risk function, corresponding to the expected value of the squared error loss.

$$RMSE = \sqrt{\frac{1}{n}\sum_{i=1}^{n}\left(Y_i - \hat{Y_i}\right)^2}. \tag{3.5}$$

In the following sections, these metrics are used for quantitative analysis of our methods in indoor and outdoor scenarios.

3.2 Indoor Scenarios

Simulation setup: Results obtained by UNet and cGAN models are presented in this section. For training both models, 'IndoorExpDataset' described in section 2.1.1 is used. This dataset is generated using 'PyLayers' software. The considered building is a single floor which represents a typical multi-room office environment. There are 14 rooms and a corridor where the floor area is 2100 m^2, room dimensions are $10m \times 10m \times 3m$, and the corridor has the dimensions $70m \times 10m \times 3m$. Windows are located on the north and south side of the office environment. Each room has a wooden door, and the walls are constructed with plaster with a thickness of 10 cm. The ceiling and floor are made using reinforced concrete. For training the model, 6 Wi-Fi access points are considered with different locations in the scenarios while keeping two or three of them in the corridor and three in the rooms. Using 'PyLayers', we simulate the received power maps in a dense environment. For the sensor map, 5 sensors are placed in each room and 26 sensors in the corridor randomly. Figure 3.1 illustrates the reference image and sensor map image for this indoor scenario.

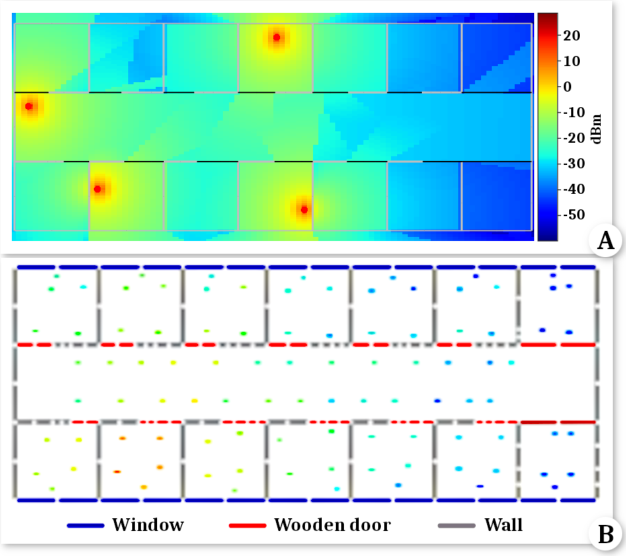

Figure 3.1: RF-EMF exposure reference map (ieee 80211b, fc=2.412 GHz polar: p). The red dots represent the Wi-Fi access points. The color gradient corresponds to the power of the electromagnetic field.

Training setup and losses are depicted in tables 3.3 and 3.2 respectively. Following the training of the EME-Net derived model with the minimum loss was chosen and

Parameters	Value
Total number of images	12660
Input samples	10128
Validation set	1266
Test set	100
Optimizer	ADAM -Adaptive Moment Algorithm
Learning rate	1×10^{-4}
Batch size	2
Decay rate	1×10^{-6}
Epochs	12

Table 3.1: Training parameters.

results are shown in Table 3.2.

Model (or configuration)	Trainable parameters	loss
EME-Net	**1942428**	**0.0017**

Table 3.2: Total number of parameters for each reconstruction model and training loss.

The Visual analysis and comparative analysis are given in the following sections.

3.2.1 EME-Net

3.2.1.1 Visual Analysis

We evaluate the proposed EME-Net model performance was investigated by increasing the number of measurement points. This is done by taking 15, 30, 50, and 96 pixels as measurement points from the reference image.

The reconstructed maps, depicted in Figure 3.2, showcase the outcomes achieved by utilizing the EME-Net model on different test sets with varying numbers of measurement points (15, 50, and 96 pixels). When employing only 15 sensors as input, the reconstruction quality appears to be inadequate. However, as the number of sensor points is increased to 96, the reconstructed map exhibits similarity to the reference map.

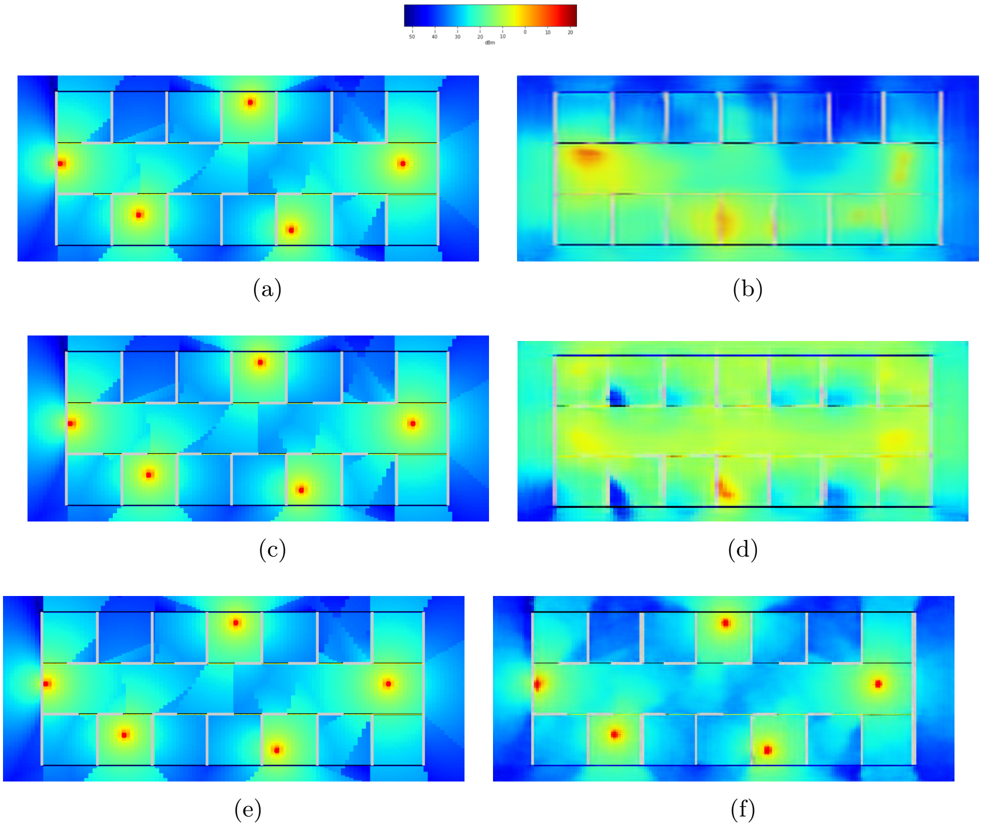

(a) (b)

(c) (d)

(e) (f)

Figure 3.2: Reconstructed maps (right column) and its corresponding original exposure maps (left column) when **(a)** 15, **(c)** 50, **(e)** 90 pixels used as sensor measurements at random locations.

3.2.1.2 Quantitative analysis

Figure 3.3 presents both averages of SSIM and PSNR increase together with the number of measurement points. About the slight downfall of the average SSIM at 90 measurements, this effect is due to the use of raw pixel intensities globally. The same trend indicates that the reconstruction process is coherent for similarity and image quality.

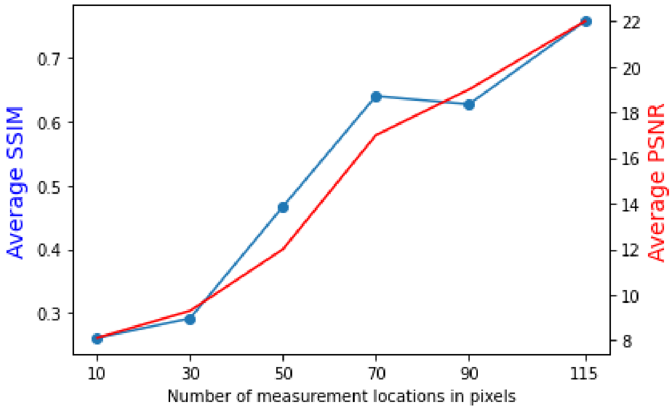

Figure 3.3: Reference Vs. Reconstructed - average SSIM and PSNR.

3.2.2 EME-GAN

In this section experiments conducted using cGAN model described in section 2.3.2 is presented. The EME-GAN model is used to infer indoor exposure maps by utilizing the 'IndoorExpDataset' described in section 2.1.1. Training setup is depicted in tables 3.3.

Parameters	Value
Total number of images	2286
Input samples	2086
Validation set	100
Test set	100
Optimizer	ADAM -Adaptive Moment Algorithm
Learning rate	1×10^{-4}
Batch size	2
Decay rate	1×10^{-6}
Epochs	13000

Table 3.3: Training parameters.

3.2.2.1 Visual Analysis

The EMGAN model's reconstructed maps are illustrated in Figure 3.4 with 5 access points in training data. With only 60 measurement points, the EME-NET reconstruction fails to represent the reference map. In addition, with increased measurement points (96), EMGAN outperforms EME-NET with better reconstruction quality and a low error ratio R near zero. Even with 8 access points as unseen data, our model performs well and surpasses EME-NET in reconstruction compared to the reference map.

3.2.2.2 Quantitative analysis

Both average SSIM and PSNR increase along with the number of measurement locations are shown in Figure 3.5. The use of global raw pixel intensities is the reason for the small decline in the average SSIM at 96 measurements. The same trend indicates that the reconstruction process is coherent with respect to similarity and image quality. When increasing the number of measurement points to 96, SSIM and PSNR values increased to 0.72 and 0.90 which shows good reconstruction quality.

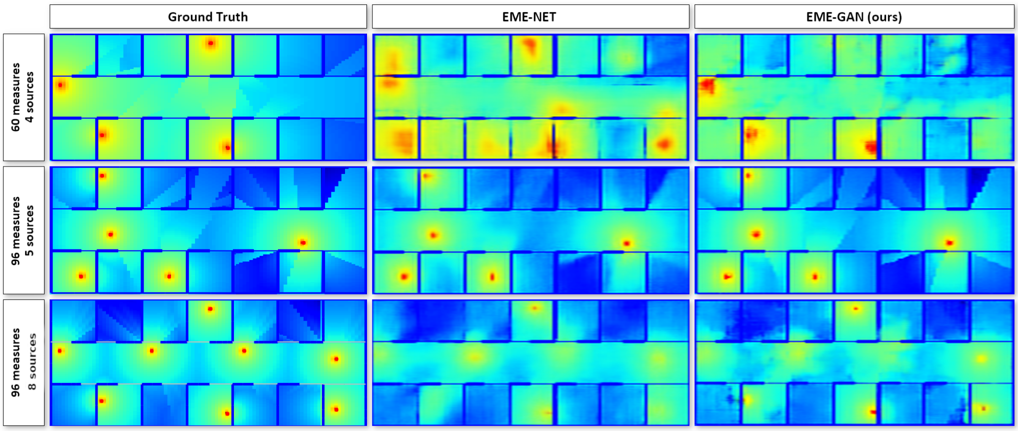

Figure 3.4: Comparison of inferred exposure maps from different measurement points configurations.

The same trend indicates that the reconstruction process is coherent with respect to similarity and image quality.

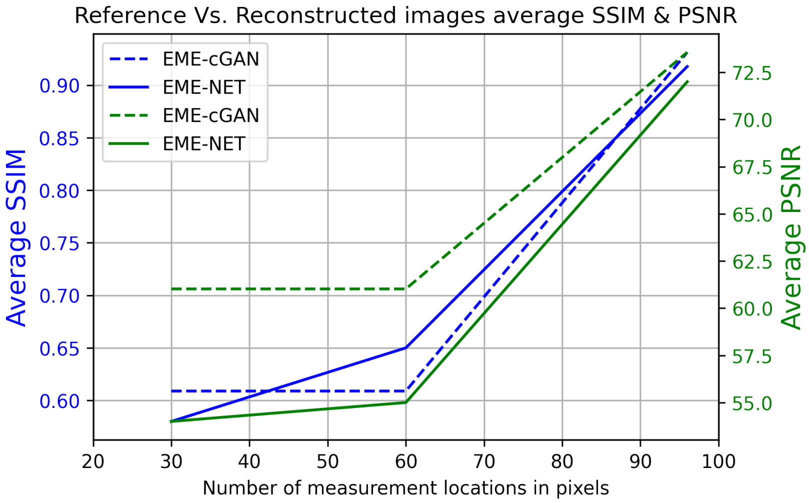

Figure 3.5: PSNR and SSIM comparison with a different number of measurements.

The PDF of the ratio of the reconstructed maps to the reference for the proposed EME-GAN model and EME-Net, is shown in Figure 3.6. A Gaussian random variable can be used to closely approach the error ratio (in dB) distribution. First, we note that the mean is very low from 30 to 96 sensors, that is at 96 points mean is 0.03 and 1.93 for EMGAN and EME-Net models, indicating that there is not much

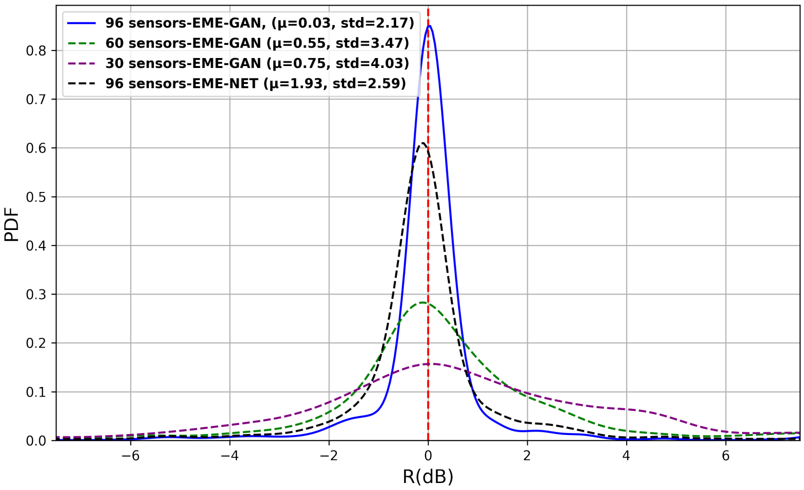

Figure 3.6: PDF of error ratio R when varying number of sensors.

bias in the prediction stages. The second crucial observation is that, as the number of sensors increases, the variance decreases from 4.03 to 2.17.

Figure 3.7 shows the CDF of the error ratio $|R|$, which is the comparison of the reconstructed map to the reference map, for the proposed EME-GAN and EME-NET model with varying numbers of sensors. Moreover, Figure 3.7 demonstrates that, despite the upbeat visual evaluation, the performance of the suggested EME-GAN inclines with an increase in the number of sensors. We can see that approximately 80% of the values fall below 1 dB while 96 sensors are used.

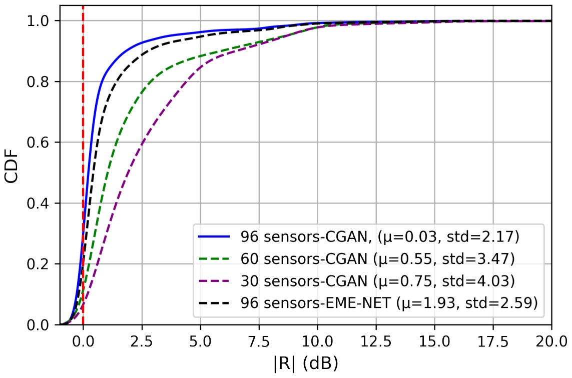

Figure 3.7: CDF of $|R|$ when different models are used.

3.3 Outdoor Scenarios

Simulation setup: Results obtained by EMGAN (cGAN) model and CNTK method are presented in this section. For training, cGAN based EMGAN model, 'VenerisLilleExposure' described in section 2.1.2 is used. This dataset is generated using 'VENERIS' software. A map of 1 km^2 area of Lille city center from 'OpenStreetMap' is used for the ray launching simulations in Veneris. More specifically, the dataset contains objects with rough surfaces like 3D building walls, statues, roads, etc., interacting with the rays in complex ways. Moreover, gaps in the object, e.g., bridges and rays at different levels, can pass or reflect from such objects. The presence of the object in the environment, and several ray interactions result in a complex power distribution representing a real-life environment. The transmitters are assumed to use an isotropic antenna, producing omnidirectional radio waves. The height and power of the transmitting antenna were set at a maximum of 15 meters and 20 Watts, respectively. The dataset consists of 3003 EMF exposure maps which are used as reference for training the EMGAN model (see section 2.1.2). For the input training samples, 50 sensor measurement locations are used. Training parameters are listed in Table 3.4.

Table 3.4: Training parameters.

Parameters	Value
Total number of images	3003
Train set	2500
Validation set	100
Test set	403
Optimizer	ADAM
Learning rate	4×10^{-4}
Batch size	2
Decay rate	1×10^{-6}
Epochs	139000

3.3.1 EMGAN

3.3.1.1 Visual analysis

The proposed EMGAN model is compared with the EME-Net model and the Kriging method when only 50 measurement points are considered. All models are trained and tested on the same training and test data sets. As illustrated in Figure 3.8, the proposed EMGAN model outperforms the kriging model. The EMGAN based (3.8d) reconstructed map looks very close to the reference, and few details are missed by the EME-Net based (3.8c), whereas the kriging-based (3.8b) encounters significant loss. Though the Kriging approach was not optimized, so the comparison is not completely fair.

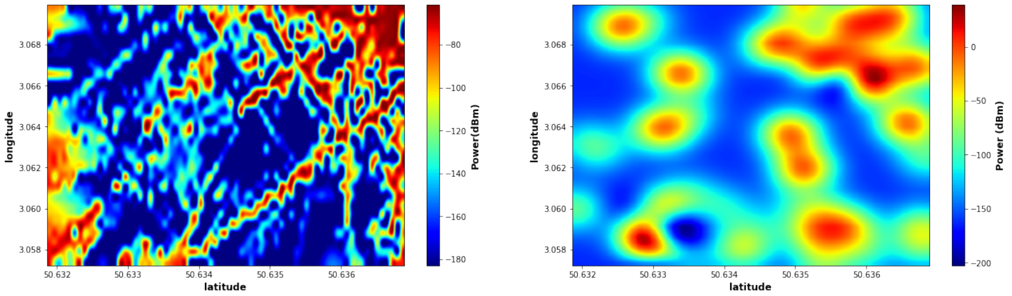

(a) reference

(b) Simple kriging

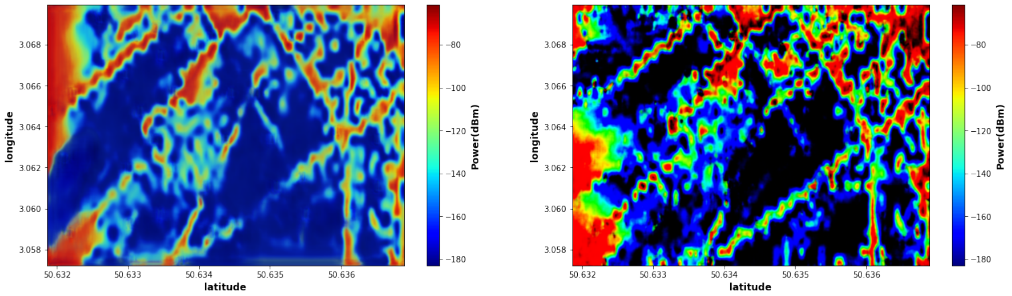

(c) EME-Net model

(d) Proposed EMGAN model

Figure 3.8: Comparison of Reconstructed maps of the proposed model and other different models.

Additionally, the proposed EMGAN model performance is analyzed by varying the number of measurement points. Figure 3.9 shows the EMGAN based reconstructed maps using 15 and 30 sensor measurement points. The figure illustrates that the performance of the proposed EMGAN model remains consistent even when a few measurement points are considered, although some degradation can be observed. The error map between the reconstructed map and the reference is illustrated in Figure 3.10. The error map shows that the proposed EMGAN model (3.10c, 3.10d and 3.10e) has a significantly low error compared to the other models. The kriging approach exhibits very poor results. The approach is not well adapted to such spatial

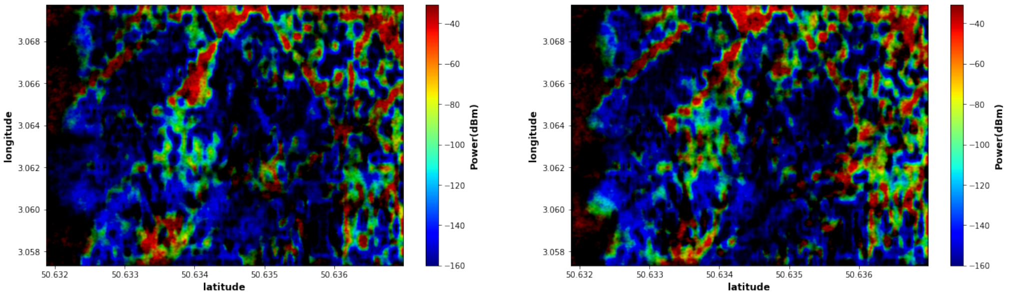

(a) Using 15 sensor map (b) Using 30 sensor map

Figure 3.9: EMGAN-based Reconstructed maps when different number of sensors are considered.

undersampling. Further studies, though, should be done to take into consideration the environment topology and the propagation models. This however is a different approach and is out of the scope of this work.

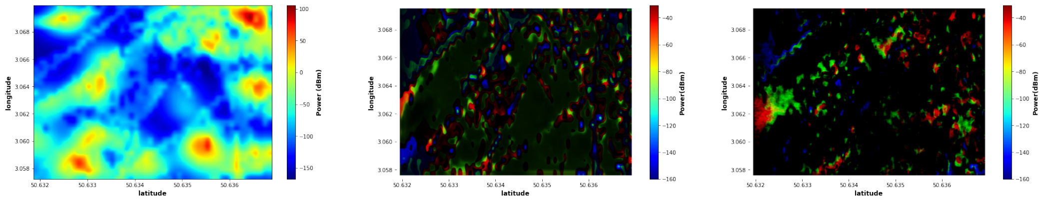

(a) Kriging 50 sensors (b) EME-Net 50 sensors (c) EMGAN 15 sensors

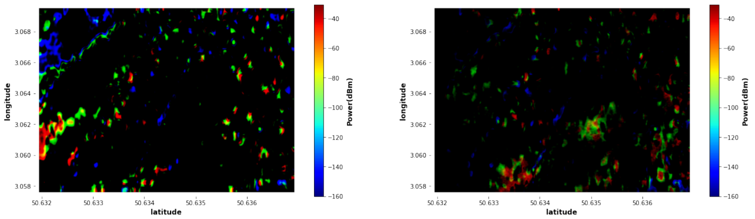

(d) EMGAN 30 sensors (e) EMGAN 50 sensors

Figure 3.10: Error maps of the proposed EMGAN for different numbers of sensors and EME-Net model.

3.3.1.2 Quantitative Analysis

Figure 3.11 presents the averages of SSIM and PSNR as a function of the number of measurement points. As the number of measurement points rises, so do the averages of SSIM and PSNR. The same trend indicates that the reconstruction process is coherent regarding similarity and image quality.

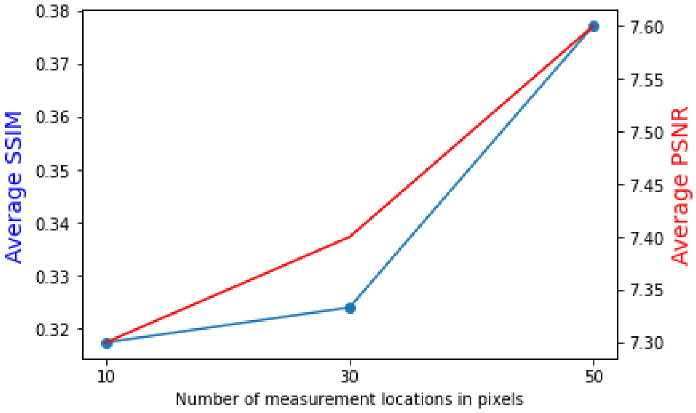

Figure 3.11: Average SSIM and PSNR of the proposed EMGAN with a varying number of measurement points.

The CDFs of R of the proposed EMGAN and other models is shown in Figure 3.12. As illustrated in Figure 3.12a, the proposed EMGAN model outperforms the kriging and EME-Net methods. In addition, Figure 3.12b shows that, despite the optimistic visual evaluation, the performance of the proposed EMGAN degrades as the number of sensors decreases. On the 1 km^2 area we are studying, 50 sensors are needed to avoid some large deviations.

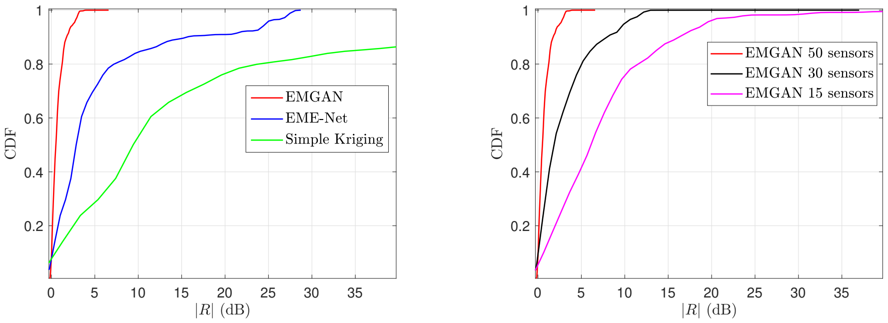

(a)

(b)

Figure 3.12: CDF of ratio R - **a)** models, and **b)** varying number of sensors between the reconstructed map and reference.

In Figure 3.13, the PDF of the ratio between the reconstructed maps and the reference of the proposed EMGAN model with different numbers of sensors, EME-Net, and simple kriging methods are presented. The error ratio (in dB) distribution can be well approximated by a Gaussian random variable. We first notice that the mean is rather close to 0, meaning there is no significant bias in the prediction steps. The second important point is that we note the variance reduction with the increase in the sensor number. With 50 sensors in the studied 1 km^2 area, the variance is reduced to 0.85, which seems a reasonable value for an exposimetry study, resulting in more than 80% of the error ratio below 3 dB. We also notice that the EME-Net approach with 50 sensors is not as good as EMGAN with 30. This is expected because the EMGAN takes into account the environment map, so, in particular, the locations of the building.

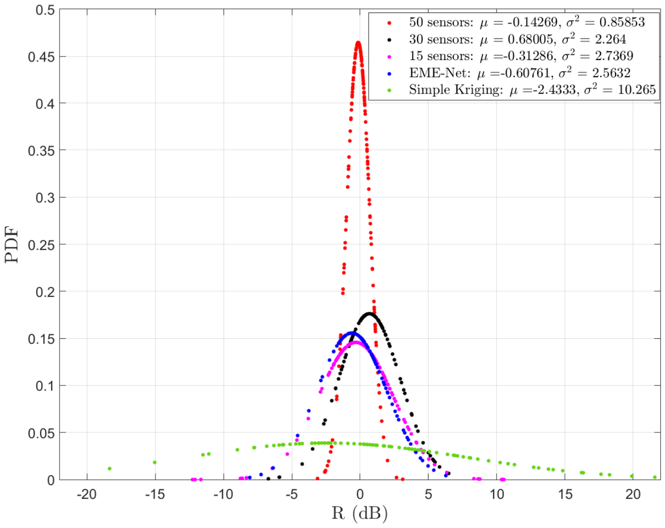

Figure 3.13: The probability density of the ratio R between the reconstructed map and reference when different numbers of sensors are used.

3.3.2 EME-CNTK

The results of EME-CNTK are described in four steps :

- Sensors numbers
- Comparison with EMGAN and EME-Net
- Number of transmitter in the scenario
- Grid size

3.3.2.1 Visual analysis

Number of Sensors

The proposed EME-CNTK method is compared with the EME-Net and EMGAN methods when only 60 measurement points are considered. EME-Net and EMGAN are trained and tested on the same data sets generated by Veneris. As illustrated in Figure 3.14, the EME-CNTK reconstruction with 100 sensors (3.14b) looks very close to the simulated map (3.14a). Figures (3.14c) and (3.14d) show reconstruction when 60 and 40 sensor data were used. In Figure 3.15 shows the comparisons with EMGAN and EMENet reconstruction with 60 sensors.

Comparison with EMGAN and EME-Net

In figure 3.16 The error map between the reconstructed map and the reference is illustrated. The error map shows that the proposed method (Figure a,b,c) has a significantly low error compared to the other models (Figure d,e).

Number of transmitters

Additionally, the proposed method's performance is analyzed by increasing the number of transmitters. Figure 3.17 shows the EME-CNTK based reconstructed maps using 40 sensors (3.17b) and 60 sensors (3.17a) measurement points. The figure illustrates that the performance of the proposed EME-CNTK method remains consistent even when 2 transmitters are used, although some degradation can be observed for 40 sensor measured maps.

In Figure 3.18, the error map of 60 and 40 sensors reconstruction using EME-CNTK, when 2 transmitters are transmitting is depicted. We can see the reconstruction is good as the error map shows less error in them.

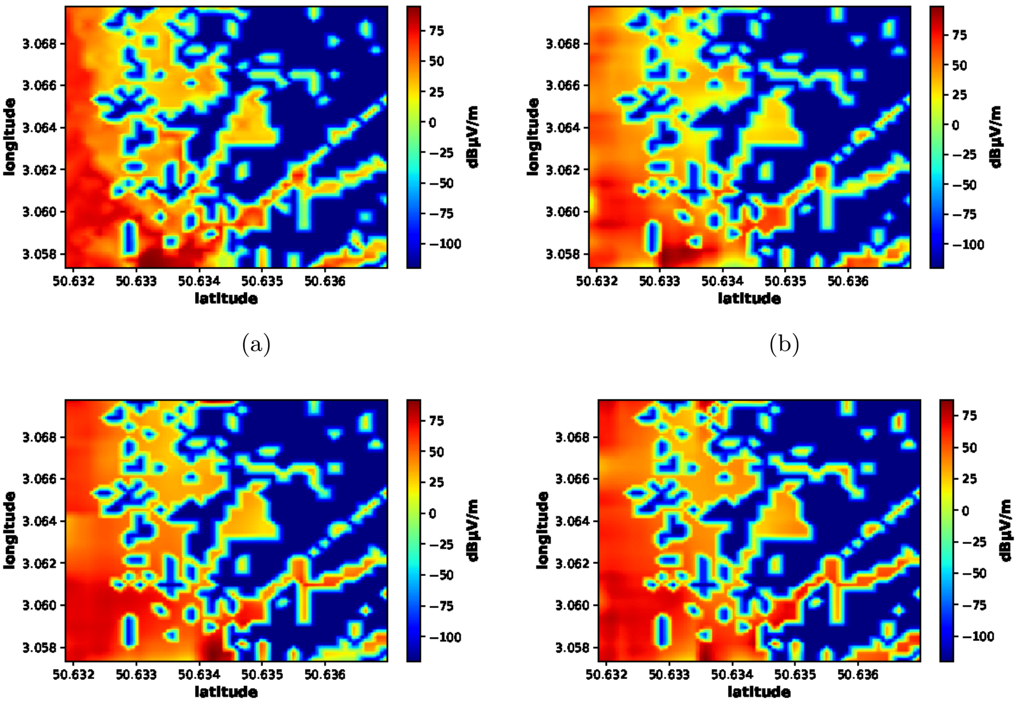

(a) (b)

(c) (d)

Figure 3.14: Comparison of Reconstructed maps of the proposed method with reference map **a)** simulated map from Veneris, **b)**100, **c)** 60, **d)** 40 sensors are used by EME-CNTK

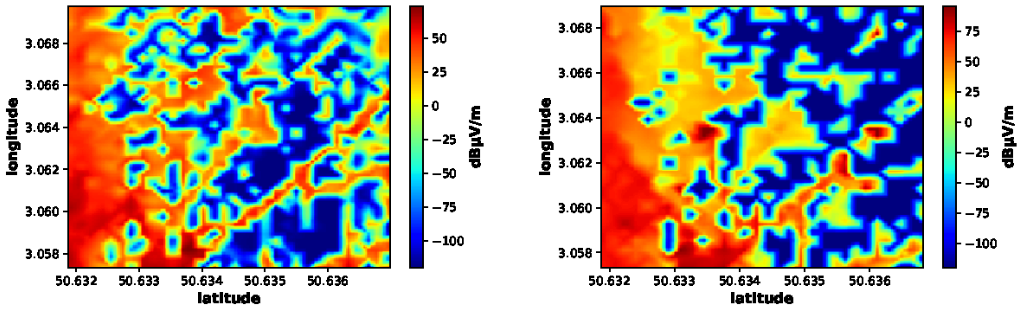

(a) (b)

Figure 3.15: Comparison of Reconstructed maps of the proposed method and **a)** EME-Net model using 60 sensors, **b)** EMGAN model using 60 sensors

Grid size

Figure 3.19, illustrates the reconstructed map using 60 sensors when the grid size

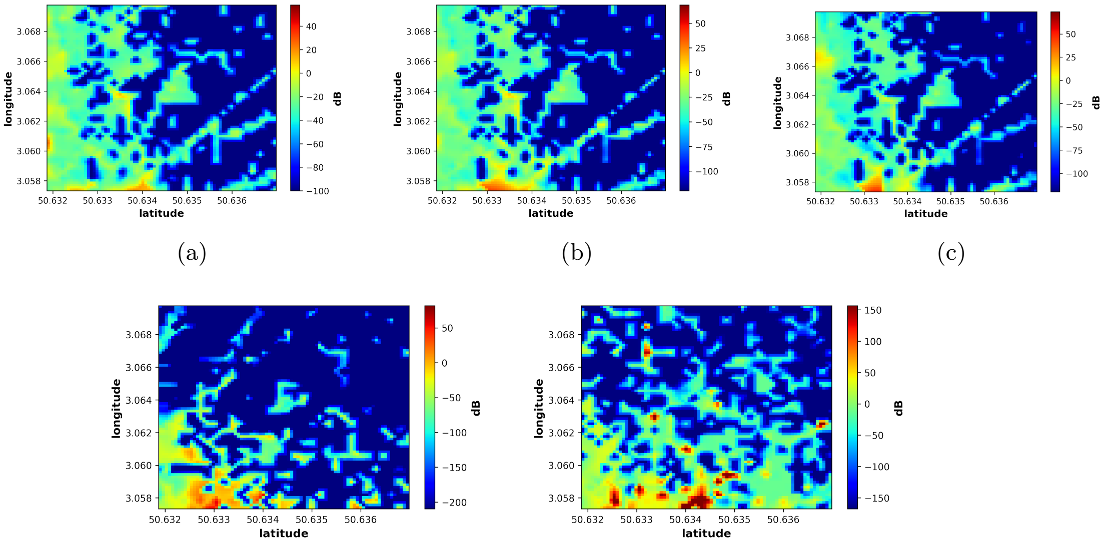

(a) (b) (c)

(d) (e)

Figure 3.16: Error maps of the proposed method for different numbers of sensors **a)** EME-CNTK 100 sensors, **b)** EME-CNTK 60 sensors, **c)** EME-CNTK 40 sensors, and **d)** EMGAN 60 sensors, **e)** EME-NET 60 sensors model.

is 64 × 64. Figure 3.19a and 3.19b show the reference map for 32 × 32 and 64 × 64 respectively. Reconstructed maps for gird size 64 × 64 using our method are shown in 3.19d.

In Figure 3.20, the error map of 60 sensors reconstruction using EME-CNTK, when one transmitter and grid resolution is increased to 64×64 is depicted. We can see the reconstruction is good as the error map shows small errors in them.

3.3.2.2 Quantitative Analysis

The MSE of the predicted and actual values or exposure is given in Table 3.5. From the table, it can be seen that with an increasing number of sensors, the MSE decreases leading to better reconstruction performance by the proposed method.

The CDF of the error ratio R, the ratio between the reconstructed map and the reference, of the proposed EME-CNTK and other models is shown in Figure 3.21. As illustrated in Figure 3.21a, the proposed method works similarly to EMGAN and EME-Net methods. In addition, Figure 3.21b shows that, despite the optimistic visual evaluation, the performance of the proposed method degrades as the

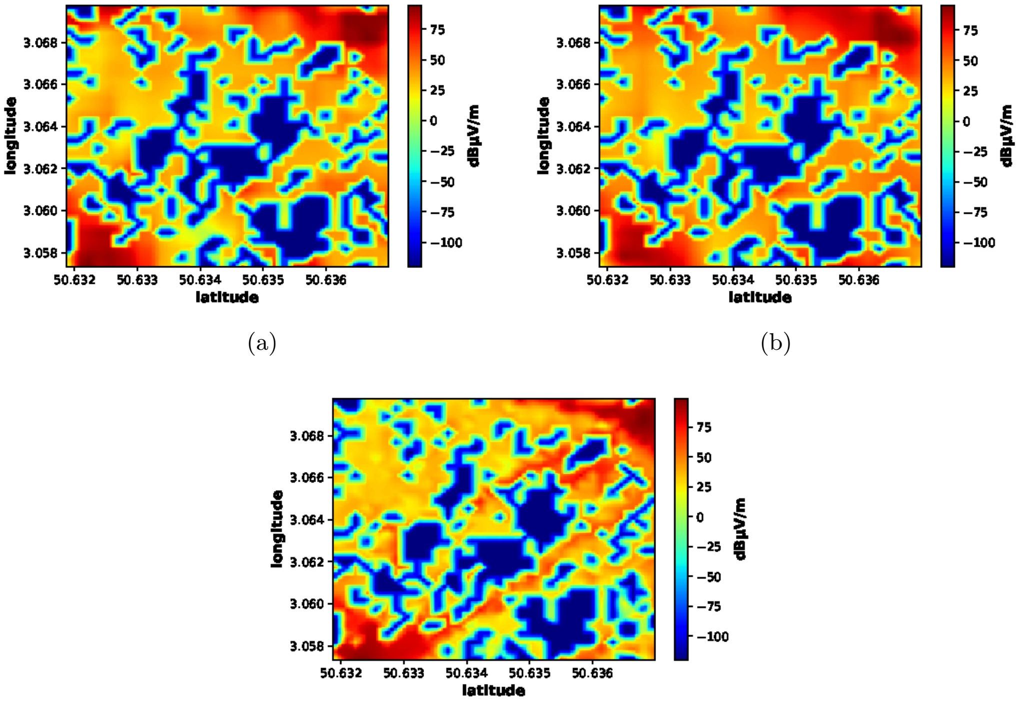

(a)

(b)

(c)

Figure 3.17: Comparison of Reconstructed maps of the proposed method when 2 transmitters are used **a)** EME-CNTK 60 sensors 2TX, **b)** EME-CNTK 40 sensors 2TX, **c)** reference map

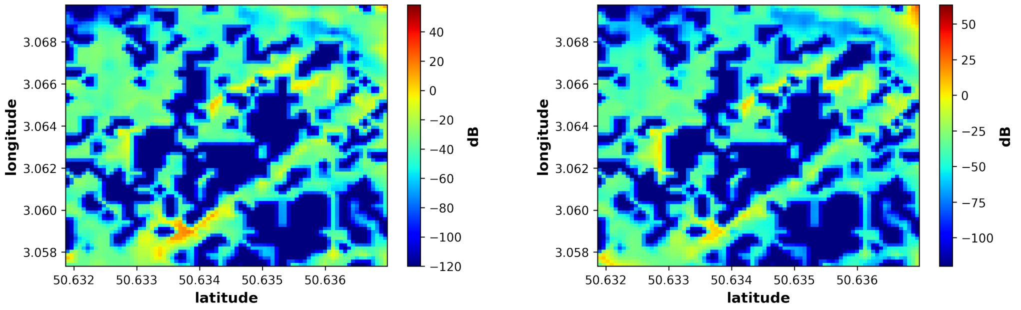

(a)

(b)

Figure 3.18: Error map of **a)** 60 sensors reconstruction and **b)** 40 sensors reconstruction when 2 transmitters are used.

number of sensors decreases. On the 1 km^2 at least 60 sensors are needed to avoid

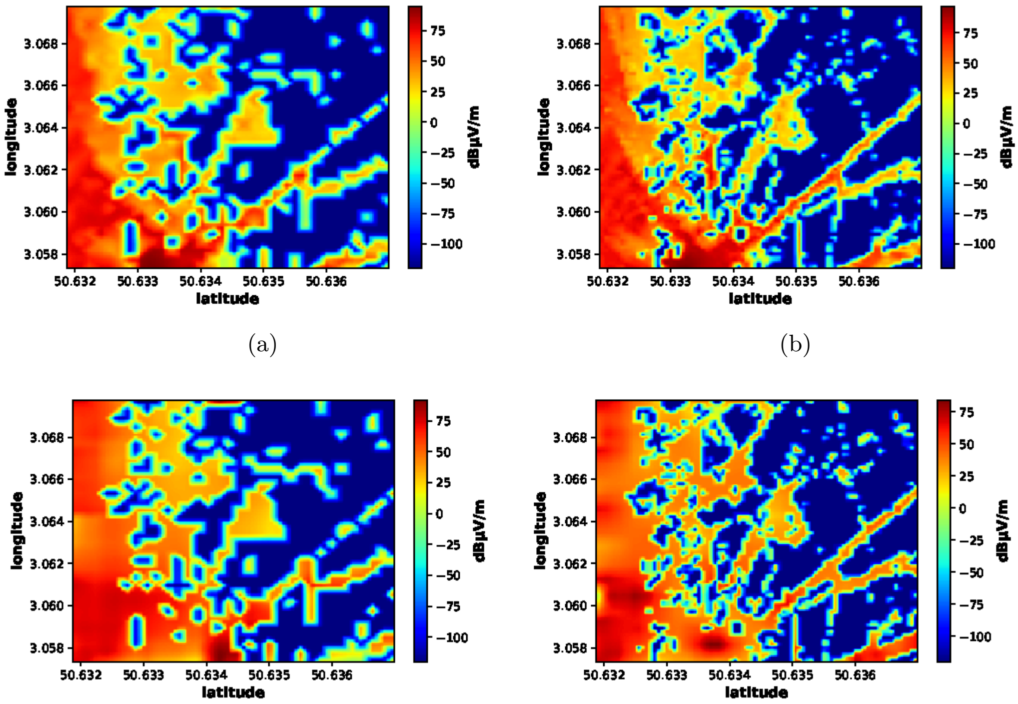

(a) (b)

(c) (d)

Figure 3.19: Comparison of reconstructed exposure map with reference when different grid size is used **a)** EME-CNTK - 60 sensors resolution 32 × 32, **b)** EME-CNTK - 60 sensors resolution 64 × 64, **c)** Reference map 32 × 32, **d)** reference map when resolution is 64 × 64

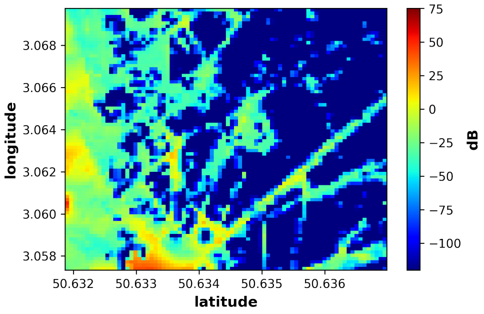

Figure 3.20: Error map of 60 sensors reconstruction and when grid size 64 × 64 is used.

large deviations. Moreover, point to be noted that, EMGAN and EME-Net methods are trained on reference generated by Veneris, so the EMGAN model performs better than EME-CNTK. Figure 3.22a, presents the PDF of the ratio between the reconstructed maps and the reference of the proposed EME-CNTK method with dif-

Number of sensors	RMSE
20 / km^2	0.00910
40 / km^2	0.00687
60 / km^2	0.00681
100 / km^2	0.00636

Table 3.5: RMSE of the estimated exposure values using our approach.

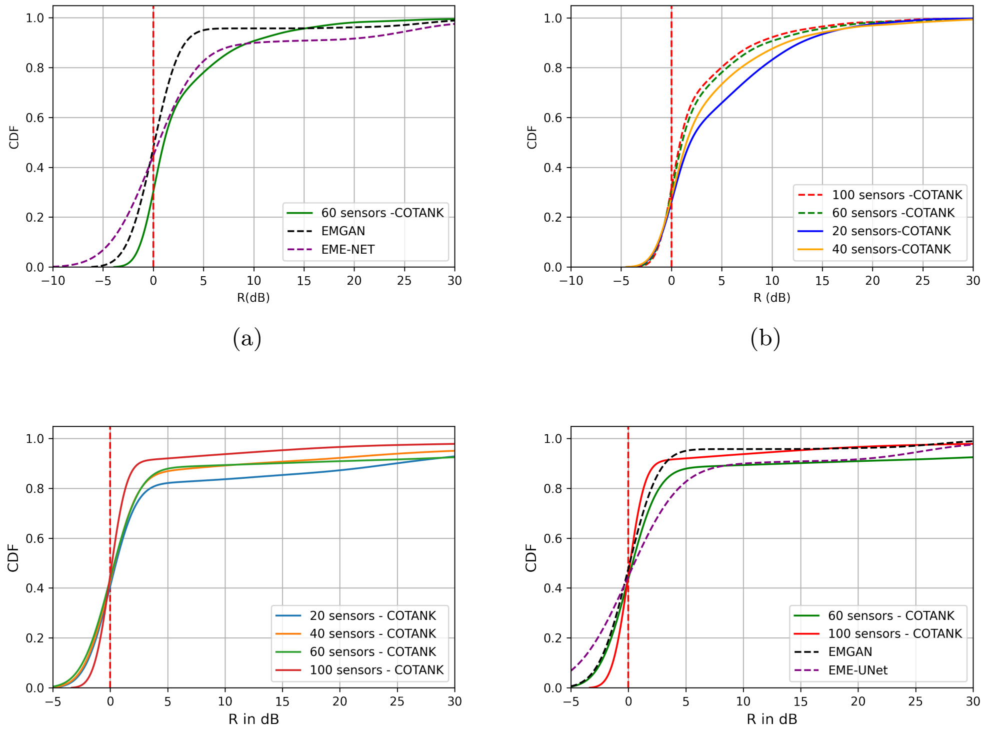

(a) (b)

(c) (d)

Figure 3.21: CDF of the models as a function of the ratio R between the reconstructed map and reference **a)** Different models, **b)** with varying number of sensors, **c)** CDF sensors EME-CNTK 100 images , **d)** different models

ferent numbers of sensors, PDF of EME-Net, and EMGAN methods are presented in Figure 3.22b. The Gaussian probability distribution can closely approximate the distribution of error ratio (in dB). Again we note that the average is quite close to 0, indicating significance in prediction processes. Moreover, it's significant to observe the diminishing variance as the number of sensors increases. In the examined 1 km^2

area with 60 sensors, the variance reduces to 4.25, which appears to be a reasonable value for exposimetry research, leading to more than 80% of error ratios falling below 4dB for the investigated scenario with 60 sensors. Additionally, we acknowledge that utilizing 60 sensors using EME-Net and EMGAN methods provides comparable results while reducing the sensor count to 40 or 20 leads to significantly inaccurate reconstruction.

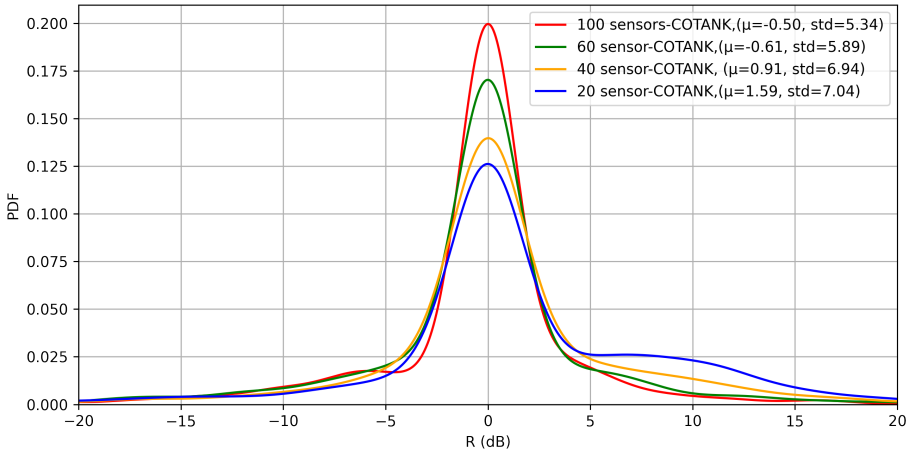

(a)

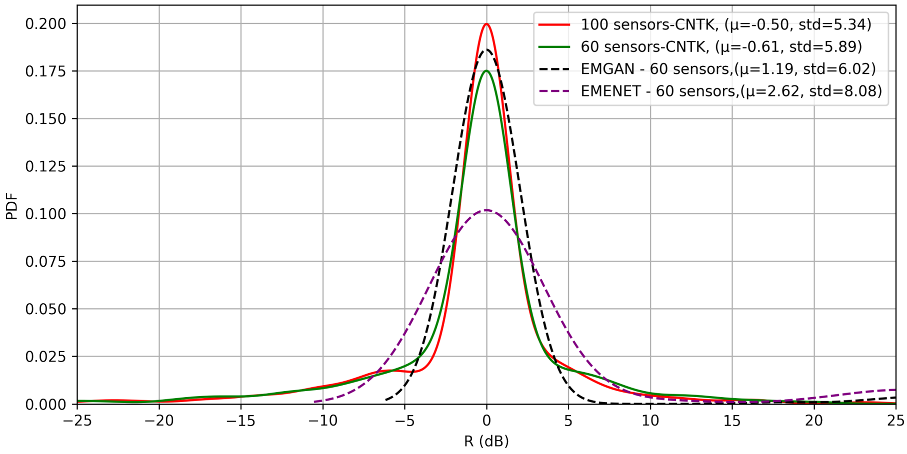

(b)

Figure 3.22: The probability density of the ratio R between the reconstructed map and reference when **a)** different numbers of sensors and **b)** different models are used.

The CDF of R, of the reconstructed map and the reference exposure map for 64×64 resolution, when EME-CNTK is used shown in Figure 3.23. In Figure 3.23a, the CDF of the error ratio is shown when grid size is increased to 64×64, and 3.23b shows the CDF when 2 transmitters are used.

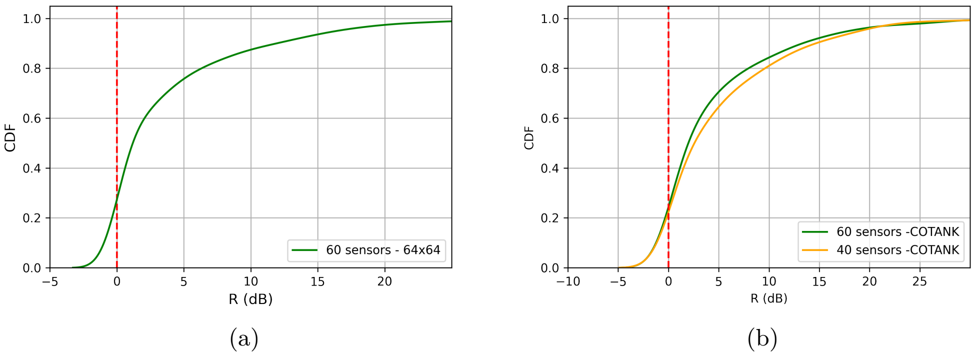

(a)

(b)

Figure 3.23: The CDF of the ratio R between the reconstructed map and reference map for 64×64 and when 2 transmitters are used **a)** CDF of R for higher resolution, **b)**CDF of R when 2 transmitter emitting for 40 and 60 sensors.

Figure 3.24 illustrates When a threshold of above 0.005 V/m is considered (below the threshold, exposure is assumed to be negligible) are analyzed for both the cases grid 64×64 and 2 transmitters, the CDF of error ratio R is illustrated in Figure 3.23a and 3.24b. As illustrated reconstruction by our method works quite well having around 80% values fall under $4dB$ when a higher resolution grid is utilized in the selected area of exposure study.

3.3.2.3 Impact of density of the sensors

We also investigate how our method performs when the number of sensor is increased in the target 1 km^2 area. The mean and standard deviation of the error ratio R are calculated when 20, 40, 60, and 100 sensors are distributed sparsely in target ROI. As we can see in table 3.6 when the number of sensors is very low as 20 the mean is rather very high at 1.39 and the std error is higher at 7.04, but with an increasing number of sensors from 40, 60 and 100 the mean decreases with decreasing std. error gradually. That means the density of the sensor and how the sensors are distributed that plays a vital role in the reconstruction process.

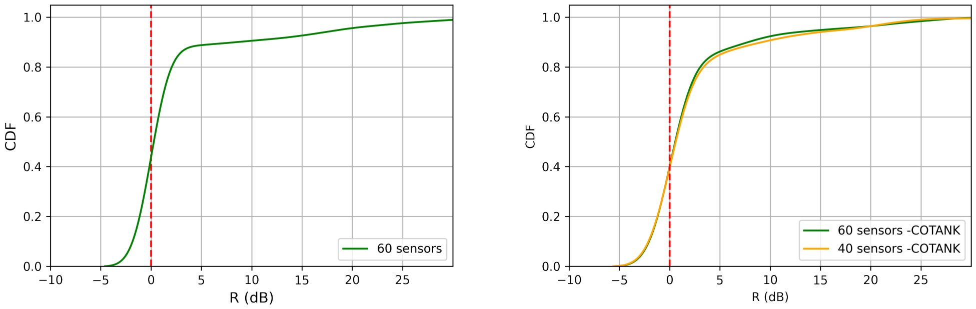

(a) (b)

Figure 3.24: The CDF of the ratio R between the reconstructed map and reference for 64×64 and when 2 transmitters are used **a)** CDF of R for higher resolution, **b)**CDF of R when 2 transmitter is used, **c)** CDF of R 64x64, **d)** CDF of R with 2 transmitters 100 images

Sensor Density	Mean	Std. Error
20 / km^2	1.59	7.04
40 / km^2	0.91	6.94
60 / km^2	0.61	3.29
100 / km^2	0.31	3.40

Table 3.6: Comparison of error with density of sensors

3.3.2.4 Comparative Analysis of Time Efficiency

We assessed the efficiency of the proposed method in terms of the time required for inference and training. Our analysis shows that the cGAN-based approach EMGAN and Unet-based approach EME-Net required 1.5 hours and approximately 20 minutes, respectively, to train on a machine with 4GB GPU memory (Intel core i7, NVIDIA Quadro T1000). EMGAN iterated over 139K epochs, while EME-Net trained for 20 epochs. Both models required higher memory, approximately 6-13 GB, and utilized 3.25GB GPU memory for training. In contrast, our proposed EME-CNTK method took only 0.00014 seconds to impute the matrix and the inference time was below 0.0003 seconds as shown in Table 3.7. (The table is given in the next page.)

Method	Memory Usage	Training	Inference
EMEGAN	13GB RAM + 3.2GB VRAM	1.5 Hrs	2s
EME-Net	6GB RAM + 2.5GB VRAM	20 min	1.5s
EME-CNTK	200MB RAM	**0.00014 s**	**0.000045 s**
EME-CNTK	300MB RAM 300MB VRAM	**0.00011 s**	**0.00003 s**

Table 3.7: Comparison of the proposed method with others with machine configuration and time

This chapter presents a quantitative analysis of the EME-NET, EMGAN, EME-GAN, and EME-CNTK methods. Three distinct variants of these techniques were employed, and the experimental results indicate their superior performance compared to previously available methods in the areas of reconstruction accuracy, time efficiency, and hardware utilization. Moreover, the following additional observations emerged from our investigation:

- Reconstruction Accuracy: Our findings demonstrate that the EME-NET, EMGAN, EME-GAN, and EME-CNTK methods consistently yield accurate reconstructions across diverse datasets. The quantitative evaluation revealed a significant improvement in reconstruction fidelity, surpassing the capabilities of existing approaches.
- Time Efficiency: We conducted comprehensive timing analyses to assess the computational efficiency of the aforementioned methods. The results unequivocally indicate that EME-CNTK compared to EME-NET, EMGAN and EME-GAN exhibit remarkable speed enhancements, allowing for efficient processing of large-scale datasets within minimal timeframes.
- Hardware Utilization: Another crucial aspect evaluated was the efficient utilization of hardware resources. Our experiments reveal that the EME-NET, EMGAN, EME-GAN, and EME-CNTK techniques effectively leverage available hardware, resulting in optimized utilization and reduced resource overhead. These findings are particularly significant for resource-constrained envi-

ronments.

The reconstruction of urban EMF exposure maps holds significant importance in assessing the safety of urban environments. These maps provide crucial insights into the distribution and intensity of EMF radiation within urban areas, allowing for a comprehensive evaluation of potential health risks and the development of appropriate mitigation strategies.

Conclusion

In summary, the quantitative analysis presented in this chapter substantiates the superiority of EME-NET, EMGAN, EME-GAN, and EME-CNTK methods over existing techniques, showcasing their exceptional performance in terms of reconstruction accuracy, time efficiency, and hardware utilization. The additional observations further reinforce the significance of these methods in advancing the field of exposure reconstruction.

Discussion and Perspectives

Summary of contributions

In this thesis, we have investigated the potential of employing deep learning to address the exposure estimation problem. This is central to fingerprinting localization techniques, aiming to reduce energy consumption by minimizing reliance on GPS. Previous research has predominantly focused on supervised training of neural network models using generated data, demonstrating their effectiveness in solving this specific task.

In the literature, numerous algorithms have been devised to create maps for power, channel-gain, and exposure. However, these algorithms face significant challenges in accurately estimating map values due to various factors, including environmental architecture, network configuration, and mobile user locations. One prominent drawback of all current schemes is their dependence on precise sensor location information, which is often unattainable in practical scenarios due to propagation phenomena that impact localization pilot signals, such as multipath. Another limitation is the reliance on interpolation methods that lack the capability to learn the intricacies of radio frequency signal propagation, leading to poor performance in strong fading channels.

All current methods of exposure reconstruction with neural network, stochastic geometry, or krigging depends on drive test measurements which do not consider time evolution resulting in one single map in space. In our proposed methods, in Chapter 2, we introduced the EMGAN, EME-Net and EME-CNTK algorithm, which enables the reconstruction of the exposure map using given measurements from a few sparsely distributed sensors. Our proposed algorithm outperformed all the baseline approaches considered and previous methods. This thesis circumvents the above mentioned limitations with the following contributions:

Classical Machine Learning - Conditional Generative Model:

- 'VenerisLillexposure', a public dataset generated by ray-tracing software, offers the opportunity to train various machine learning models in order to generate exposure maps.
- Employing a conditional generative model algorithm, the generator and discriminator models are trained using the environment model image as a conditional input, which is concatenated channel-wise, resulting in the effect of city architecture in output exposure map.

Modern Machine Learning - Infinitely wide CNN model:

- In our proposed method, we introduced a novel approach EME-CNTK, utilizing an infinite-width neural network connecting with Convolutional Neural Tangent Kernel. By employing matrix completion, we successfully reconstructed urban exposure maps using only 60 sensor values over time, without relying on a ground truth full exposure map for training. Implementing the city architecture in the reconstructed maps significantly enhanced the accuracy of the urban exposure maps.
- Our proposed methods incorporate time variation, allowing for generating dynamic maps over time based on the sensor data.
- Exploiting the conventional parametric structure of wireless communication signals, this thesis formulates methodologies to estimate the exposure maps using generative models using ground truth and kernel-based models using only sensor values. Moreover, custom training approaches are devised to enable effective learning from a limited set of measurements.

Limitations & Perspectives

This thesis proposes different methods to reconstruct exposure maps. In the future, the extension of the work in this thesis can be from several perspectives and can be summarized as follows:

Classical Machine Learning - Conditional Generative Model:

⋆ As demonstrated in Chapter 2, cGAN model - EMGAN trained on groundtruth simulated maps from VENERIS software, where only one transmitter is used in the simulation scenario. This ground truth can be updated by simulating actual network activity (i.e. using the actual number of transmitters, the orientation of the antenna, etc.) in VENERIS software which is close to reality.

⋆ Antenna locations and directions can be used as input features in the input image to the generative model to estimate more accurate exposure maps.

⋆ This work can be extended in the temporal dimension to predict exposure maps in future times. time-dependent models can be exploited to achieve this.

Modern Machine Learning - Infinitely Wide CNN:

⋆ In our proposed method EME-CNTK, matrix completion is performed for missing data imputation. To do so, unobserved data coordinates are used as feature information. This approach can be extended by adding missing feature information such as transmitters or base station locations, antenna height, azimuth, beam direction for 5G base stations, etc. which are publicly available. This information can be used to create a dataset and impute missing exposure values by performing matrix completion by selecting the feature information to generate different feature priors for the NTK.

⋆ City topology is added by superimposing on imputed matrix, this can be improved by adding city topology information such as building location, height, wall materials, vegetation type, etc. as a feature map for the data. Another way could be adding it in the kernel itself. Thus further investigation can be conducted to generate exposure maps that will include environment features in the regression step.

In order to address a more comprehensive generalization problem, we also want to investigate the task of transfer learning from one city to another.

Finally, matrix completion has become an effective tool for dealing with missing data in a variety of disciplines. In the area of exposure estimates, particularly in disciplines like wireless communication signals and environmental mapping, matrix completion has some intriguing uses. Matrix completion can effectively impute missing values and calculate exposure levels in certain cases by using feature data and publicly accessible data. There is still scope for improvement although the suggested approaches, such as EME-CNTK, and EMGAN have demonstrated significant potential in improving the precision of missing data imputation and exposure assessment. Exposure maps that are more thorough and accurate may result from the matrix completion process's integration of additional characteristics and environmental data. In conclusion, the presented methods have a great deal of potential for solving the problems associated with missing data and improving exposure estimating techniques. Unquestionably, further investigation and study in this field will result in more reliable and efficient solutions for a variety of real-world applications.

Appendix A

Appendix related to inference on Indoor Environment

A.1 EME-GAN

We present the results of EME-GAN when a different number of sensors is used in the scenario in Figure A.1 and Figure A.2.

Number of sensors: 30

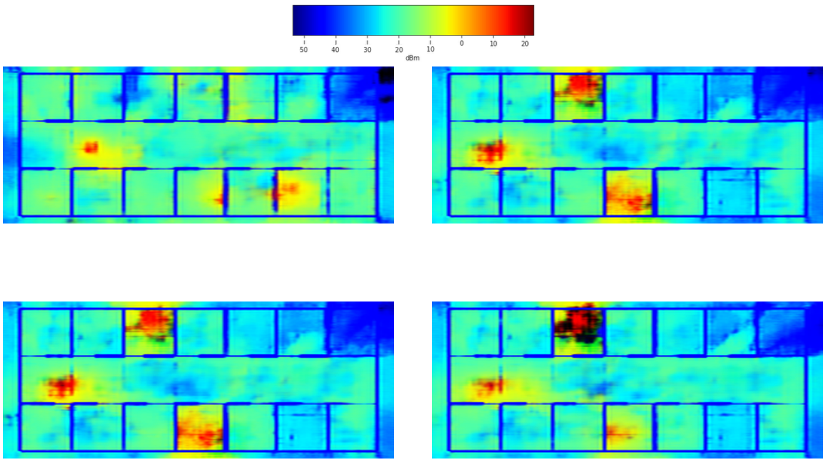

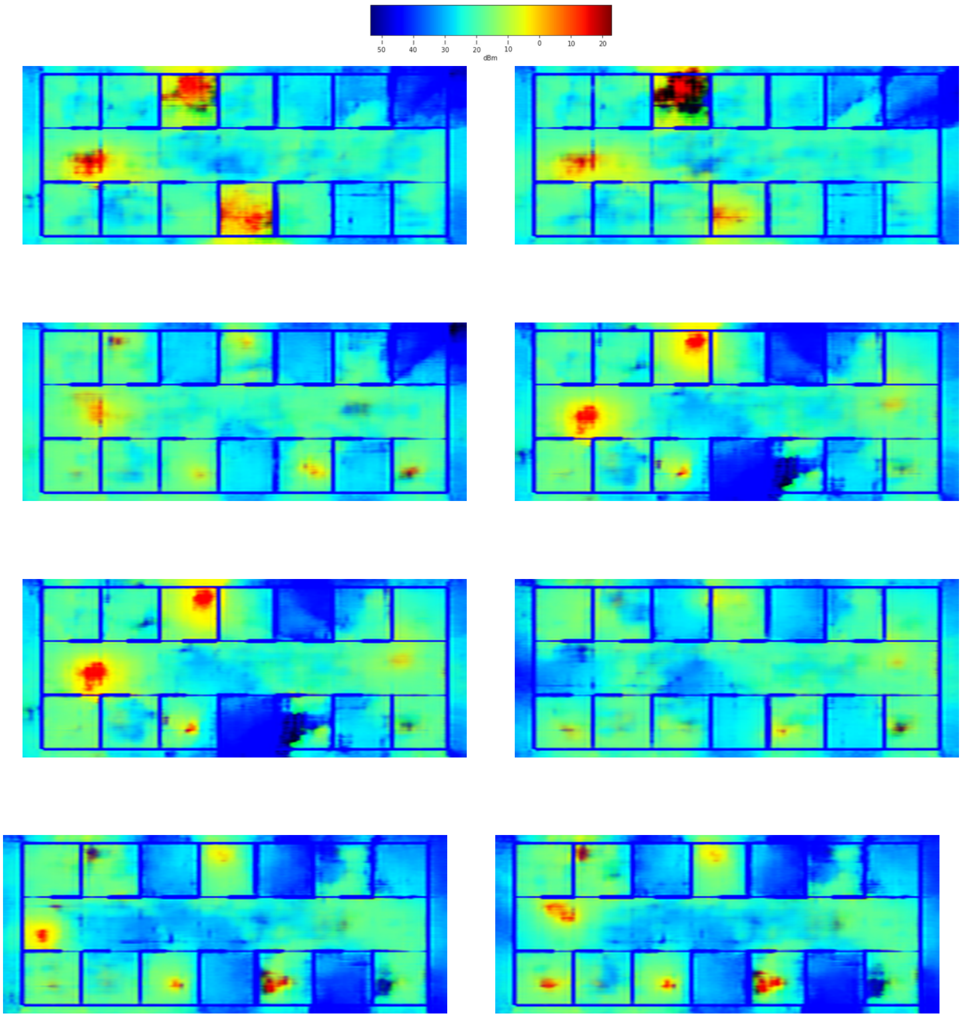

Figure A.1: RF-EMF exposure reference map images with different Wi-Fi access points locations while 30 sensors are in input images

Number of sensors: 60

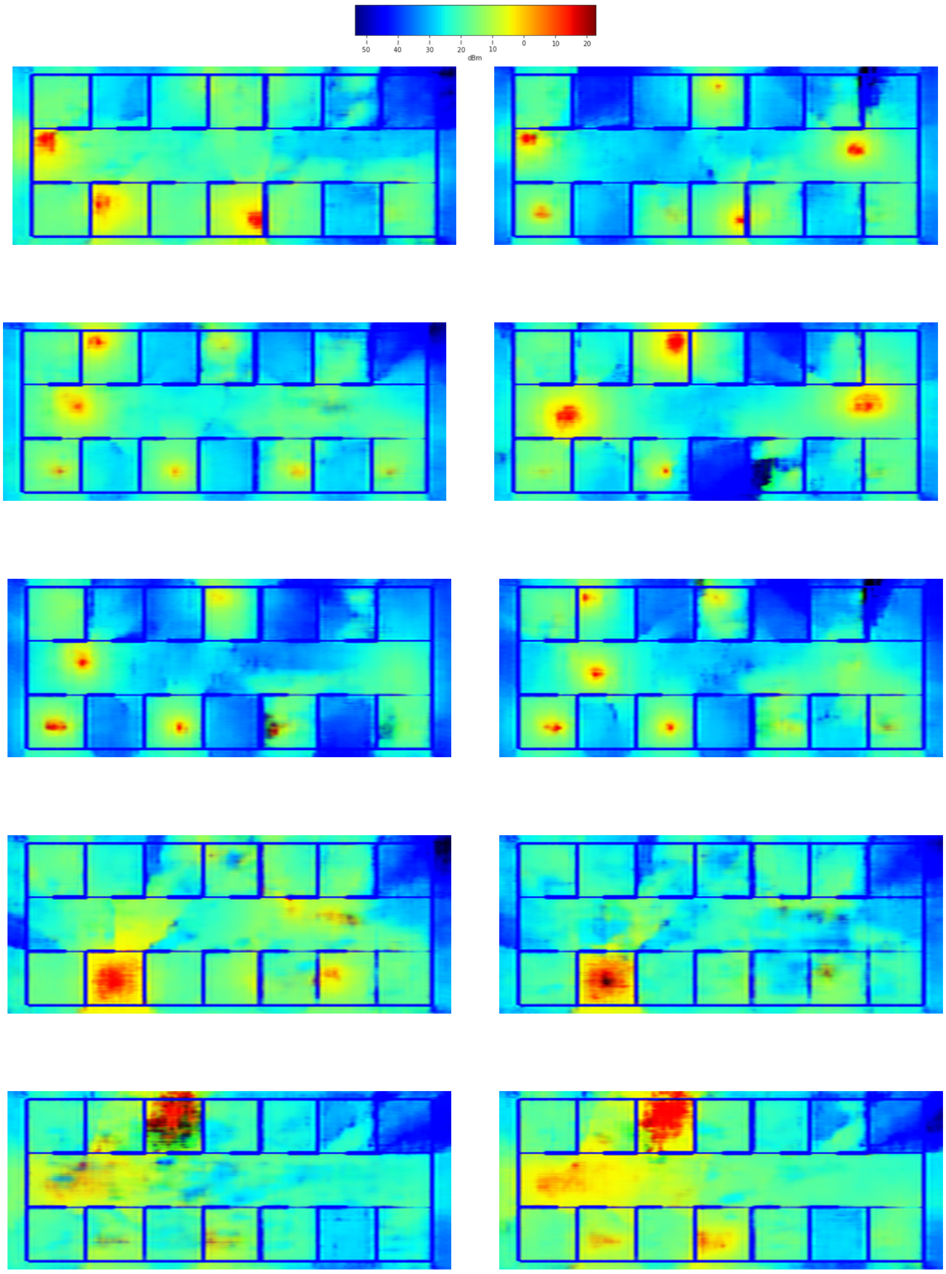

Figure A.2: RF-EMF exposure reference map images with different Wi-Fi access points locations while 60 sensors are in input images

A.2 EME-Net

We present the results of EME-Net, Unet based architecture, when a different number of sensors is used in the scenario in Figure A.3.

Number of sensors: 96

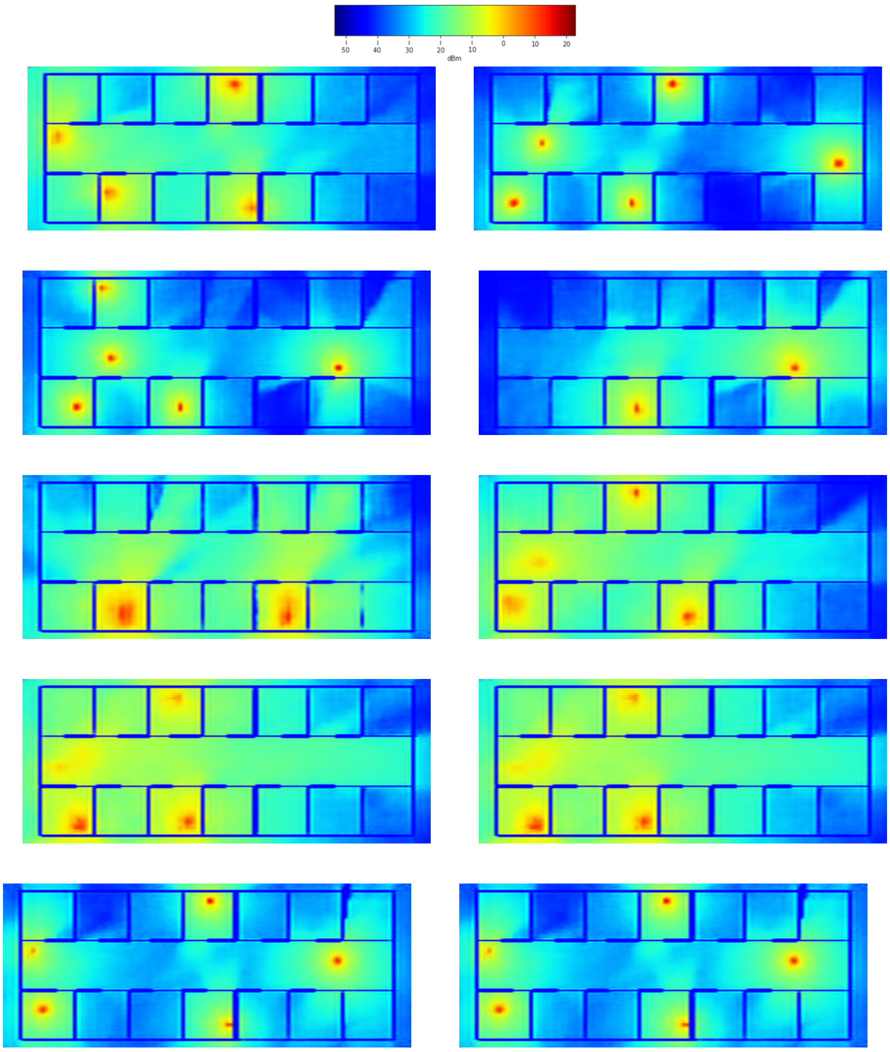

Figure A.3: RF-EMF exposure reference map images with different Wi-Fi access points locations while 96 sensors are in input images

Appendix B

Appendix related to inference on Outdoor Environment

B.1 EMGAN

We present the results of EMGAN when a 50 sensors are used in the scenario in Figure B.1.

number of sensor 50

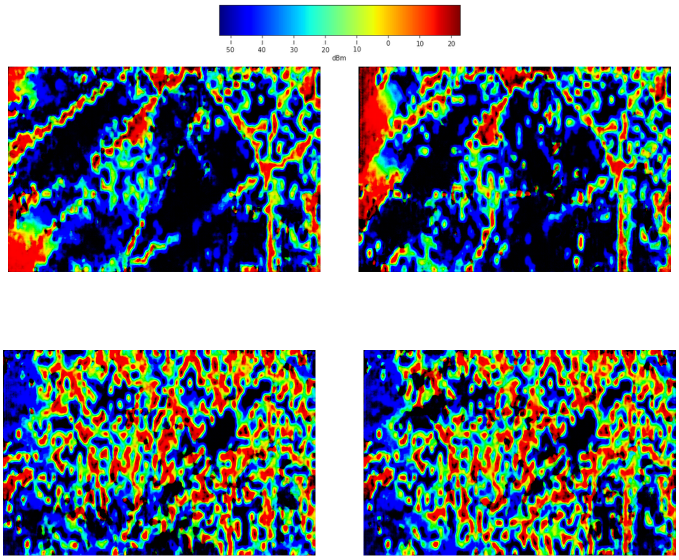

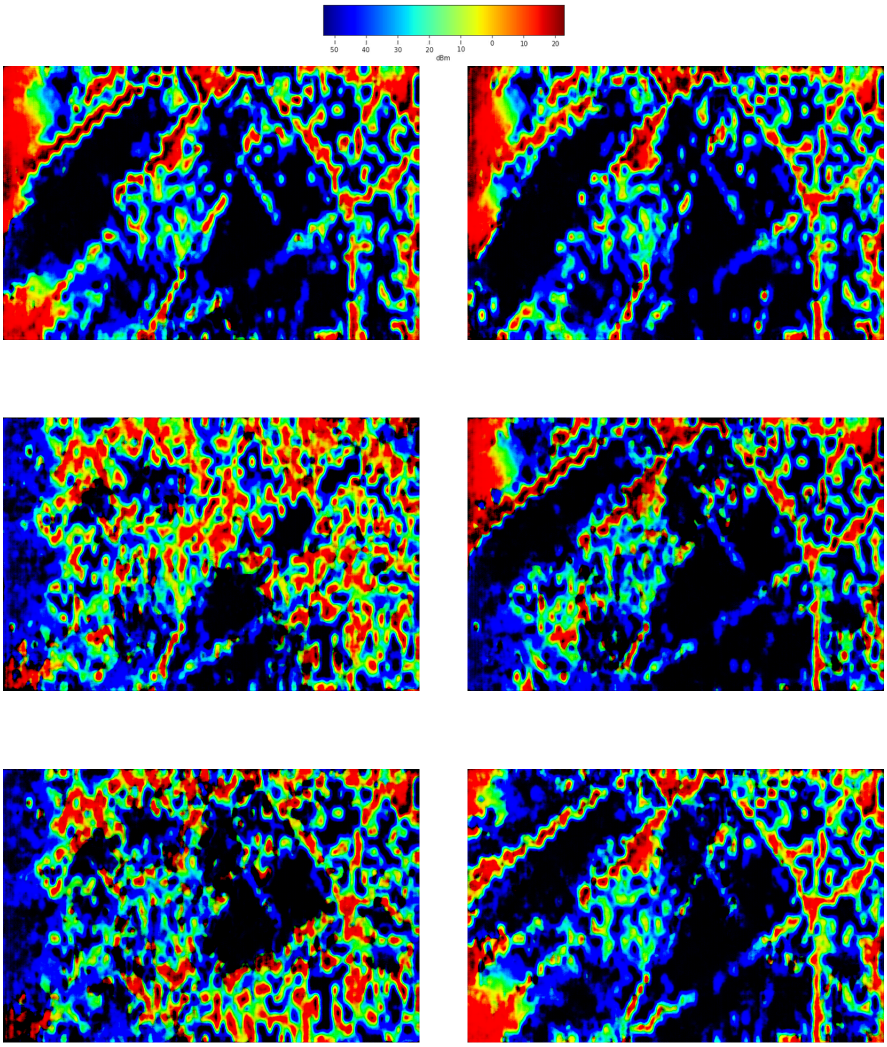

Figure B.1: RF-EMF exposure reference map images with different position of the transmitter locations in the outdoor scenario while 60 sensors are in input images

B.2 EME-CNTK

We present the few reconstruction, failed included of EME-CNTK, when a different number of sensors is used in the scenario in Figure B.2.

Varying number of sensors

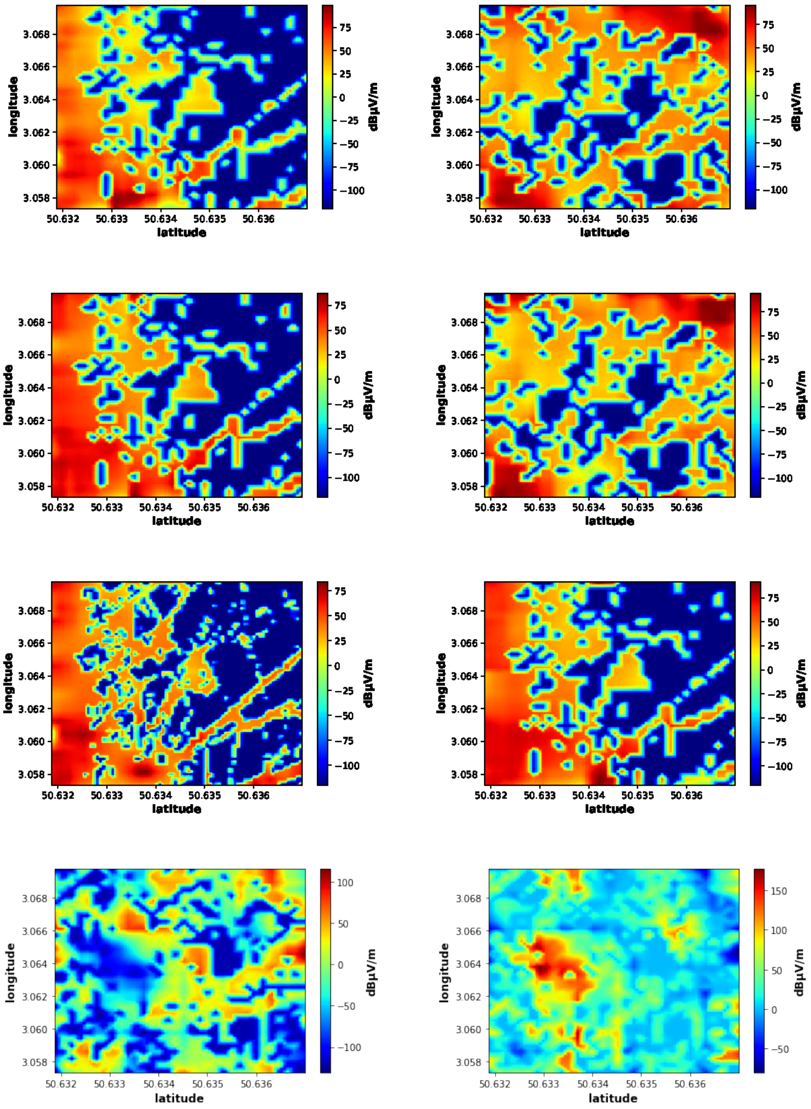

Figure B.2: RF-EMF exposure maps reconstructed with different positions of the transmitters while varying number of sensors in input images

B.3 Reference images

Python is used to convert the veneris data into images (RGB or grayscale) as illustrated in Figure B.3 and B.4.

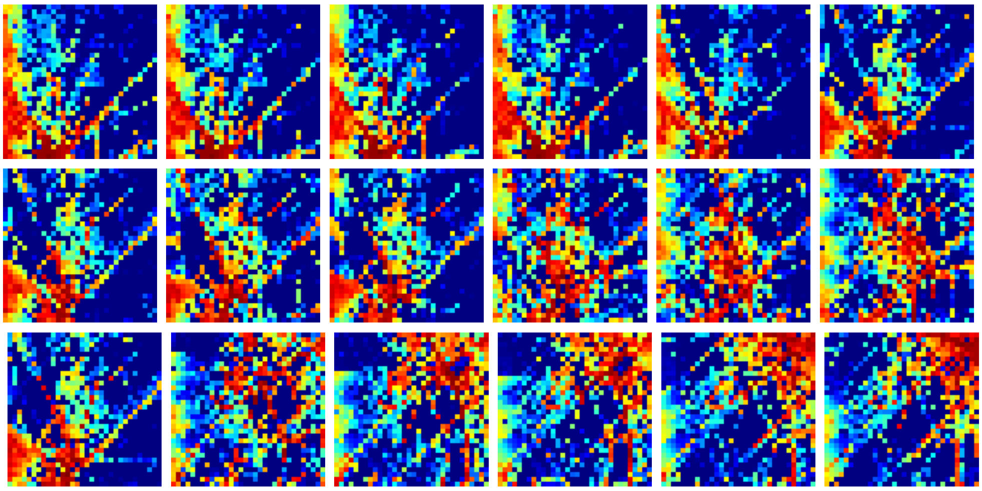

Figure B.3: RF-EMF exposure ground truth images (RGB) with different positions of the transmitters

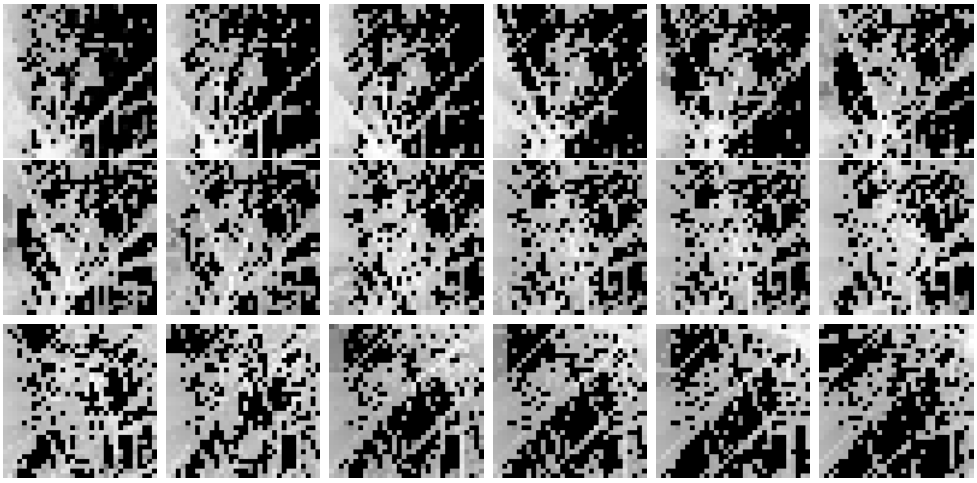

Figure B.4: RF-EMF exposure ground truth grayscale images with different positions of the transmitters grayscale

Bibliography

[1] Adam, M, Rebholz, CE, et al. “The Swiss Childhood Cancer Registry: rationale, organisation and results for the years 2001-2005”. In: *Swiss medical weekly* 137.3536 (2007), pp. 502–509.

[2] Aerts, Sam et al. “Assessment of outdoor radiofrequency electromagnetic field exposure through hotspot localization using kriging-based sequential sampling”. In: *Environmental research* 126 (2013), pp. 184–191.

[3] Aerts, Sam et al. “Use of artificial intelligence to model exposure to radiofrequency electromagnetic fields based on sensor network measurements”. In: *4th Workshop on Uncertainty Modeling for Engineering Applications (UMEMA 2018).* 2018.

[4] Agarwal, Anirudh and Gangopadhyay, Ranjan. “Predictive spectrum occupancy probability-based spatio-temporal dynamic channel allocation map for future cognitive wireless networks”. In: *Transactions on Emerging Telecommunications Technologies* 29.8 (2018), e3442.

[5] Ahlbom, Anders. “Guidelines for limiting exposure to time-varying electric, magnetic, and electromagnetic fields (up to 300 GHz). International Commission on Non-Ionizing Radiation Protection.” In: *Health physics* 74 4 (1998), pp. 494–522.

[6] Ahlbom, Anders et al. “Epidemiologic evidence on mobile phones and tumor risk: a review”. In: *Epidemiology* (2009), pp. 639–652.

[7] Ainsworth, Samuel K, Foti, Nicholas J, and Fox, Emily B. “Disentangled VAE representations for multi-aspect and missing data”. In: arXiv preprint arXiv:1806.09060 (2018).

[8] Alaya-Feki, Afef Ben Hadj et al. “Informed spectrum usage in cognitive radio networks: Interference cartography”. In: *2008 IEEE 19th International Symposium on Personal, Indoor and Mobile Radio Communications.* IEEE. 2008, pp. 1–5.

[9] Amiot, Nicolas, Laaraiedh, Mohamed, and Uguen, Bernard. “PyLayers: An open source dynamic simulator for indoor propagation and localization”. In: *2013 IEEE International Conference on Communications Workshops (ICC).* IEEE. 2013, pp. 84–88.

[10] Andersen, J.B., Rappaport, T.S., and Yoshida, S. “Propagation measurements and models for wireless communications channels”. In: *IEEE Communications Magazine* 33.1 (1995), pp. 42–49. DOI: `10.1109/35.339880`.

[11] Arora, Sanjeev et al. “Implicit regularization in deep matrix factorization”. In: *Advances in Neural Information Processing Systems* 32 (2019).

[12] Arora, Sanjeev et al. “On exact computation with an infinitely wide neural net”. In: *Thirty-third Conference on Neural Information Processing Systems.* 2019.

[13] Augner, Christoph et al. “Acute effects of electromagnetic fields emitted by GSM mobile phones on subjective well-being and physiological reactions: A meta-analysis”. In: vol. 424. Mar. 2012, pp. 11–5. DOI: `10.1016/j.scitotenv.2012.02.034`.

[14] Aydin, Denis et al. “Mobile phone use and brain tumors in children and adolescents: a multicenter case-control study”. In: *Journal of the National Cancer Institute* 103.16 (2011), pp. 1264–1276.

[15] Baan, Robert et al. “Carcinogenicity of radiofrequency electromagnetic fields”. In: *The lancet oncology* 12.7 (2011), pp. 624–626.

[16] Bakcan, M Rafet et al. “Measurement and Prediction of Electromagnetic Radiation Exposure Level in a University Campus”. In: *Tehnički vjesnik* 29.2 (2022), pp. 449–455.

[17] Balanis, Constantine A. *Advanced engineering electromagnetics.* John Wiley & Sons, 2012.

[18] Bamler, Robert and Mandt, Stephan. “Structured black box variational inference for latent time series models”. In: *arXiv preprint arXiv:1707.01069* (2017).

[19] Bartlett, Peter L and Mendelson, Shahar. “Rademacher and Gaussian complexities: Risk bounds and structural results”. In: *Journal of Machine Learning Research* 3.Nov (2002), pp. 463–482.

[20] Bazerque, Juan Andres and Giannakis, Georgios B. “Nonparametric basis pursuit via sparse kernel-based learning: A unifying view with advances in blind methods”. In: *IEEE Signal Processing Magazine* 30.4 (2013), pp. 112–125.

[21] Belkin, Mikhail et al. “Reconciling modern machine-learning practice and the classical bias–variance trade-off”. In: *Proceedings of the National Academy of Sciences* 116.32 (2019), pp. 15849–15854.

[22] Bertalmio, Marcelo et al. “Image Inpainting”. In: *Proceedings of the 27th Annual Conference on Computer Graphics and Interactive Techniques.* SIGGRAPH ’00. USA: ACM Press/Addison-Wesley Publishing Co., 2000, pp. 417–424. ISBN: 1581132085. DOI: `10.1145/344779.344972`. URL: `https://doi.org/10.1145/344779.344972`.

[23] Boccolini, Gabriele, Hernandez-Penaloza, Gustavo, and Beferull-Lozano, Baltasar. “Wireless sensor network for spectrum cartography based on kriging interpolation”. In: *2012 IEEE 23rd International Symposium on Personal, Indoor and Mobile Radio Communications-(PIMRC).* IEEE. 2012, pp. 1565–1570.

[24] Böhler, Eva and Schüz, Joachim. “Cellular telephone use among primary school children in Germany”. In: *European journal of epidemiology* (2004), pp. 1043–1050.

[25] Bracale, Daniele et al. “Infinite-channel deep stable convolutional neural networks”. In: *arXiv preprint arXiv:2102.03739* (2021).

[26] Bradbury, James et al. *JAX: composable transformations of Python+NumPy programs.* Version 0.3.13. 2018. URL: `http://github.com/google/jax`.

[27] Bulut, Eyuphan and Guevenc, Ismail. “Trajectory optimization for cellular-connected UAVs with disconnectivity constraint”. In: *2018 IEEE International Conference on Communications Workshops (ICC Workshops).* IEEE. 2018, pp. 1–6.

[28] Candès, Emmanuel J and Tao, Terence. “The power of convex relaxation: Near-optimal matrix completion”. In: *IEEE Transactions on Information Theory* 56.5 (2010), pp. 2053–2080.

[29] Casale, Francesco Paolo et al. “Gaussian process prior variational autoencoders”. In: *Advances in neural information processing systems* 31 (2018).

[30] Cheng, Zezhou et al. “A bayesian perspective on the deep image prior”. In: *Proceedings of the IEEE/CVF Conference on Computer Vision and Pattern Recognition.* 2019, pp. 5443–5451.

[31] Chikha, Wassim Ben, Wang, Shanshan, and Wiart, Joe. “An Extrapolation Approach for RF-EMF Exposure Prediction in an Urban Area using Artificial Neural Network”. In: *IEEE Access* (2023).

[32] Choi, Chang-Sik and Baccelli, François. “A Stochastic Geometry Model for Spatially Correlated Blockage in Vehicular Networks”. In: *IEEE Internet of Things Journal* 9.20 (2022), pp. 19881–19889.

[33] Choi, Wongeun et al. “Low-Power LoRa signal-based outdoor positioning using fingerprint Algorithm”. In: *ISPRS International Journal of Geo-Information* 7.11 (2018), p. 440.

[34] Chouvardas, Symeon et al. “A method to reconstruct coverage loss maps based on matrix completion and adaptive sampling”. In: *2016 IEEE International Conference on Acoustics, Speech and Signal Processing (ICASSP).* IEEE. 2016, pp. 6390–6394.

[35] Christopher, EO, Dhillon, Harpreet S, and Buehrer, R Michael. “A statistical characterization of localization performance in wireless networks”. In: *IEEE Transactions on Wireless Communications* 17.9 (2018), pp. 5841–5856.

[36] Chu, Lei, Pan, Hao, and Wang, Wenping. “Unsupervised Shape Completion via Deep Prior in the Neural Tangent Kernel Perspective”. In: *ACM Trans. Graph.* 40.3 (July 2021). ISSN: 0730-0301. DOI: `10.1145/3459234`. URL: `https://doi.org/10.1145/3459234`.

[37] CLAVIER, Laurent. “Modèles physiques et perception, contributions à l’analyse du milieu sonore”. PhD thesis. UNIVERSITÉ DE BRETAGNE OCCIDENTALE, 1996.

[38] Council, The Swiss Federal. *Ordinance relating to Protection from Non-Ionising Radiation (ONIR).* Dec. 1999.

[39] Cozman, Fabio Gagliardi, Cohen, Ira, and Cirelo, M. “Unlabeled Data Can Degrade Classification Performance of Generative Classifiers.” In: *Flairs conference.* 2002, pp. 327–331.

[40] Dalca, Adrian V et al. “Unsupervised learning of probabilistic diffeomorphic registration for images and surfaces”. In: *Medical image analysis* 57 (2019), pp. 226–236.

[41] Damelin, Steven B and Hoang, NS. “On surface completion and image inpainting by biharmonic functions: Numerical aspects”. In: *International Journal of Mathematics and Mathematical Sciences* 2018 (2018), pp. 1–8.

[42] Daniely, Amit, Frostig, Roy, and Singer, Yoram. “Toward deeper understanding of neural networks: The power of initialization and a dual view on expressivity”. In: *Advances in neural information processing systems* 29 (2016).

[43] De Vocht, Frank, Burstyn, Igor, and Cherrie, John W. “Time trends (1998–2007) in brain cancer incidence rates in relation to mobile phone use in England”. In: *Bioelectromagnetics* 32.5 (2011), pp. 334–339.

[44] Diederik, P Kingma, Welling, Max, et al. “Auto-encoding variational bayes”. In: *Proceedings of the International Conference on Learning Representations (ICLR).* Vol. 1. 2014.

[45] Ding, Guoru et al. “Cellular-base-station-assisted device-to-device communications in TV white space”. In: *IEEE Journal on Selected Areas in Communications* 34.1 (2015), pp. 107–121.

[46] Do, Tien Huu et al. “Matrix completion with variational graph autoencoders: Application in hyperlocal air quality inference”. In: *ICASSP 2019-2019 IEEE International Conference on Acoustics, Speech and Signal Processing (ICASSP).* IEEE. 2019, pp. 7535–7539.

[47] Domke, Justin. “Statistical Machine Learning: Kernel Methods and SVMs”. In: *URL: http://phd. gccis. rit. edu/justindomke/courses/SML/(visited on 06/07/2019)* (2012).

[48] Dong, Chao et al. “Image Super-Resolution Using Deep Convolutional Networks”. In: *IEEE Transactions on Pattern Analysis and Machine Intelligence* 38 (2014), pp. 295–307.

[49] Egea-Lopez, Esteban et al. “Vehicular networks simulation with realistic physics”. In: *IEEE Access* 7 (2019), pp. 44021–44036.

[50] Falkenberg, Robert et al. “Machine learning based uplink transmission power prediction for LTE and upcoming 5G networks using passive downlink indicators”. In: *2018 IEEE 88th Vehicular Technology Conference (VTC-Fall).* IEEE. 2018, pp. 1–7.

[51] Fan, Jicong, Zhang, Yuqian, and Udell, Madeleine. “Polynomial matrix completion for missing data imputation and transductive learning”. In: *Proceedings of the AAAI Conference on Artificial Intelligence.* Vol. 34. 04. 2020, pp. 3842–3849.

[52] Fan, Xiaochen et al. “Towards system implementation and data analysis for crowdsensing based outdoor RSS maps”. In: *IEEE Access* 6 (2018), pp. 47535–47545.

[53] Fischhoff, Baruch et al. “How safe is safe enough? A psychometric study of attitudes towards technological risks and benefits”. In: *Policy sciences* 9 (1978), pp. 127–152.

[54] Forsk, Atoll. “Radio Planning & Optimisation Software”. In: *Technical Reference Guide., Blagnac-France: Copyright by Forsk* (2011).

[55] Fortuin, Vincent et al. “GP-VAE: Deep probabilistic time series imputation”. In: *International conference on artificial intelligence and statistics.* PMLR. 2020, pp. 1651–1661.

[56] Freeman, W.T., Jones, T.R., and Pasztor, E.C. “Example-based super-resolution”. In: *IEEE Computer Graphics and Applications* 22.2 (2002), pp. 56–65. DOI: `10.1109/38.988747`.

[57] Frei, Patrizia et al. “A prediction model for personal radio frequency electromagnetic field exposure”. In: *Science of the total environment* 408.1 (2009), pp. 102–108.

[58] Gaillot, Davy Paul. “Optical properties of complex periodic media structurally modified by atomic layer deposition”. In: *Ph. D. Thesis* (2007).

[59] Gontier, Quentin et al. “A stochastic geometry approach to EMF exposure modeling”. In: *IEEE access* 9 (2021), pp. 91777–91787.

[60] Gontier, Quentin et al. “Semi-empirical Model of Global Exposure using Stochastic Geometry”. In: *2021 IEEE International Conference on Communications Workshops (ICC Workshops).* IEEE. 2021, pp. 1–5.

[61] Gontier, Quentin et al. “Stochastic Geometry Modeling of EMF exposure due to Cellular Networks in Urban Environments”. In: *Proc. of the 1st Post-IRACON Meeting (COST).* 2020.

[62] Goodfellow, Ian et al. “Generative adversarial nets”. In: *Advances in neural information processing systems* 27 (2014).

[63] Group, INTERPHONE Study. “Brain tumour risk in relation to mobile telephone use: results of the INTERPHONE international case-control study”. In: *International journal of epidemiology* 39.3 (2010), pp. 675–694.

[64] Haas, John K. “A history of the unity game engine”. In: (2014).

[65] Hamid, Mohamed and Beferull-Lozano, Baltasar. “Non-parametric spectrum cartography using adaptive radial basis functions”. In: *2017 IEEE International Conference on Acoustics, Speech and Signal Processing (ICASSP)*. IEEE. 2017, pp. 3599–3603.

[66] Han, Xu et al. “A Power Spectrum Maps Estimation Algorithm Based on Generative Adversarial Networks for Underlay Cognitive Radio Networks”. In: *Sensors* 20.1 (2020). ISSN: 1424-8220. DOI: `10.3390/s20010311`. URL: `https://www.mdpi.com/1424-8220/20/1/311`.

[67] Han, Zhifeng et al. “Radio environment map construction by kriging algorithm based on mobile crowd sensing”. In: *Wireless Communications and Mobile Computing* 2019 (2019).

[68] Harris, Charles R. et al. “Array programming with NumPy”. In: *Nature* 585.7825 (Sept. 2020), pp. 357–362. DOI: `10.1038/s41586-020-2649-2`. URL: `https://doi.org/10.1038/s41586-020-2649-2`.

[69] Hayashi, Takahiro, Nagao, Tatsuya, and Ito, Satoshi. “A study on the variety and size of input data for radio propagation prediction using a deep neural network”. In: *2020 14th European Conference on Antennas and Propagation (EuCAP)*. IEEE. 2020, pp. 1–5.

[70] He, Kaiming et al. “Deep residual learning for image recognition”. In: *Proceedings of the IEEE conference on computer vision and pattern recognition*. 2016, pp. 770–778.

[71] Heaton, Jeff. “Ian Goodfellow, Yoshua Bengio, and Aaron Courville: Deep learning: The MIT Press, 2016, 800 pp, ISBN: 0262035618”. In: *Genetic Programming and Evolvable Machines* 19.1-2 (2018), pp. 305–307.

[72] Hinrichs, Hermann, Heinze, Hans-Jochen, and Rotte, Michael. “Human sleep under the influence of a GSM 1800 electromagnetic far field”. In: *Somnologie* 9.4 (2005), pp. 185–191.

[73] Hodos, Rachel et al. “Cell-specific prediction and application of drug-induced gene expression profiles”. In: *PACIFIC SYMPOSIUM ON BIOCOMPUTING 2018: Proceedings of the Pacific Symposium.* World Scientific. 2018, pp. 32–43.

[74] Hu, Yongli et al. “Efficient radio map construction based on low-rank approximation for indoor positioning”. In: *Mathematical Problems in Engineering* 2013 (2013).

[75] Huang, Din-Hwa et al. “Cooperative radio source positioning and power map reconstruction: A sparse Bayesian learning approach”. In: *IEEE Transactions on Vehicular Technology* 64.6 (2014), pp. 2318–2332.

[76] Hug, K and Röösli, M. “Electromagnetic hypersensitivityät: evaluation of scientific studies: status at the end of 2011”. In: (2012).

[77] “IEEE Standard for Safety Levels with Respect to Human Exposure to Electric, Magnetic, and Electromagnetic Fields, 0 Hz to 300 GHz - Redline”. In: *IEEE Std C95.1-2019 (Revision of IEEE Std C95.1-2005/ Incorporates IEEE Std C95.1-2019/Cor 1-2019) - Redline* (2019), pp. 1–679.

[78] IEEE Standards Coordinating Committee, 28 et al. “IEEE standard for safety levels with respect to human exposure to radio frequency electromagnetic fields, 3kHz to 300GHz”. In: *IEEE C95. 1-1991* (1992).

[79] Imai, T, Kitao, K, and Inomata, M. “Radio propagation prediction model using convolutional neural networks by deep learning”. In: *2019 13th European Conference on Antennas and Propagation (EuCAP).* IEEE. 2019, pp. 1–5.

[80] Inoue, Kazuya et al. “Radio propagation prediction using deep neural network and building occupancy estimation”. In: *IEICE Communications Express* 9.10 (2020), pp. 506–511.

[81] Inskip, Peter D, Hoover, Robert N, and Devesa, Susan S. “Brain cancer incidence trends in relation to cellular telephone use in the United States”. In: *Neuro-oncology* 12.11 (2010), pp. 1147–1151.

[82] Isola, Phillip et al. “Image-to-image translation with conditional adversarial networks”. In: *Proceedings of the IEEE conference on computer vision and pattern recognition.* 2017, pp. 1125–1134.

[83] Jacot, Arthur, Gabriel, Franck, and Hongler, Clément. “Neural tangent kernel: Convergence and generalization in neural networks”. In: *Advances in neural information processing systems* 31 (2018).

[84] Jähnichen, Patrick et al. "Scalable generalized dynamic topic models". In: *International Conference on Artificial Intelligence and Statistics*. PMLR. 2018, pp. 1427–1435.

[85] Jain, Nitin. "Joint link learning and cognitive radio sensing." In: (2012).

[86] Jayawickrama, Beeshanga Abewardana et al. "Improved performance of spectrum cartography based on compressive sensing in cognitive radio networks". In: *2013 IEEE International Conference on Communications (ICC)*. IEEE. 2013, pp. 5657–5661.

[87] Joseph, Wout et al. "Comparison of personal radio frequency electromagnetic field exposure in different urban areas across Europe". In: *Environmental research* 110.7 (2010), pp. 658–663.

[88] Kacou, Marc et al. "A multi-wall and multi-frequency home environment path loss characterization and modeling". In: *12th European Conference on Antennas and Propagation (EuCAP 2018)*. 2018, pp. 1–5. DOI: `10.1049/cp.2018.0464`.

[89] Kaplan, Jared et al. "Scaling laws for neural language models". In: *arXiv preprint arXiv:2001.08361* (2020).

[90] Kay, Steven M. *Fundamentals of statistical signal processing: estimation theory*. Prentice-Hall, Inc., 1993.

[91] Kim, Jiwon, Lee, Jung Kwon, and Lee, Kyoung Mu. "Accurate Image Super-Resolution Using Very Deep Convolutional Networks". In: *CoRR* abs/1511.04587 (2015). arXiv: `1511.04587`. URL: `http://arxiv.org/abs/1511.04587`.

[92] Kim, Seung-Jun and Giannakis, Georgios B. "Cognitive radio spectrum prediction using dictionary learning". In: *2013 IEEE Global Communications Conference (GLOBECOM)*. IEEE. 2013, pp. 3206–3211.

[93] Kimeldorf, George S and Wahba, Grace. "A correspondence between Bayesian estimation on stochastic processes and smoothing by splines". In: *The Annals of Mathematical Statistics* 41.2 (1970), pp. 495–502.

[94] Kubota, Ryosuke et al. "Efficient survey database construction using location fingerprinting interpolation". In: *2013 IEEE 27th international conference on advanced information networking and applications (AINA)*. IEEE. 2013, pp. 469–476.

[95] Lauer, Oliver et al. “Combining near-and far-field exposure for an organ-specific and whole-body RF-EMF proxy for epidemiological research: a reference case”. In: *Bioelectromagnetics* 34.5 (2013), pp. 366–374.

[96] LeCun, Yann et al. “Gradient-based learning applied to document recognition”. In: *Proceedings of the IEEE* 86.11 (1998), pp. 2278–2324.

[97] Lee, Jaehoon et al. “Deep neural networks as gaussian processes”. In: *arXiv preprint arXiv:1711.00165* (2017).

[98] Lee, Jaehoon et al. “Finite versus infinite neural networks: an empirical study”. In: *Advances in Neural Information Processing Systems* 33 (2020), pp. 15156–15172.

[99] Levy, Barry S et al. “Occupational and environmental healh: Twenty-first century challenges and opportunities”. In: *Occupational and environmental health: Recognizing and preventing disease and injury* (2011), 3À22.

[100] Li, Steven Cheng-Xian, Jiang, Bo, and Marlin, Benjamin. “MISGAN: Learning from incomplete data with generative adversarial networks”. In: *arXiv preprint arXiv:1902.09599* (2019).

[101] Li, Zhemin et al. “A regularised deep matrix factorised model of matrix completion for image restoration”. In: *IET Image Processing* 16.12 (2022), pp. 3212–3224.

[102] Li, Zhiyuan et al. “Enhanced convolutional neural tangent kernels”. In: *arXiv preprint arXiv:1911.00809* (2019).

[103] Li, Zhuo et al. “Sparsely Self-Supervised Generative Adversarial Nets for Radio Frequency Estimation”. In: *IEEE Journal on Selected Areas in Communications* 37.11 (2019), pp. 2428–2442. DOI: `10.1109/JSAC.2019.2933779`.

[104] Lin, Yuxiang et al. “Sateloc: A virtual fingerprinting approach to outdoor lora localization using satellite images”. In: *ACM Transactions on Sensor Networks (TOSN)* 17.4 (2021), pp. 1–28.

[105] Liu, Chaoyue, Zhu, Libin, and Belkin, Mikhail. “Toward a theory of optimization for over-parameterized systems of non-linear equations: the lessons of deep learning”. In: *arXiv preprint arXiv:2003.00307* 7 (2020).

[106] Liu, Chaoyue, Zhu, Libin, and Belkin, Misha. “On the linearity of large non-linear models: when and why the tangent kernel is constant”. In: *Advances in Neural Information Processing Systems* 33 (2020), pp. 15954–15964.

[107] Liu, Ji et al. "Tensor completion for estimating missing values in visual data". In: *IEEE transactions on pattern analysis and machine intelligence* 35.1 (2012), pp. 208–220.

[108] Ma, Chao et al. "Eddi: Efficient dynamic discovery of high-value information with partial vae". In: *arXiv preprint arXiv:1809.11142* (2018).

[109] MacCartney, George R. et al. "Path loss models for 5G millimeter wave propagation channels in urban microcells". In: *2013 IEEE Global Communications Conference (GLOBECOM)*. 2013, pp. 3948–3953. DOI: `10.1109/GLOCOM.2013.6831690`.

[110] Malkova, Aleksandra et al. "Self-learning for received signal strength map reconstruction with neural architecture search". In: *Artificial Neural Networks and Machine Learning–ICANN 2021: 30th International Conference on Artificial Neural Networks, Bratislava, Slovakia, September 14–17, 2021, Proceedings, Part V 30*. Springer. 2021, pp. 515–526.

[111] Mallik, Mohammed et al. "EME-GAN: A Conditional Generative Adversarial Network based Indoor EMF Exposure Map Reconstruction". In: *29Â° Colloque sur le traitement du signal et des images*. 2023-1258. Grenoble: GRETSI - Groupe de Recherche en Traitement du Signal et des Images, 2023, p. 745–748.

[112] Mallik, Mohammed et al. "EME-Net: A U-net-based Indoor EMF Exposure Map Reconstruction Method". In: *2022 16th European Conference on Antennas and Propagation (EuCAP)*. IEEE. 2022, pp. 1–5.

[113] Mallik, Mohammed et al. "Towards Outdoor Electromagnetic Field Exposure Mapping Generation Using Conditional GANs". In: *Sensors* 22.24 (2022), p. 9643.

[114] Martín Abadi et al. *TensorFlow: Large-Scale Machine Learning on Heterogeneous Systems*. Software available from tensorflow.org. 2015. URL: `https://www.tensorflow.org/`.

[115] Martínez-González, A et al. "Minimization of measuring points for the electric field exposure map generation in indoor environments by means of Kriging interpolation and selective sampling". In: *Environmental Research* 212 (2022), p. 113577.

[116] Mathar, Rudolf and Mattfeldt, Jürgen. “On the distribution of cumulated interference power in Rayleigh fading channels”. In: *Wireless Networks* 1.1 (1995), pp. 31–36.

[117] Matheron, Georges. “Principles of geostatistics”. In: *Economic geology* 58.8 (1963), pp. 1246–1266.

[118] Matthews, Alexander G de G et al. “Gaussian process behaviour in wide deep neural networks”. In: *arXiv preprint arXiv:1804.11271* (2018).

[119] Mazar, Haim. “Electro Magnetic Fields: Limitations to Radio Frequency Human Exposure; revised Chapter 9”. In: Jan. 2021.

[120] Mazloum, Taghrid et al. “Artificial Neural Network-Based Uplink Power Prediction From Multi-Floor Indoor Measurement Campaigns in 4G Networks”. In: *Frontiers in Public Health* 9 (2021), p. 777798.

[121] Mei, Song and Montanari, Andrea. “The generalization error of random features regression: Precise asymptotics and the double descent curve”. In: *Communications on Pure and Applied Mathematics* 75.4 (2022), pp. 667–766.

[122] Meinilä, J et al. “IST-2003-507581 WINNER D5. 2 Determination of Propagation Scenarios”. In: ().

[123] Mercer, James. “Xvi. functions of positive and negative type, and their connection the theory of integral equations”. In: *Philosophical transactions of the royal society of London. Series A, containing papers of a mathematical or physical character* 209.441-458 (1909), pp. 415–446.

[124] Mirza, Mehdi and Osindero, Simon. “Conditional generative adversarial nets”. In: *arXiv preprint arXiv:1411.1784* (2014).

[125] Mohler, Evelyn et al. “Effects of everyday radiofrequency electromagnetic-field exposure on sleep quality: a cross-sectional study”. In: *Radiation Research* 174.3 (2010), pp. 347–356.

[126] Moulder, JE et al. “Mobile phones, mobile phone base stations and cancer: a review”. In: *International journal of radiation biology* 81.3 (2005), pp. 189–203.

[127] Nagao, Tatsuya and Hayashi, Takahiro. “Study on radio propagation prediction by machine learning using urban structure maps”. In: *2020 14th European Conference on Antennas and Propagation (EuCAP)*. IEEE. 2020, pp. 1–5.

[128] Nakkiran, Preetum et al. "Deep double descent: Where bigger models and more data hurt". In: *Journal of Statistical Mechanics: Theory and Experiment* 2021.12 (2021), p. 124003.

[129] Nazabal, Alfredo et al. "Handling incomplete heterogeneous data using vaes". In: *Pattern Recognition* 107 (2020), p. 107501.

[130] Neal, Radford M. *Bayesian learning for neural networks.* Vol. 118. Springer Science & Business Media, 2012.

[131] Ning, Chao, Li, Rui, and Li, Kejiong. "Outdoor location estimation using received signal strength-based fingerprinting". In: *Wireless Personal Communications* 89 (2016), pp. 365–384.

[132] Non-Ionizing Radiation Protection, International Commission on et al. "Guidelines for limiting exposure to electromagnetic fields (100 kHz to 300 GHz)". In: *Health physics* 118.5 (2020), pp. 483–524.

[133] Novak, Roman et al. *Neural Tangents: Fast and Easy Infinite Neural Networks in Python.* 2019. arXiv: `1912.02803 [stat.ML]`.

[134] OpenStreetMap contributors. *Planet dump retrieved from https://planet.osm.org.* `https://www.openstreetmap.org`. 2017.

[135] Organization, World Health. *Establishing a dialogue on risks from electromagnetic fields.* 2002.

[136] Parker, Steven G et al. "Optix: a general purpose ray tracing engine". In: *Acm transactions on graphics (tog)* 29.4 (2010), pp. 1–13.

[137] *Peak Signal-to-noise Ratio.* URL: `https://en.wikipedia.org/wiki/Peak_signal-to-noise_ratio`.

[138] Pedersen, Alma B et al. "Missing data and multiple imputation in clinical epidemiological research". In: *Clinical epidemiology* (2017), pp. 157–166.

[139] Peek, Markus and Tsourdi, Evangelia Lilian. "Directive 2013/33/EU of the European Parliament and of the Council of 26 June 2013 laying Down Standards for the Reception of Applicants for International Protection". In: *EU Immigration and Asylum Law Commentary.* CH Beck/Hart/Nomos, 2016, pp. 1381–1477.

[140] Piersanti, Stefano, Annoni, Luca Alfredo, and Cassioli, Dajana. “Millimeter waves channel measurements and path loss models”. In: *2012 IEEE International Conference on Communications (ICC)*. 2012, pp. 4552–4556. DOI: `10.1109/ICC.2012.6363950`.

[141] Radhakrishnan, Adityanarayanan. *Lecture 3: Kernel Regression*. 2022.

[142] Radhakrishnan, Adityanarayanan et al. “Simple, fast, and flexible framework for matrix completion with infinite width neural networks”. In: *Proceedings of the National Academy of Sciences* 119.16 (2022), e2115064119.

[143] Rasmussen, Carl Edward and Williams, Christopher KI. “Gaussian processes in machine learning”. In: *Lecture notes in computer science* 3176 (2004), pp. 63–71.

[144] Recht, Benjamin, Fazel, Maryam, and Parrilo, Pablo A. “Guaranteed minimum-rank solutions of linear matrix equations via nuclear norm minimization”. In: *SIAM review* 52.3 (2010), pp. 471–501.

[145] Redondi, Alessandro Enrico Cesare. “Radio map interpolation using graph signal processing”. In: *IEEE Communications Letters* 22.1 (2017), pp. 153–156.

[146] Regel, Sabine J et al. “Pulsed radio-frequency electromagnetic fields: dose-dependent effects on sleep, the sleep EEG and cognitive performance”. In: *Journal of sleep research* 16.3 (2007), pp. 253–258.

[147] Repacholi, Michael H et al. “Systematic review of wireless phone use and brain cancer and other head tumors”. In: *Bioelectromagnetics* 33.3 (2012), pp. 187–206.

[148] *RGBA color model*. en. Page Version ID: 1057086643. Nov. 2021. URL: `https://en.wikipedia.org/w/index.php?title=RGBA_color_model&oldid=1057086643` (visited on 09/28/2022).

[149] Rizk, Karim, Wagen, J-F, and Gardiol, Fred. “Two-dimensional ray-tracing modeling for propagation prediction in microcellular environments”. In: *IEEE Transactions on Vehicular Technology* 46.2 (1997), pp. 508–518.

[150] Romero, Daniel et al. “Aerial spectrum surveying: Radio map estimation with autonomous UAVs”. In: *2020 IEEE 30th International Workshop on Machine Learning for Signal Processing (MLSP)*. IEEE. 2020, pp. 1–6.

[151] Ronneberger, Olaf, Fischer, Philipp, and Brox, Thomas. “U-net: Convolutional networks for biomedical image segmentation”. In: *Medical Image Computing and Computer-Assisted Intervention–MICCAI 2015: 18th International Conference, Munich, Germany, October 5-9, 2015, Proceedings, Part III 18.* Springer. 2015, pp. 234–241.

[152] Röösli, Martin and Hug, Kerstin. “Wireless communication fields and nonspecific symptoms of ill health: a literature review”. In: *Wiener Medizinische Wochenschrift* 161.9 (2011), pp. 240–250.

[153] Röösli, Martin et al. “Conduct of a personal radiofrequency electromagnetic field measurement study: proposed study protocol”. In: *Environmental Health* 9.1 (2010), pp. 1–14.

[154] Röösli, Martin et al. “Systematic review on the health effects of exposure to radiofrequency electromagnetic fields from mobile phone base stations”. In: *Bulletin of the World Health Organization* 88 (2010), pp. 887–896.

[155] Rosenblatt, Frank. *Principles of neurodynamics. perceptrons and the theory of brain mechanisms.* Tech. rep. Cornell Aeronautical Lab Inc Buffalo NY, 1961.

[156] Rubin, G James, Nieto-Hernandez, Rosa, and Wessely, Simon. “Idiopathic environmental intolerance attributed to electromagnetic fields (formerly ‘electromagnetic hypersensitivity’): an updated systematic review of provocation studies”. In: *Bioelectromagnetics: Journal of the Bioelectromagnetics Society, The Society for Physical Regulation in Biology and Medicine, The European Bioelectromagnetics Association* 31.1 (2010), pp. 1–11.

[157] Rumelhart, David E, Hinton, Geoffrey E, and Williams, Ronald J. “Learning representations by back-propagating errors”. In: *nature* 323.6088 (1986), pp. 533–536.

[158] Rusu, Cristian and Rusu, Virginia. “Radial basis functions versus geostatistics in spatial interpolations”. In: *Artificial Intelligence in Theory and Practice: IFIP 19th World Computer Congress, TC 12: IFIP AI 2006 Stream, August 21–24, 2006, Santiago, Chile 1.* Springer. 2006, pp. 119–128.

[159] Saito, Kentaro et al. “Two-step path loss prediction by artificial neural network for wireless service area planning”. In: *IEICE Communications Express* (2019).

[160] Schoenberg, Isaac J. “Contributions to the problem of approximation of equidistant data by analytic functions: Part A.—On the problem of smoothing or graduation. A first class of analytic approximation formulae”. In: *Quart. Appl. Math. 4 (1946), 45-99* (1946), pp. 3–57. DOI: `https://doi.org/10.1090/qam/15914`.

[161] Schüz, Joachim and Mann, Simon. “A discussion of potential exposure metrics for use in epidemiological studies on human exposure to radiowaves from mobile phone base stations”. In: *Journal of Exposure Science & Environmental Epidemiology* 10.6 (2000), pp. 600–605.

[162] Shan, Jing et al. “The method of electromagnetic environment map construction based on Kriging spatial interpolation”. In: *2018 International Conference on Information Systems and Computer Aided Education (ICISCAE)*. IEEE. 2018, pp. 212–217.

[163] Shih, Ya et al. “The Association Between Smartphone Use and Breast Cancer Risk Among Taiwanese Women: A Case-Control Study”. In: *Cancer Management and Research* Volume 12 (Oct. 2020), pp. 10799–10807. DOI: `10.2147/CMAR.S267415`.

[164] Solin, Arno et al. “Modeling and interpolation of the ambient magnetic field by Gaussian processes”. In: *IEEE Transactions on robotics* 34.4 (2018), pp. 1112–1127.

[165] Stefanakis, George. “Theory and Applications of Matrix Completion in Genomics Datasets”. PhD thesis. Massachusetts Institute of Technology, 2022.

[166] Sun, Jingzhang et al. “Pix2Pix generative adversarial network for low dose myocardial perfusion SPECT denoising”. In: *Quantitative Imaging in Medicine and Surgery* 12.7 (2022), p. 3539.

[167] Tang, Mengyun et al. “A joint tensor completion and prediction scheme for multi-dimensional spectrum map construction”. In: *IEEE Access* 4 (2016), pp. 8044–8052.

[168] Teganya, Yves and Romero, Daniel. “Deep completion autoencoders for radio map estimation”. In: *IEEE Transactions on Wireless Communications* 21.3 (2021), pp. 1710–1724.

[169] Tipler, Paul Allen and Mosca, Gene. *Física para la ciencia y la tecnología. II.* Vol. 2. Reverté, 2004.

[170] Tognola, Gabriella et al. “Use of Machine Learning for the Estimation of Down-and Up-Link Field Exposure in Multi-Source Indoor WiFi Scenarios”. In: *Bioelectromagnetics* 42.7 (2021), pp. 550–561.

[171] Ulyanov, Dmitry, Vedaldi, Andrea, and Lempitsky, Victor. “Deep image prior”. In: *Proceedings of the IEEE conference on computer vision and pattern recognition*. 2018, pp. 9446–9454.

[172] Van der Walt, S et al. *scikit-image: image processing in Python, PeerJ, 2, e453*. 2014.

[173] Vapnik, V. “Statistical Learning Theory Wiley-Interscience, New York”. In: (1998).

[174] Varga, Andras. “OMNeT++”. In: *Modeling and Tools for Network Simulation*. Ed. by Klaus Wehrle, Mesut Güneş, and James Gross. Berlin, Heidelberg: Springer Berlin Heidelberg, 2010, pp. 35–59. ISBN: 978-3-642-12331-3. DOI: `10.1007/978-3-642-12331-3_3`. URL: `https://doi.org/10.1007/978-3-642-12331-3_3`.

[175] Virtanen, Pauli et al. “SciPy 1.0: Fundamental Algorithms for Scientific Computing in Python”. In: *Nature Methods* 17 (2020), pp. 261–272. DOI: `10.1038/s41592-019-0686-2`.

[176] Vovk, Vladimir. “Kernel ridge regression”. In: *Empirical Inference: Festschrift in Honor of Vladimir N. Vapnik*. Springer, 2013, pp. 105–116.

[177] Wahl, René et al. “Dominant path prediction model for urban scenarios”. In: *14th IST Mobile and Wireless Communications Summit, Dresden (Germany)* (2005).

[178] Wang, Shanshan, Mazloum, Taghrid, and Wiart, Joe. “Prediction of RF-EMF Exposure by Outdoor Drive Test Measurements”. In: *Telecom*. Vol. 3. 3. MDPI. 2022, pp. 396–406.

[179] Wang, Shanshan and Wiart, Joe. “Sensor-aided EMF exposure assessments in an urban environment using artificial neural networks”. In: *International Journal of Environmental Research and Public Health* 17.9 (2020), p. 3052.

[180] Wang, Zhou et al. “Image quality assessment: from error visibility to structural similarity”. In: *IEEE Transactions on Image Processing* 13.4 (2004), pp. 600–612. DOI: `10.1109/TIP.2003.819861`.

[181] Wang, Zhuang et al. “Fast Construction of the Radio Map Based on the Improved Low-Rank Matrix Completion and Recovery Method for an Indoor Positioning System”. In: *Journal of Sensors* 2021 (2021), pp. 1–12.

[182] Welling, Max. “Kernel ridge regression”. In: *Max Welling’s class notes in machine learning* (2013), pp. 1–3.

[183] Wiame, Charles et al. *Joint data rate and EMF exposure analysis in Manhattan environments: stochastic geometry and ray tracing approaches.* 2023. arXiv: `2301.11097 [eess.SP]`.

[184] Wiart, Joe. “Propagation des ondes radioélectriques en milieu urbain dans un contexte microcellulaire. Analyse par la GTD et validation expérimentale”. PhD thesis. Paris 6, 1995.

[185] Wiedemann, Peter M et al. “When precaution creates misunderstandings: the unintended effects of precautionary information on perceived risks, the EMF case”. In: *Risk Analysis* 33.10 (2013), pp. 1788–1801.

[186] Williams, Christopher. “Computing with infinite networks”. In: *Advances in neural information processing systems* 9 (1996).

[187] Williams, Christopher K. I. “Computation with Infinite Neural Networks”. In: *Neural Computation* 10.5 (July 1998), pp. 1203–1216. ISSN: 0899-7667. DOI: `10.1162/089976698300017412`. eprint: `https://direct.mit.edu/neco/article-pdf/10/5/1203/813888/089976698300017412.pdf`. URL: `https://doi.org/10.1162/089976698300017412`.

[188] Xie, Junyuan, Xu, Linli, and Chen, Enhong. “Image Denoising and Inpainting with Deep Neural Networks”. In: *Advances in Neural Information Processing Systems.* Ed. by F. Pereira et al. Vol. 25. Curran Associates, Inc., 2012. URL: `https://proceedings.neurips.cc/paper/2012/file/6cdd60ea0045eb7a6ec44c54d29ed402-Paper.pdf`.

[189] Xu, Chunxue and Zhao, Bo. “Satellite image spoofing: Creating remote sensing dataset with generative adversarial networks (short paper)”. In: *10th International conference on geographic information science (GIScience 2018).* Schloss Dagstuhl-Leibniz-Zentrum fuer Informatik. 2018.

[190] Xue, Hongyang, Zhang, Shengming, and Cai, Deng. “Depth image inpainting: Improving low rank matrix completion with low gradient regularization”. In: *IEEE Transactions on Image Processing* 26.9 (2017), pp. 4311–4320.

[191] Yang, Greg and Hu, Edward J. *Feature Learning in Infinite-Width Neural Networks.* 2022. arXiv: `2011.14522 [cs.LG]`.

[192] Yeh, Raymond A. et al. "Semantic Image Inpainting with Perceptual and Contextual Losses". In: *CoRR* abs/1607.07539 (2016). arXiv: `1607.07539`. URL: `http://arxiv.org/abs/1607.07539`.

[193] Yilmaz, H Birkan et al. "Radio environment map as enabler for practical cognitive radio networks". In: *IEEE Communications Magazine* 51.12 (2013), pp. 162–169.

[194] Yoon, Jinsung, Jordon, James, and Schaar, Mihaela. "GAIN: Missing data imputation using generative adversarial nets". In: *International conference on machine learning.* PMLR. 2018, pp. 5689–5698.

[195] Yun, Zhengqing and Iskander, Magdy F. "Ray tracing for radio propagation modeling: Principles and applications". In: *IEEE access* 3 (2015), pp. 1089–1100.

[196] Zagoruyko, Sergey and Komodakis, Nikos. "Wide residual networks". In: *arXiv preprint arXiv:1605.07146* (2016).

[197] Zha, Song et al. "An novel non-parametric algorithm for spectrum map construction". In: *2018 International Symposium on Electromagnetic Compatibility (EMC EUROPE).* IEEE. 2018, pp. 941–944.

[198] Zhang, Chiyuan et al. "Understanding deep learning (still) requires rethinking generalization". In: *Communications of the ACM* 64.3 (2021), pp. 107–115.

[199] Zhang, Shuowen and Zhang, Rui. "Radio map-based 3D path planning for cellular-connected UAV". In: *IEEE Transactions on Wireless Communications* 20.3 (2020), pp. 1975–1989.

[200] Zhang, Tong and Oles, Frank J. "A probability analysis on the value of unlabeled data for classification problems". In: *17th International Conference on Machine Learning.* 2000. URL: `http://www-cs-students.stanford.edu/~tzhang/papers/icml00-unlabeled.pdf`.

[201] Zhu, Di et al. "Spatial interpolation using conditional generative adversarial neural networks". In: *International Journal of Geographical Information Science* 34.4 (2020), pp. 735–758.

[202] Zugno, Tommaso et al. "Toward standardization of millimeter-wave vehicle-to-vehicle networks: Open challenges and performance evaluation". In: *IEEE Communications Magazine* 58.9 (2020), pp. 79–85.